



**STUDY ON CONTROL OF
A ROBOTIC ORTHOSIS ACTUATED BY
PNEUMATIC ARTIFICIAL MUSCLES FOR
GAIT REHABILITATION**

a Dissertation Submitted to the
GRADUATE SCHOOL OF ENGINEERING AND SCIENCE OF
SHIBAURA INSTITUTE OF TECHNOLOGY

by

DAO QUY THINH

Student ID: nb16505

in Partial Fulfillment of the Requirements
for the Degree of

DOCTOR OF PHILOSOPHY

SEPTEMBER 2019

Acknowledgments

First of all, I would like to convey my special thanks to my supervisor, Professor Shin-ichiroh Yamamoto for his kindness, encouragements, enthusiastic guidance, helpful advice and technical support throughout my research. His constructive comments in every discussion are the key to my success today.

I would also like to thank all students in Neuro-Rehabilitation Engineering laboratory, Omiya campus, Shibaura Institute of Technology and special thanks to my all Vietnamese friends and colleagues for their supports.

Finally, I would also like to express my gratefulness to my family who always beside me all the time of my overseas research.

Saitama, September, 2019

Dao Quy Thinh

Abstract

There are millions of people worldwide with movement disability caused by neurological pathologies such as spinal cord injury (SCI), stroke, or traumatic brain injury. Rehabilitation devices such as lower-limb rehabilitation system can help the patients improve their recovery and assist therapists by supporting them to perform repetitive movements on the rehabilitation process. These devices carry some of the patient's weight to reduce the forces that the legs have to bear, making it similar to walking in a reduced gravitational field. Even though several systems have been ready on the market, the demand for improvement of those systems still poses difficulties in both hardware and control design perspective.

Recently, a high compliant gait training system named AIRGAIT has been developed in Neuro-Rehabilitation Engineering laboratory, Shibaura Institute of Technology. The AIRGAIT system consists of a treadmill, a body weight support system, and a lower-limb exoskeleton robot. The robotic orthosis is powered by pneumatic artificial muscles (PAMs). The actuator arrangement of the robot bases on the human musculoskeletal configuration with an additional pair of bi-articular muscles connecting between the hip and knee joints. The existence of a pair of bi-articular muscles can positively contribute to the compliant property of the multi-articular extremities. Furthermore, this additional pair of muscles also provides more power for position and force control of the endpoint of the extremities, which may result in smooth, fine and precise movements. In this research, the control system of the lower-limb robotic orthosis is continued to improve. Aiming to bring the AIRGAIT system towards commercialization, numerous control strategies are implemented to the system. As a result, the trajectory tracking performance is enhanced. Besides,

an assist-as-needed (AAN) training strategy has also been integrated into the system.

First, throughout the literature reviews on existing reports of the modeling and control of single pneumatic muscle or PAMs in antagonistic configuration, both linear and nonlinear mathematical model types are carefully reviewed together with the equivalent control algorithms in *Chapter 2*. Even though many considerable studies have been reported, it could be said that the field is still wide open in both modeling and control algorithm of PAMs. This chapter also introduces a feedforward-feedback control strategy and a discrete-time fractional order integral sliding mode control (DFISMC) for trajectory tracking purpose of an antagonistic actuator. Both control algorithms use a linear discrete second order plus dead time (SOPDT) model to describe the behavior of the actuator. The identification procedure of the proposed model is simplified. Experiment results show that both proposed controllers achieve better performances than the existing control approaches of the AIRGAIT system in the literature.

Second, the trajectory tracking control of the AIRGAIT robotic orthosis is proposed in *Chapter 3*. In this chapter, the behavior of the robotic orthosis which considers the contribution of the additional bi-articular muscles is built. Based on the built-in model, the modified computed torque control strategy is investigated for the trajectory tracking purpose. Particularly, the fractional order calculus $PI^\alpha D^\beta$ of the integration and differentiation term is used instead of the conventional integer ones. The fractional order controller offers more degree of freedom which can be utilized to further improve the tracking performance. In comparison with the conventional computed torque controller, the proposed control algorithm provides a better performance not only in the steady state but also during the transient process. This result is also much better than any existing control approaches of the AIRGAIT system.

The assist-as-needed training strategy is one of the most important requirements of any rehabilitation system because the disability level of patients not only varies from subject to subject but also changes during the training process with each subject. Since the control system

must be able to measure or estimate the disability level of the patient and change the robot impedance accordingly to encourage patient effort. *Chapter 4* of this thesis presents the development of impedance controller for AIRGAIT robotic orthosis. Also in this chapter, the patient's effort is estimated by the load cell by introducing the new defined human active torque. As a result, the support of the robotic varies with the patient's effort following that the AAN training strategy is achieved.

Finally, *Chapter 5* presents the troubleshooting of the AIRGAIT system. In rehabilitation devices, the safety of patients who interact directly with the robot is the highest priority. All the common issues might lead to hazards of the patient during training such as sensors malfunction, broken actuators, or the interrupt of any power sources, etc. must be carefully investigated. Following that, the control system classifies these risks and give suitable safety solutions. This troubleshooting helps the AIRGAIT system go one step ahead on the way to become a commercial product.

Contents

| | |
|--|-------------|
| Abstract | ii |
| Acknowledgments | ii |
| List of Figures | xi |
| List of Tables | xiii |
| List of Abbreviations | xiii |
| 1 Introduction and Objective | 1 |
| 1.1 Literature Review | 1 |
| 1.2 The AIRGAIT Lower-limb Gait Training System | 7 |
| 1.3 Challenges and Objectives | 10 |
| 1.4 Scopes and Limitations | 12 |
| 1.5 Significance of This Research | 12 |
| 1.6 Structure of the Thesis | 13 |
| 2 Modeling and control of Pneumatic Artificial Muscles | 15 |
| 2.1 Introduction | 15 |
| 2.2 Contributions | 16 |
| 2.3 Literature Review About Modeling and Control of PAMs | 16 |
| 2.3.1 Three-element Nonlinear Model | 16 |
| 2.3.2 The Hysteresis Model | 18 |
| 2.3.3 The Nonlinear Grey-Box Experimental Model | 20 |
| 2.3.4 The Linearized Model of Single PAM | 22 |
| 2.4 Feedforward-Feedback Control of an Antagonistic Actuator | 23 |
| 2.4.1 The Discrete-time Second Order Plus Dead Time (SOPDT) Model of an Antagonistic Actuator | 23 |

| | | |
|----------|---|-----------|
| 2.4.2 | Control Design | 28 |
| 2.4.2.1 | The Feedforward Controller | 29 |
| 2.4.2.2 | The Feedback Controller | 29 |
| 2.4.3 | Experimental Evaluation | 30 |
| 2.4.3.1 | Experimental Setup | 30 |
| 2.4.3.2 | Experimental results | 30 |
| 2.5 | Fractional Order Integral Sliding Mode Control Strategy | 34 |
| 2.5.0.1 | Fractional Order Calculus | 34 |
| 2.5.1 | Fractional Order Integral Approximation | 35 |
| 2.5.2 | Control Design | 37 |
| 2.5.3 | Experimental Evaluation | 41 |
| 2.5.3.1 | Experimental Procedure | 41 |
| 2.5.3.2 | Experimental Results | 42 |
| 2.6 | Conclusions | 45 |
| 3 | Trajectory Tracking Control of the AIRGAIT Orthosis | 50 |
| 3.1 | Introduction | 50 |
| 3.2 | Contributions | 51 |
| 3.3 | Mechanism Evaluation of the Robotic Orthosis | 51 |
| 3.4 | Modeling of the 2-DOF Robot Manipulated by Bi-articular Muscles | 53 |
| 3.5 | Trajectory Tracking Control Design | 55 |
| 3.5.1 | Computed Torque Control Strategy | 55 |
| 3.5.2 | Modified Computed Torque Control Strategy | 57 |
| 3.5.3 | Stability Analysis | 59 |
| 3.5.3.1 | Definitions of Stability | 59 |
| 3.5.3.2 | Lyapunov Functions | 60 |
| 3.5.3.3 | Lyapunov's Direct Method | 61 |
| 3.5.3.4 | Stability Analysis of the Closed Loop System | 61 |
| 3.6 | Experimental Evaluation | 62 |
| 3.6.1 | Experimental Setup | 62 |
| 3.6.2 | Experimental Protocol | 63 |
| 3.6.3 | Experimental Results | 64 |
| 3.7 | Conclusions | 66 |

| | | |
|----------|---|------------|
| 4 | Impedance Control of the AIRGAIT Orthosis | 68 |
| 4.1 | Introduction | 68 |
| 4.2 | Contributions | 69 |
| 4.3 | Human Robot Interaction Force Based Impedance Controller . . . | 70 |
| 4.3.1 | Control Design | 70 |
| 4.3.2 | Experimental Procedure | 73 |
| 4.3.3 | Experimental Results | 75 |
| 4.3.3.1 | Trajectory Tracking Control | 75 |
| 4.3.3.2 | Joint Compliance Control | 77 |
| 4.4 | Muscles Activation Level Based Impedance Controller | 79 |
| 4.4.1 | The Equivalent Muscles in Subject Body of the AIRGAIT Robotic Orthosis | 79 |
| 4.4.2 | The Muscle Activation Level based EMG Signal | 81 |
| 4.4.3 | The EMG-Based Fuzzy Controller | 84 |
| 4.4.4 | Simulation Results | 85 |
| 4.5 | Conclusions | 86 |
| 5 | Troubleshooting of the AIRGAIT System | 87 |
| 5.1 | Introduction | 87 |
| 5.2 | Contribution | 88 |
| 5.3 | Failure Classification | 88 |
| 5.4 | Safety Enhancement Procedure | 90 |
| 5.4.1 | General Definition | 90 |
| 5.4.2 | Safety Enhancement Procedure | 91 |
| 5.5 | Experimental Evaluation | 93 |
| 5.6 | Conclusions | 94 |
| 6 | Conclusions and Recommendation | 98 |
| 6.1 | Conclusions | 98 |
| 6.2 | Recommendation and Future Works | 100 |
| | References | 109 |
| | Research Achievements | 110 |

List of Figures

| | | |
|-----|---|----|
| 1.1 | (a) The hip orthosis; (b) The ankle orthosis RGT; (c) The ankle orthosis AFO. | 3 |
| 1.2 | (a) The wearing lower exoskeleton; (b) The underwater gait-training orthosis; (c) The Knee-Ankle-Foot Orthosis (KAFO). | 5 |
| 1.3 | The 6 DOF robotic orthosis. (a) Robotic orthosis, its major components, and all the DOFs labeled. (A) Parallelogram mechanism for vertical translation. (B) Height-adjustable frame. (C) Hip sagittal plane revolute joint. (D) Walker. (E) Ankle sagittal plane revolute joint. (F) Treadmill. (G) Foot lifter. (H) Knee sagittal plane revolute joint. (I) Hip abduction/adduction revolute joint. (J) Sliders for lateral translation. (b) Experimental setup of the robotic orthosis with a subject walking on a treadmill. | 6 |
| 1.4 | The AIRGAIT System: (a) The schematic diagram. (b) The real image of the system | 9 |
| 1.5 | (a) The lower-limb robotic exoskeleton; (b) A typical antagonistic configuration. | 10 |
| 2.1 | The AIRGAIT System: (a) The schematic diagram of PAM. (b) The three-element model of PAM. | 17 |
| 2.2 | The PAM Maxwell-slip model. Description of the predicted pressure output: four Maxwell-slip elements are intuitively selected, the output prediction of the extracted hysteresis pressure P_{hys} is the sum of the individually contributing outputs $P_{hys1, \dots, 4}$ of these elements. | 18 |
| 2.3 | The scheme of the cascade position control of the single PAM based Maxwell-slip model. | 20 |
| 2.4 | Experiment setup of the Grey-Box model of single PAM. | 21 |

| | | |
|------|---|----|
| 2.5 | Robust Adaptive Internal Model Control Structure. | 22 |
| 2.6 | (a)The typical antagonistic configuration of two PAMs and (b) the experiment platform of an antagonistic actuator powered by PAMs. | 24 |
| 2.7 | Identification results of the antagonistic actuator: (a) the step input of 0.4 MPa, (b) the 0.5 Hz sinusoidal signal, and (c) the time-varying amplitude and frequency control input. Upper sub-figures show measured (blue line) and estimated (dash red line) values of the actuator angle. Lower sub-figures show the estimation errors of the mathematical model. | 27 |
| 2.8 | The typical block diagram of each joints. P_0 is the nominal pressure supplied to the PAMs, P_{AP} is the different pressure of two PAMs. | 28 |
| 2.9 | Experiment results without a load for tracking a sinusoidal trajectory: (a) 0.2 Hz, (b) 0.5 Hz, (c) 0.8 Hz and (d) 1.0 Hz of signal frequency. | 31 |
| 2.10 | Experiment results of the proposed controller and conventional DSMC controller when tracking the human-gait pattern signal: (a) 4 seconds and (b) 2.5 seconds of gait cycle time. The experiment was carried out without a load. | 32 |
| 2.11 | Experiment results with 2.5kg of load for tracking a sinusoidal trajectory: (a) 0.2 Hz, (b) 0.5 Hz, (c) 0.8 Hz and (d) 1.0 Hz of signal frequency. | 33 |
| 2.12 | Experiment results for the proposed controller and conventional DSMC controller when tracking the human-gait pattern signal with a load $m = 2.5$ kg: (a) 4 seconds and (b) 2.5 seconds of gait cycle time | 34 |
| 2.13 | Block diagram of the discrete-time fractional integral sliding mode control. | 38 |
| 2.14 | Experiment results without a load for tracking a sinusoidal trajectory: (a) 0.2 Hz, (b) 0.5 Hz, (c) 0.8 Hz, and (d) 1.0 Hz of signal frequency. | 42 |
| 2.15 | Experiment results of the proposed controller and conventional DSMC controller when tracking the human-gait pattern signal: (a) 4 seconds and (b) 2.5 seconds of gait cycle time. The experiment was carried out without a load. | 43 |

| | | |
|------|--|----|
| 2.16 | MTE and RMSTE of the proposed controller and conventional DSMC controller with 0.2 Hz, 0.5 Hz, 0.8 Hz, and 1.0 Hz of the desired signal frequency in case of no load. | 43 |
| 2.17 | Experiment results with 2.5 kg of load for tracking a sinusoidal trajectory: (a) 0.2 Hz, (b) 0.5 Hz, (c) 0.8 Hz, and (d) 1.0 Hz of the desired signal frequency. | 46 |
| 2.18 | Experiment results for the proposed controller and conventional DSMC controller when tracking the human-gait pattern signal with a load $m = 2.5$ kg: (a) 4 seconds and (b) 2.5 seconds of gait cycle time. | 47 |
| 2.19 | MTE and RMSTE of the proposed controller and conventional DSMC controller with 0.2 Hz, 0.5 Hz, 0.8 Hz, and 1.0 Hz of the desired signal frequency and load $m = 2.5$ kg. | 47 |
| 3.1 | The average value of angle trajectory of orthosis joint compared to subject normal walking in one gait cycle. | 52 |
| 3.2 | The peak value of orthosis angle compared to normal walking. . . | 52 |
| 3.3 | (a) Typical 2DOF robotic (b) Robotic Orthosis with two mono-articular and one bi-articular muscles. The 1, 2, 3 subscripts represent hip, knee and bi-articular muscle. A and P subscripts denote the anterior and posterior PAMs. | 53 |
| 3.4 | Block diagram of the computed torque control strategy. | 56 |
| 3.5 | Block diagram of the modified computed torque control strategy. . | 57 |
| 3.6 | The hip and knee joint angle trajectories of the proposed controller and normal computed torque one during the startup process: (a) Hip joint (b) Knee joint. | 64 |
| 3.7 | The trajectory tracking performance of the proposed controller, the hip and knee trajectories are averaged over all subjects for two gait cycles. | 65 |
| 4.1 | The typical antagonistic configuration. | 70 |
| 4.2 | The compliance control method of the AIRGAIT robot orthosis: (a) The position of the load cell on robot orthosis and (b) the dependence of the robot compliance base on the human effort. . . | 72 |
| 4.3 | Compliance control architecture of the AIRGAIT robotic orthosis. | 74 |

| | | |
|------|---|----|
| 4.4 | Trajectory tracking control performance of AIRGAIT robotic orthosis in passive mode (blue line) and active mode (red line). The gait data is normalized and plotted as reference trajectories. . . . | 75 |
| 4.5 | Joint sagittal plane compliance of AIRGAIT robot orthosis: (a) Hip joint and (b) Knee joint. | 77 |
| 4.6 | The human-robot interactive torque (HRIT) of AIRGAIT robotic orthosis during active and passive modes: (a) Hip joint and (b) Knee joint. | 78 |
| 4.7 | The muscle system: (a) The actuator arrangement of the AIRGAIT orthosis. (b) The human musculoskeletal system | 79 |
| 4.8 | The muscle system: (a) The actuator arrangement of the AIRGAIT orthosis. (b) The human musculoskeletal system | 80 |
| 4.9 | The example of subject 1's EMG signal: (a) standardized of Vastus Lateralis EMG signal. Means and standard deviations of the EMG signals after standardizing: (b) The Vastus Lateralis, (c) Rectus Femoris, (d) Biceps Femoris Short Head and (e) Biceps Femoris Long Head muscles. | 82 |
| 4.10 | The RMS of EMG signal over all subjects: (a) The Vastus Lateralis, (b) Rectus Femoris, (c) Biceps Femoris Short Head and (d) Biceps Femoris Long Head muscles. | 83 |
| 4.11 | The system fuzzy variables designed in LabView. | 85 |
| 4.12 | The simulation result of EMG-based fuzzy controller: (a) The hip joint and (b) knee joint assistant level. | 86 |
| 5.1 | The failure classification. | 89 |
| 5.2 | The flowchart for determining the safety procedure. | 92 |
| 5.3 | The detection of broken PAMs: (a) Anterior PAM and (b) posterior PAM of bi-articular muscles. | 95 |
| 5.3 | The detection of broken PAMs: (c) anterior PAM and (d) posterior PAM of knee mono-articular muscles. | 96 |

List of Tables

| | | |
|-----|--|----|
| 1.1 | The Literature Review about Lower-limb Rehabilitation Systems. | 8 |
| 2.1 | Initial parameters of PAMs. | 25 |
| 2.2 | Identified Parameters of the Antagonistic Actuator. | 28 |
| 2.3 | The parameters of the controllers | 31 |
| 2.4 | Experiment results of the FFFB controller. | 32 |
| 2.5 | Parameters of the DFISMC and conventional DSMC controller. | 42 |
| 2.6 | MTE and RMSTE of the DFISMC control method, conventional DSMC control method, and FFFB controller in case of no load. | 44 |
| 2.7 | MTE and RMSTE of the proposed control method, conventional DSMC control method, and FFFB controller with load $m = 2.5\text{kg}$ | 45 |
| 2.8 | The Comparison Results About Modeling and Control of PAMs. | 49 |
| 3.1 | The information of five subjects participating the mechanism evaluation experiment. | 51 |
| 3.2 | Parameters of the AIRGAIT Robotic Orthosis. | 54 |
| 3.3 | The Parameters of the Proposed Controller. | 58 |
| 3.4 | Absolute Values of Maximum Tracking Error, Root Mean Square Tracking Error Averaged over All subjects in Two Gait Cycles. | 66 |
| 3.5 | The Comparison Results of the AIRGAIT System to the Existing Systems. | 67 |
| 4.1 | The spring parameters of PAMs. | 71 |
| 4.2 | The information of eight subjects. | 74 |
| 4.3 | The parameters of the proposed controller. | 75 |

| | | |
|-----|--|----|
| 4.4 | Maximum tracking error (MTE), RMSTE and maximum compliance (Comp^{max}) of hip and knee joint in the experiment. Standard deviation (\pm) are presented for subject variability. * means the significantly improve. | 76 |
| 4.5 | The information of three subjects. | 81 |
| 4.6 | The RMS range of each muscle's EMG voltage. | 84 |
| 5.1 | The Equivalent Range of the Sensor System. | 90 |
| 5.2 | The minimum pressure inside each PAMs. | 93 |
| 5.3 | The detection time of the system when the broken PAMs. | 94 |

List of Abbreviations

Acronyms

| Symbol | Description |
|--------|--|
| AAN | Assist-as-needed |
| AFO | Ankle Foot Orthosis |
| BASMC | Boundary layer-Augmented Sliding Mode Control |
| BFLH | Biceps femoris long head muscle |
| BFSH | Biceps femoris short head muscle |
| BWS | Body Weight Support |
| COM | Center of mass |
| CRVC | Chattering-free robust variable structure control |
| DC | Direct Current |
| DFISMC | Discrete-time Fractional Integral Sliding Mode Control |
| DLPF | Discrete-time Low-pass Filter |
| DOF | Degree of Freedom |
| DSMC | Discrete-time Sliding Mode Control |
| EBFC | EMG-Based Fuzzy Controller |
| ECV | Electric Control Valve |
| EMG | Electromyography |

| | |
|-------|----------------------------------|
| FOD | Fractional order differential |
| FOI | Fractional order Integral |
| GC | Gait Cycle |
| GM | Gluteus Maximus muscle |
| GMS | Generalized Maxwell-Slip |
| HRIT | Human Robot Interaction Torque |
| IL | Iliosoas muscle |
| IMC | Internal Model Control |
| KAFO | Knee Ankle Foot Orthosis |
| MTE | Maximum Tracking Error |
| PAM | Pneumatic Artificial Muscle |
| PI | Proportional Integral |
| PID | Proportional Integral Derivative |
| RF | Rectus femoris muscle |
| RGT | Robotic Gait Trainer |
| RLS | Recursive Least Square |
| RMSTE | Root Mean Square Tracking Error |
| SCI | Spinal cord injury |
| SD | Standard Deviation |
| SEA | Series elastic actuator |
| SISO | Single input single output |
| SMC | Sliding Mode Control |
| SMC | Sling Mode Control |

| | |
|-------|----------------------------|
| SOM | Spring Over Muscle |
| SOPDT | Second Order Plus Deadtime |
| VL | Vastus Lateralis muscle |
| WHO | World Health Organization |

Greek Symbols

| Symbol | Description |
|------------------|---|
| α | Fractional order of integral |
| β | Fractional order of differential |
| ΔP | Different pressure of two PAMs in antagonistic actuator |
| Ω, ω | Weighting factors of fractional order integral |
| τ | Robot muscle torque matrix |
| θ | Measured trajectory |
| ε | Contraction of PAM |

Superscripts

| Symbol | Description |
|---------------|-------------------------|
| θ^* | Desired trajectory |
| z^{-1} | Backward shift operator |

Subscripts

| Symbol | Description |
|----------------------|--|
| γ_i | Compliance of antagonistic actuator |
| \hat{T}_h | Estimation of human active torque |
| a_1, a_2, b_1, b_2 | Known parameters of antagonistic actuator model |
| B_{0d}, B_{1d} | The parameters of PAM's damping element during deflation state |

| | |
|----------------------------------|--|
| B_{0i}, B_{1i} | The parameters of PAM's damping element during inflation state |
| $C_{11}, C_{12}, C_{21}, C_{22}$ | Elements of system coriolis matrix |
| $D_{11}, D_{12}, D_{21}, D_{22}$ | Elements of system mass matrix |
| e_k | Tracking error at time instance k |
| F_0, F_1 | The parameters of PAM's contractile force element |
| f_c | Cut-off frequency of the low-pass filter |
| G_P | Process transfer function |
| G_1, G_2 | Elements of system gravity matrix |
| G_{FB} | Feedback term transfer function |
| G_{FF} | Feedforward term transfer function |
| G_{total} | Closed-loop transfer function |
| I_1 | Hip link inertia |
| I_2 | Knee link inertia |
| K_0, K_1 | The parameters of PAM's spring element |
| K_d | Differential gain |
| K_i | Integral gain |
| K_p | Proportional gain |
| K_{FF} | Feedforward controller gain |
| K_{imp} | Impedance controller gain |
| l_1 | Length of the hip link |
| l_2 | Length of the knee link |
| m_1 | Hip link mass |

| | |
|-----------|--|
| m_2 | Knee link mass |
| p_k | Disturbance at time instance k |
| P_{0A} | Nominal pressure of anterior PAM of antagonistic actuator |
| P_{0P} | Nominal pressure of posterior PAM of antagonistic actuator |
| T_s | Sampling time |
| T_h | Human active torque |
| T_{int} | Human robot interaction torque |
| u_k | Control signal at time instance k |
| y_k | Measured output at time instance k |

Other Symbols

| Symbol | Description |
|-------------------------------|---|
| ${}^\alpha \hat{\zeta}_{e,k}$ | Fractional order integral of tracking error at time instance k |
| ${}^\beta D_{t_0} e(t)$ | Fractional order differential of tracking error $e(t)$ |
| $B(z^{-1}), A(z^{-1})$ | Numerator and denominator polynomial of antagonistic actuator's transfer function, respectively |
| $Comp_i^{Max}$ | Maximum Compliance of joint i |
| $O(T_s^2)$ | Same order with T_s^2 |
| T_{int}^{Active} | The human-robot interaction torque during active walking mode of the subject |
| $T_{int}^{Passive}$ | The human-robot interaction torque during passive walking mode of the subject |
| d | Delay time in number of sampling time |
| e | Tracking error |
| T | Robot joint torque matrix |

Chapter 1

Introduction and Objective

This chapter starts with a literature review of gait training systems which are based on the body weight support and treadmill together with how it effects during rehabilitation. Then, a detail description of the AIRGAIT gait training system such as hardware design, actuators, and the existing controller, etc. is provided together with its challenges and objectives. Finally, this chapter is ended by presenting the outline of this dissertation organization.

1.1 Literature Review

Based on WHO statistic, millions of people in the world today involve disability. These people generally face difficulties with daily living activities. The rehabilitation process may help the patient with disability not only to slow the rate of loss function but also improve the restoration of function. However, traditional rehabilitation therapies, especially for gait training, are very labor and difficult to perform for a long duration of time. Patients' paralyzed legs are guided by therapists during physical training of traditional rehabilitation.

According to a report on the treadmill training therapy based on 'rules of spinal locomotion' by Wernig *et al.* [1, 2], the neurological patients, i.e. SCI can be improved locomotive capabilities far beyond the traditional rehabilitation. In this study, the patients participated in the training program which supported by a motor-driven treadmill initially with a BWS and assisted limb movements by therapists for their daily upright walking training. After the rehabilitation

session, more than three-quarter of 33 individuals with incomplete SCI can walk independently, and only one patient did not improve.

Recently, robot-assisted therapy devices have been increasingly used in rehabilitation. These robots can support patients to perform repetitive and systematic training sessions as long as possible. Since these types of robot interact closely with humans, safety is always the top priority consideration in the design. Besides, the compliance of the robot must also be controlled to give the subject the best comfort during training. Three important requirements for this type of robots are as follow:

- 1) A safe and comfortable mechanism,
- 2) High stiffness enough to guide the subject to the designate trajectories during training,
- 3) And can estimate the patient disability level and provide the assistance accordingly.

It is a general assumption that actuators play an important role in not only mechanism design but also control strategy of rehabilitation robot. Recently, a natural and low-cost actuator PAM is widely implemented in the development of rehabilitation systems. In comparison with conventional actuators such as electrical motor, series elastic actuator (SEA) and brushless DC motor, PAM has many advantages including natural compliant, lightweight, and high ratio from weight to power. Despite inherent drawbacks such as a very high nonlinear and uncertain characteristic, a slow response in force generation, the applications of PAM in rehabilitation robotic fields are exponential growth due to the demand on much high compliant of human-robotic system. The literature review of the recently PAMs based rehabilitation robot system is present in the following discussion. The first robotic orthosis actuated by PAM was developed by Claysson B. Vimieiro et al. in 2004 [3] for supporting the hip flexion movement of the patients. As shown in 1.1, this exoskeleton is designed with two main parts: the first one is a pelvic brace to provide the stability of the robot, and the second one is support for the thigh. Two parts are connected by the metallic beam and powered by PAM. The clinical results showed that the exoskeleton was able to provide not only more stabilization but also better condition for the patients during walking activity.

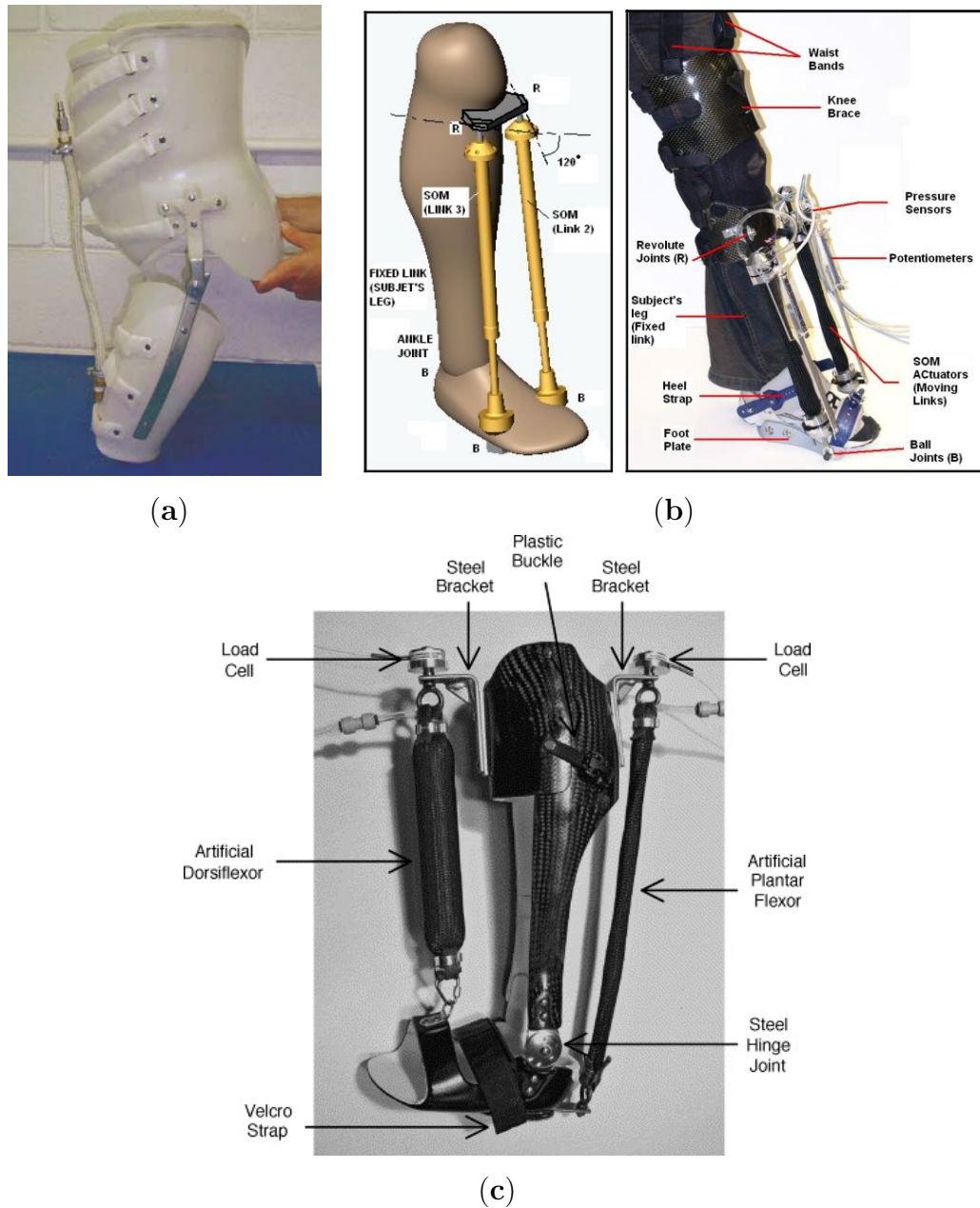


Figure 1.1: (a) The hip orthosis; (b) The ankle orthosis RGT; (c) The ankle orthosis AFO.

Another example of PAM-based robotic orthosis is Robotic Gait Trainer (RGT) for stroke rehabilitation of ankle joint which was developed by Kartik et al. from Human/Machine Integrated Laboratory, Arizona State University, the USA in 2006 [4]. This ankle orthosis is structured based on a tripod mechanism with one fixed link and is actuated by compliant Spring Over Muscle (SOM)

actuators. This device is able to support the ankle movements in the dorsiflexion and plantar-flexion, as well as, the inversion and eversion directions. About the control system, this robot can archive the angular position by using two types of sensors are potentiometers and pressure sensors.

Similar with two above mentioned assistive robots, the prototype of an Ankle-Foot Orthosis (AFO) [5] was designed for supporting only one part of patient lower-limb (i.e. ankle joint). As shown in Fig 1.1c, the robot is combined with a hinge joint and a plastic buckle made from carbon fiber shell. Two PAMs were used to actuate the subject's ankle in dorsiflexor and plantar flexor directions. A proportional myoelectric control approach through the PC and real-time control board (dSPACE, Inc., Northville, MI) was employed to regulate the air pressure in both PAMs. The experiment was conducted with a healthy subject to test the performance and comfort during gait. As a result, the orthosis can be useful for rehabilitation training.

To develop new "human-friendly" exoskeleton robotic orthosis which can cover all parts of patients' lower-limb, Nelson Costa et al. [6] combined PAM a highly compliant actuator with an intelligent embedded control system. By using PAMs were arranged in antagonistic configuration and employed a three-level PID joint torque control scheme, this robot can produce powerful inherent safe operation for paraplegic patients. Although this system only evaluated without the participation of a subject, its prototype provided significant design for the development of rehabilitation robots and rehabilitative protocol for paraplegic patients. Figure 1.2a illustrates the real image of the developed exoskeleton. Figure 1.2b shows the development of a PAM-based underwater gait-training orthosis was introduced by Miyoshi et al. in 2008 [7]. This robot covers hip, knee, and ankle of the patients and allows to train under water. The control system was designed based on the angular motions of the hip and knee joints of a healthy subject as he walked in the water. The system was evaluated with the participation of a healthy subject. A partial BWS and treadmill training is also implemented in the system.

In 2009, the AFO robot in [5] was upgraded to the Knee-Ankle-Foot orthosis (KAFO) [8] which covered all parts of the patient's lower-limb as shown in Figure 1.2c. In comparison to AFO, this system is implemented a physiologically-inspired controller which used the information of the patient's muscles providing by EMG sensors. This robot also performed more positive mechanical works than the

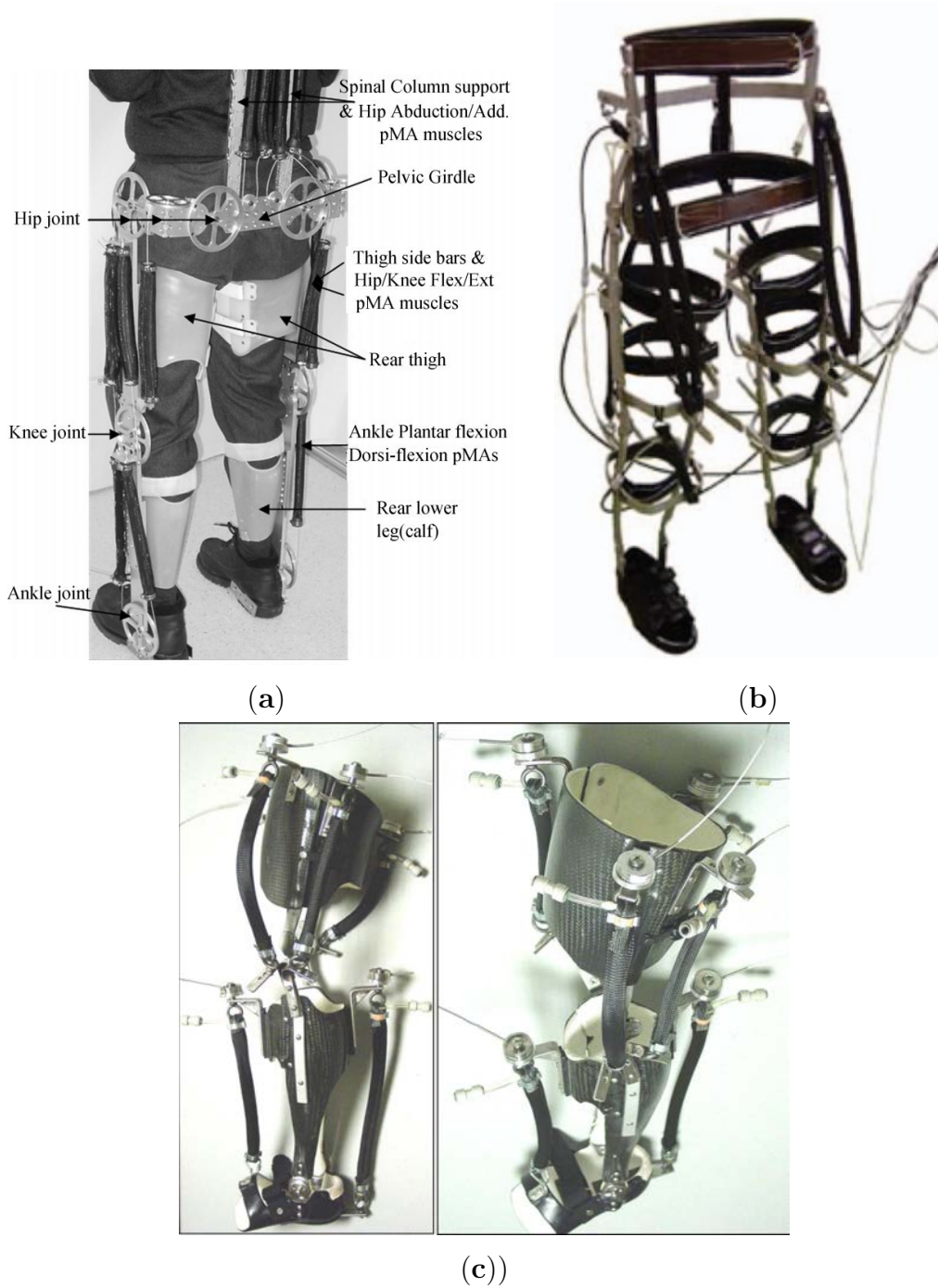


Figure 1.2: (a) The wearing lower exoskeleton; (b) The underwater gait-training orthosis; (c) The Knee-Ankle-Foot Orthosis (KAFO).

previous version. The robot was successfully applied to assist individuals with incomplete spinal cord injury during locomotor training. It is believed that the KAFO has promising clinical and basic science applications.

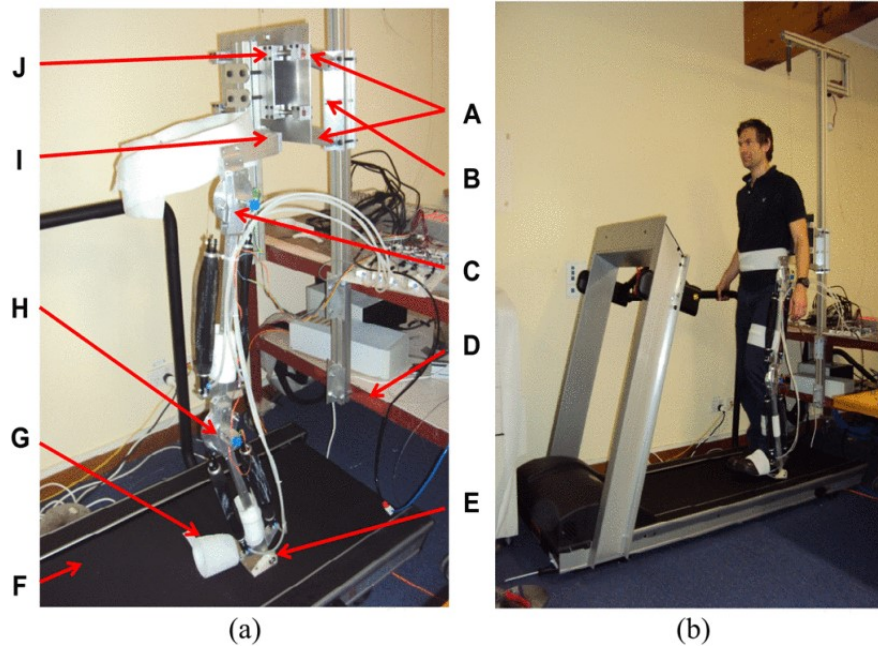


Figure 1.3: The 6 DOF robotic orthosis. (a) Robotic orthosis, its major components, and all the DOFs labeled. (A) Parallelogram mechanism for vertical translation. (B) Height-adjustable frame. (C) Hip sagittal plane revolute joint. (D) Walker. (E) Ankle sagittal plane revolute joint. (F) Treadmill. (G) Foot lifter. (H) Knee sagittal plane revolute joint. (I) Hip abduction/adduction revolute joint. (J) Sliders for lateral translation. (b) Experimental setup of the robotic orthosis with a subject walking on a treadmill.

Most of the above mentioned systems are in the early stages of the development with trajectory tracking function only. For rehabilitation, the "assist-as-needed" is a better training approach. The robot orthosis not only have a high stiffness enough to guide the patient's limb to the designated trajectory but also can estimate the disability level of the patient and provide the needed assistance. Recently, a six degree of freedom robotic orthosis was invented for gait rehabilitation by Hussain et al. [9] in 2011. Figure 1.3 demonstrates the main part of this robot. The exoskeleton is powered by two pairs of PAMs in an antagonistic configuration. Consequently, many control approaches were implemented to the system, i.e. Boundary layer-Augmented Sliding Mode Control (BASMC), chattering-free robust variable structure control law (CRVC) for trajectory tracking purpose. In some consequent reports, this robot is also able to patients disability level and provide the needed assistance by employed the

impedance control method. As a result, the AAN training strategy is integrated into the system.

Even though many others prototype systems of PAMs based rehabilitation robot have been developed in research centers [8, 10, 11, 12, 13, 14, 15, 16], most of them are designed with single pairs of mono-articular muscles for each joint of the hip, knee, and ankle. The positive contribution of the bi-articular muscle to the robot motion already reported by Kumamoto *et al.* [17] in 1994. The existence of the additional muscles can positively contribute to the compliant property of the multi-articular extremities. These muscles also provide the robot the redundancy in both its kinematic and dynamic. The additional pair of bi-articular muscles which connect between hip and knee joints play a similar role as Bicep Femoris and Rectus Femoris muscles in the actual human musculoskeletal system. This may help us better understand the anatomy of our body. This research is implemented in AIRGAIT rehabilitation robotic orthosis which design with additional bi-articular muscles [18]. Table 1.1 provides a summary about the configurations and control performances of the recently PAM-based rehabilitation prototypes including our AIRGAIT system before this research. The information of the commercial gait training system LOKOMAT is also provided for further analysis.

1.2 The AIRGAIT Lower-limb Gait Training System

Figure 1.4a demonstrates the schematic diagram of the AIRGAIT rehabilitation system. The design of this system already was thoroughly introduced and evaluated in some previous researches output [19, 20]. The main following parts of the AIRGAIT orthosis are numbered and shown in Fig. 1.4a.

1) The height of the lower limb orthosis (A) can be changed to fit with the subject height by a slider (D).

2) The springs (E and G) and parallel linkage (F) allows the vertical movement of the orthosis.

3) The BWS system included counterweight (I) and body hardness (C) is employed for the safety and weight compensation purpose. The level of support

Table 1.1: The Literature Review about Lower-limb Rehabilitation Systems.

| Prototype | Covered joints | Configuration | Control system | Performance | References |
|--------------|----------------|------------------|-----------------------|--|---------------------|
| Hip Orthosis | Hip | single PAM | Position control | - | [3] |
| RGT | Ankle | 2 single PAMs | Position control | - | [10] |
| AFO | Ankle | Mono-articular | Proportional control | - | [5, 10] |
| PLLO | All leg | Mono-articular | PID | - | [6] |
| WGTO | All leg | Mono-articular | - | - | [16] |
| KAFO | Knee & Ankle | Mono-articular | Torque control | - | [5] |
| KNEXO | Knee & Ankle | Mono-articular | PID & Feedforward | 0.7m/s | [11] |
| AIRGAIT | Hip & Knee | Bi-articular | PID & computed torque | - | [19, 20, 21] |
| 6-DOF robot | All leg | Mono-articular | Modified SMC | $\theta = 50^\circ, e = 9.31^\circ,$ 0.6m/s $\theta \geq 60^\circ, e = 15^\circ,$ 2.0km/h | [9, 22, 23, 24, 25] |
| LOKOMAT | All leg | Motorized system | - | - | [26] |

Abbreviations:

PID: Proportional Integral Derivative

SMC: Sliding mode control

1.2 The AIRGAIT Lower-limb Gait Training System

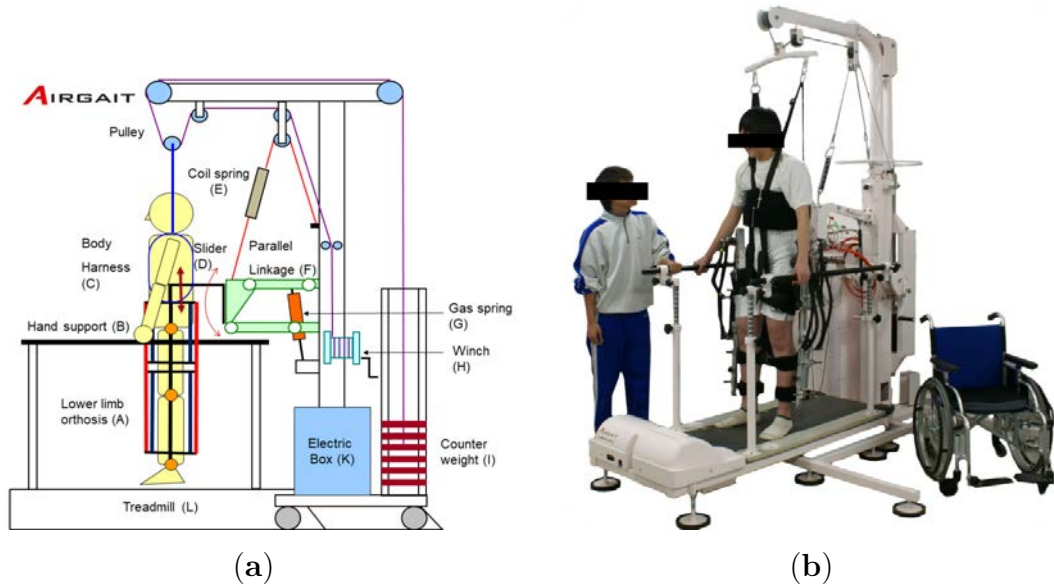


Figure 1.4: The AIRGAIT System: (a) The schematic diagram. (b) The real image of the system

can be varied by winch (H).

The leg orthosis is fixed in the sagittal plane which divides the body subject into the right and left halves. The thigh segment and shank segment of the orthosis can be adjusted to match the body of the subject by the slider and fixed by the screw during training. The maximum joint angles of the hip and knee flexion/extension movement are $+60^{\circ}/60^{\circ}$ and $+90^{\circ}/0^{\circ}$, respectively. The orthosis frame was made from aluminum alloy to satisfied the torque transmission requirement. The orthosis connected to the lower limb of the subject by three plastic braces: one at the thigh and two at the shank part. The braces have a soft fabric strap inside to prevent the subject from hurt during training. Two bar-shape load cells are attached between orthosis and the braces for two purposes: measuring the orthosis torque affected to the subject and the human force interact with the orthosis.

The structure of the lower-limb robotic exoskeleton is shown in Figure 1.5a. The robotic gait training system covers the thigh at the lower end of the hip joint and shank at the lower end of the knee joint. The ankle joint orthosis is not included and researched separately. It is actuated by PAMs in an antagonistic configuration as illustrated in Figure 1.5b. The PAM used in this research is a self-made McKibben artificial muscle with 1.0-inch diameter. Similar to human

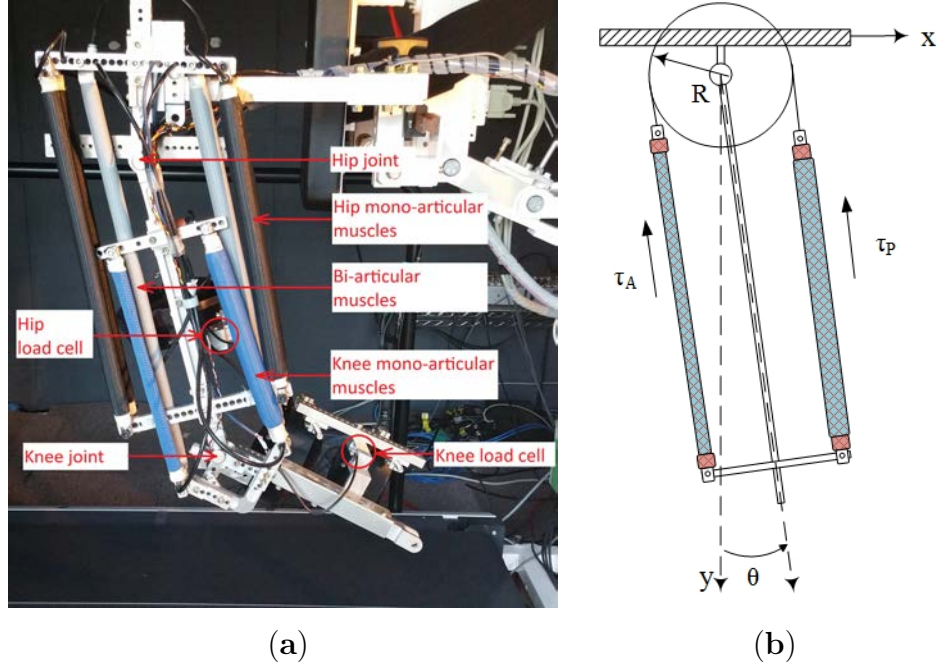


Figure 1.5: (a) The lower-limb robotic exoskeleton; (b) A typical antagonistic configuration.

muscle, this PAM can reach a maximum contraction of 30% from the complete deflation length. The detailed parameters of PAMs are provided in Table 1. Proportional electric control valves ITV2000/3000 of SMC company are used to regulate the pressure of PAMs. The angle of knee and hip joints are measured by contactless Hall-IC named CP-20H of Midori Precisions. To implement the control algorithm, a CompactRIO platform developed by National Instrument is employed. It consists of a real-time processor for communication and signal processing, a field programmable gate array (FPGA) to run high-speed control. Besides, the sensors and control valves can be connected directly to the CompactRIO via industrial plug-in analog and digital inputs/outputs. The control algorithm is implemented and compiled by Labview software first and downloaded to CompactRIO for real-time control after that.

1.3 Challenges and Objectives

This research thesis continues to improve on the control system of a rehabilitation robotic orthosis named AIRGAIT. In comparison with the existing robotic ortho-

sis actuated by two mono-articular actuators for hip and knee joints [8, 10, 11, 12, 14, 27], an additional pair of bi-articular muscles connecting between the hip and knee joint is introduced which results in a human musculoskeletal system. Several strategies have been used for trajectory tracking control of the developed system such as conventional PID controller [19], co-contraction model [20], or computed torque approach [21]. However, the system only shows good performance without the participation of the subject at low walking speed. Besides, the model of the robot has not considered since all controllers are designed independently in [19, 20] and the AAN training strategy has not been integrated yet [21].

This research focuses on improving the control system of the AIRGAIT robotic orthosis. Firstly, the actuator consist of two PAMs in the antagonistic configuration is linearized and modeled. Based on the model of the actuator, some advanced control techniques are employed for trajectory tracking purpose. Then the dynamic behavior of overall robot which considers the contribution of the bi-articular muscles must be built for improving the control performance. Finally, the AAN training strategy should be implemented by regulating the robot joint compliances. Due to the safety requirements of the rehabilitation device, the operation of the system under incident working condition also be considered for troubleshooting purpose.

This research thesis embarks on the following objectives:

- (1) To describe the dynamic behavior of pneumatic artificial actuator in the antagonistic configuration of the AIRGAIT robotic orthosis by a more simple mathematical model. The used model should not only be obtained by a not complicated procedure but also achieve high accuracy approximation.
- (2) To derive and model the dynamic behavior of the AIRGAIT exoskeleton orthosis considering the contribution of the additional bi-articular muscles.
- (3) To improve the trajectory tracking performance of the AIRGAIT orthosis by employed some advanced control techniques.
- (4) To integrate the AAN training strategy to the AIRGAIT exoskeleton robotic orthosis by control the robot joint compliances.
- (5) To reduce the collision injury for the patient during training by implementing the safety procedure to the AIRGAIT system.

1.4 Scopes and Limitations

This research thesis is carried out with some scopes and limitations as follows:

- (1) The model parameters are derived based on the self-made PAM in the antagonistic configuration of the AIRGAIT exoskeleton robotic orthosis.
- (2) All the measurements, control performances, and experimental results were executed based on the overall BWS gait training system named AIRGAIT.
- (3) All the experimental procedures related to human were approved by the Ethics Committee of Shibaura Institute of Technology and conducted with only the healthy subjects.

1.5 Significance of This Research

Patients suffering from walking difficulty have a better recovery if they intend the rehabilitation programs. However, traditional therapy, exercises, and targeted play activities to train effective movements necessitate intensive of many therapists. Besides, these therapy tasks are potentially painful for therapists. For instance, attempting overground balance training to a patient who has heavy-weight and disability is always difficult and unsafe. Physiotherapy general requires a technical therapist to execute and assess the rehabilitation outcomes. This also reduces the chance to participate in the training session of the patients and their family. Therefore, the goal is not only to reduce the therapist labor but also prevent him from the painful aspects of his works lead to longer and more effective training sessions for the patients. Another barrier to rehabilitation is the lack of financial therapy services and the lack of resources and health infrastructure [28]. This can reduce access to rehabilitation and its quality.

Rehabilitation assistive robots are promising research to take over the barriers of traditional rehabilitation. This type of robot should have an adjustable frame because the robot can be used for multi patients who have different bodies. It also needs to be programmable for executing a large range of rehabilitation procedures. The needed of adjustable and programmable in development is the most difficult of a rehabilitation robot in comparison with an industrial robot which always

the same for the specific tasks. Recently, the rehabilitation robot has been used widely in physical and rehabilitation medicine. This can solve the barrier of the lack of doctors and technical therapists. This also increases the duration of each training session. The doctors may be supported too much with his or her rehabilitation decision making by using the helpful data automatically collected during training sessions.

The development of a rehabilitation robot might give a chance to extend the therapy at home and increase the contribution of the patient family to his or her training process. With the programmable and remote controllable abilities, the rehabilitation robot can provide many home therapies with remote support from the medical center. Unfortunately, the cost of a rehabilitation robot is inversely proportional to its easy-to-use and flexibility. For this reason, the cost of this robot must first come down for applying at home and small health care centers.

This research continues to develop the high compliance lower-limb gait training system based on body weight support and a treadmill named AIRGAIT and focus on the control system of the robot exoskeleton. The main contents of this research will be summarized in the next section of the chapter.

1.6 Structure of the Thesis

The thesis title is “Study on control of a robotic orthosis actuated by pneumatic artificial muscles for gait rehabilitation”. The content of the research thesis which consists of six different chapters including introduction, modeling, trajectory tracking control, impedance control, troubleshooting, and conclusions.

Chapter 1: The first chapter provides an introduction and backgrounds related to the research including the literature review, challenges and objectives, scopes and limitations, and outline of the research.

Chapter 2: The second describes dynamic models of pneumatic muscle and its control strategies. In this chapter, a simple linearized model is introduced for modeling PAMs in the antagonistic configuration. Base on the built-in mathematical model of the actuator, a modified feedforward-feedback control strategy is employed to improve the tracking performance of the PAM-based system. All

procedures for deriving the model and tuning the controller parameters are also included in this chapter.

Chapter 3: The third chapter focus on trajectory tracking purpose of the AIRGAIT orthosis. Firstly, the mechanism of the system is thoroughly evaluated. After that dynamic behavior of AIRGAIT orthosis which considers the contribution of the additional bi-articular muscle is proposed. Finally, the tracking performance of the system is improved by using modified computed torque control law. The overall system is evaluated by the experiment without a subject (WoS) and with the participation of a subject (WS). All the subjects who participated in the experiments are healthy and no neurological disease.

Chapter 4: In the fourth chapter, the impedance controller is included in the AIRGAIT system. The joint compliance of the robot orthosis powered by the antagonistic actuator can be controllable via regulating its nominal pressure. With the impedance controller, the system is able to provide assistance according to the patients' disability level. Subsequently, the assist-as-needed training strategy is integrated into the AIRGAIT system. The patients' disability level can be estimated by using load cells. The procedures and experimental tests of the system also provide in details.

Chapter 5: The fifth chapter relates to the troubleshooting of the AIRGAIT robotic orthosis. One of the most important requirements of the rehabilitation device is the ability to detect any malfunctions of the system and provide the procedure to enhance the safety for the patients. In this chapter, the AIRGAIT system is evaluated under some troubles such as sensor faults, PAM broken, and interruption of the power supply, etc. All experiments are conducted without the participation of a subject to confirm the safety function.

Chapter 6: The last chapter includes conclusions of the whole research. It also provides some recommendations for upcoming improvement in the control system of the AIRGAIT orthosis.

Chapter 2

Modeling and control of Pneumatic Artificial Muscles

2.1 Introduction

In recent years, high-compliant and low-cost pneumatic artificial muscles (PAMs) have been widely implemented in rehabilitation systems [3, 5, 9, 15, 16, 19]. PAMs are shortened in the longitudinal direction and enlarged in the radial direction when being inflated, and they will turn back to their initial form when being completely deflated. PAMs act similar to the human muscle, e.g. the longer muscles produce bigger force and vice versa. Furthermore, these pneumatic muscles are also inherently compliant, which makes them suitable for applying in human-robotic systems. In comparison with the motorized actuators, PAMs are lightweight and have a high power-to-weight ratio. In addition to the aforementioned advantages, the PAM-based applications also have inherent drawbacks, such as very high nonlinearity and uncertainty, and slow response in force generation. These drawbacks make it difficult to model and control PAMs. In order to deal with these drawbacks of PAM, both nonlinear [29, 30, 31, 32] and linear [20, 33] mathematical models are investigated in the literature. However, most of them require too complicated identification procedure and complexity control structure.

2.2 Contributions

This chapter is dedicated to solving these problems, using a simple paradigm and control strategy for handling the sudden increase in pressure and hysteresis behavior of the PAM. Firstly, the updated dynamic models and control schemes of pneumatic muscle in the literature are carefully reviewed. Then, a simple linear mathematical model of pneumatic muscle in antagonistic configuration and the detailed procedure for deriving the model parameters are also introduced. Finally, this chapter includes the control law for the antagonistic actuators. In advances, the tuning procedure for obtaining control parameters is also provided.

2.3 Literature Review About Modeling and Control of PAMs

Although PAMs have many advantages such as natural compliant, lightweight, and high ratio of weight to power, the challenges which PAM must overcome are very high nonlinear and uncertain characteristic, slow response in force generation. Hence, modeling and control of PAM have attracted a lot of attention in recent years.

2.3.1 Three-element Nonlinear Model

Using a nonlinear mathematical model to describe the nonlinear characteristic of the PAMs is the most common choice of researchers. In 2003, D. B. Reynolds *et al.* introduced the three-element model of PAM which consists of a contractile (force-generating) element, spring element, and damping element in parallel as demonstrates in Fig. 2.1 [29]. In this model, the displacement y of the PAM from the completely deflate can be described by the following equation.

$$M\ddot{y} + B\dot{y} + Ky = F - Mg \quad (2.1)$$

where K is the spring coefficient, B is the damping coefficient, and F is the effective force provided by the contractile element. M is the mass which is picked up by the PAM and g is gravity acceleration. The relationship between the

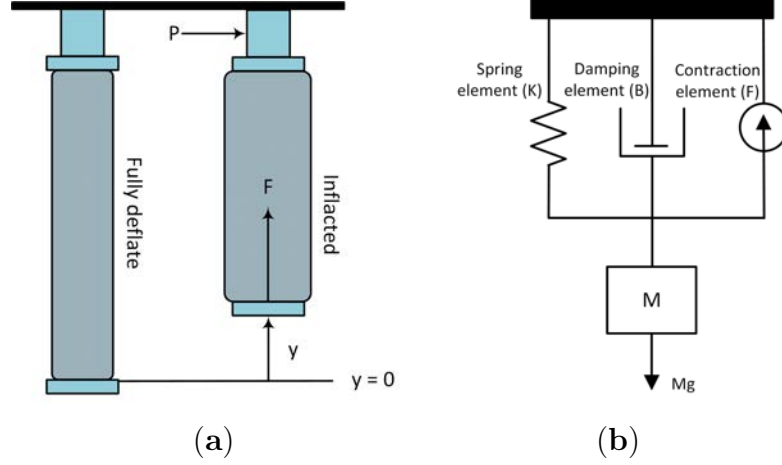


Figure 2.1: The AIRGAIT System: (a) The schematic diagram of PAM. (b) The three-element model of PAM.

coefficients K , B , and F and pressure of PAM (P) can be represented by the linear function.

$$K(P) = K_0 + K_1P \quad (2.2)$$

$$F(P) = F_0 + F_1P \quad (2.3)$$

$$B(P) = B_{0i} + B_{1i}P \text{ (inflation)} \quad (2.4)$$

$$B(P) = B_{0d} + B_{1d}P \text{ (deflation)} \quad (2.5)$$

Note that the damping coefficient depends on the PAM status which is inflated or deflated.

Base on McKibben model K.Xing *et al.* developed the sliding mode control (SMC) based on a nonlinear disturbance observer to improve the tracking performance of a single PAM-mass system [30]. A boundary layer augmented SMC and its modified versions have also been developed for both antagonistic configuration of PAMs and robot orthosis actuated by PAMs [12, 14, 22, 23, 24, 34, 35]. However, the procedure to identify this model's parameters remains complicated with at least two separate experiments: one experiment for determining spring (K) and contractile (F) coefficients and another experiment for estimating damping (B) coefficient. Each experiment must be carried out in three steps [30]. Besides, the parameters of the damping (B) coefficient must be obtained by measuring the load's acceleration, which is very sensitive to external noise. For this reason, it is difficult to obtain the model's parameters with a high accuracy.

2.3.2 The Hysteresis Model

To deal with hysteresis of PAMs, many hysteresis models have been proposed recently, e.g. Maxwell-slip model [32], Prandtl-Ishlinskii model [36], and Preisach model [37]. In these reports, the dynamic characteristic of PAMs was described by an equivalent pressure/length hysteresis model. The obtained models were used in the feedforward term of the cascade position control scheme for hysteresis compensation. The inner loop of the controllers was designed to regulate the inside pressure of the muscles. The outer loops were designed to deal with the nonlinearity of the PAMs characteristic. Both of the loops use a PID-based control strategy. Consequently, some authors continued to develop the modified hysteresis model for both single PAM-mass system and PAMs in antagonistic configuration [38, 39]. However, they mainly focused on modeling of PAMs. Only the trajectory-tracking experiments with low frequency, e.g. up to $0.2Hz$, were conducted in literature. Furthermore, enhanced PID control methods, which were most widely used in these studies, could not deal with hysteresis of PAMs. For example, in Maxwell-slip model, the contracting force of the PAM can be

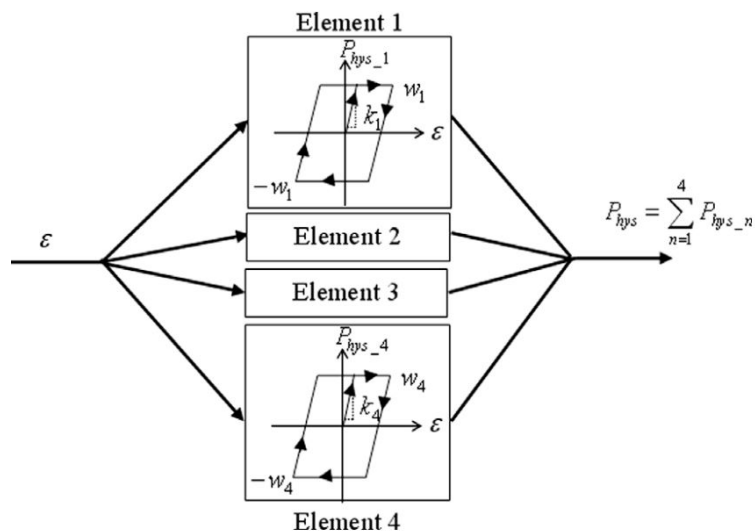


Figure 2.2: The PAM Maxwell-slip model. Description of the predicted pressure output: four Maxwell-slip elements are intuitively selected, the output prediction of the extracted hysteresis pressure P_{hys} is the sum of the individually contributing outputs $P_{hys1, \dots, 4}$ of these elements.

derived as equation

$$F_{isob} = P \sum_{i=0}^2 C_i \varepsilon^i + \sum_{j=0}^3 C_j \varepsilon^j + F(f(\varepsilon), F_{hys}(\varepsilon_n)) \quad (2.6)$$

in which F_{isob} is the measured static contracting force from the isobaric experiment. F_{hys} is the extracted force/length hysteresis. C_i, C_j are the coefficients of the polynomial function, P the internal pressure of the muscle, and ε is the contraction ratio defined as the ratio of the difference between the maximum length l_{max} and the actual length l to the maximum length of the muscle:

$$\varepsilon = \frac{l_{max} - l}{l} \quad (2.7)$$

Secondly, the pressure/length hysteresis model was obtained by the following equation

$$P_{isob} = \frac{F_{isom} - \sum_{j=0}^3 C_j \varepsilon^j}{\sum_{i=0}^2 C_i \varepsilon^i} + P(p(\varepsilon), P_{hys}(\varepsilon_n)) \quad (2.8)$$

Comparing (2.6) and (2.8), one obtains:

$$P_{hys} = P(p(\varepsilon), P_{hys}(\varepsilon_n)) = F^{-1}(f(\varepsilon), F_{hys}(\varepsilon_n)) \quad (2.9)$$

Modeling the pressure/length hysteresis of PAM is derived by the following steps:

- Extracting the pressure/length hysteresis loop experimentally.
- Shrinking the upper (or lower) half of extracted hysteresis loop to get the virgin curve.
- Picking up intuitively the segments which represent the Maxwell-slip elements, a kind of piecewise linearization of the virgin curve.
- Identifying the representing parameters for those selected elements.

Finally, the prediction of the output hysteresis pressure inside the PAM can be represented by four Maxwell-slip elements as shown in Fig. 2.2.

The obtained model was used for the feedforward term of the cascade position control scheme. The inner loop of the controller was designed to cope with the nonlinearity of the PAM's pressure. The outer loop was designed to deal with

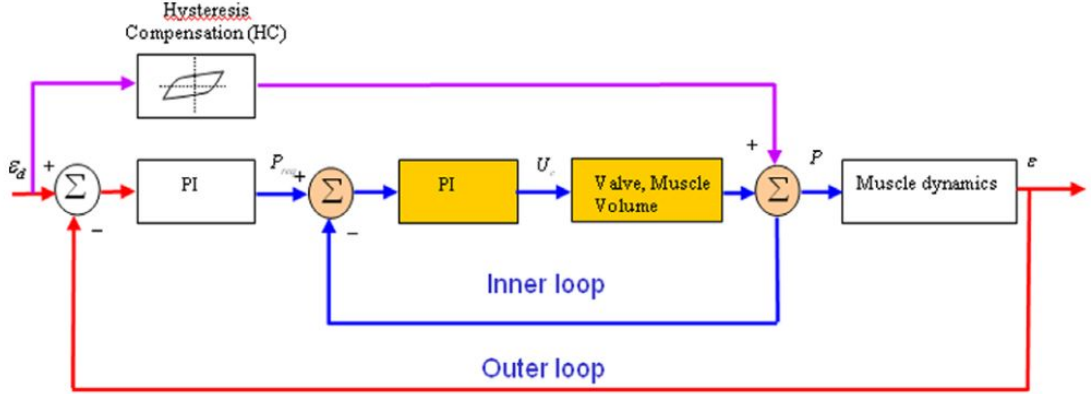


Figure 2.3: The scheme of the cascade position control of the single PAM based Maxwell-slip model.

the nonlinearity of the PAM characteristic. The detail of the cascade control scheme is illustrated in Fig. 2.3. Consequently, Tri Vo Minh *et al.* continue to develop the hysteresis model for both single PAM-mass system and PAMs in antagonistic configuration [38, 39]. However, the authors focused mostly on the modeling of PAM. Only the trajectory tracking experiments with low frequency i.e. up to 2 Hz were conducted in literature. Furthermore, the enhanced PID control method which most widely used in these researches cannot deal with the hysteresis characteristic of PAM.

2.3.3 The Nonlinear Grey-Box Experimental Model

In 2015, to deal with the uncertain nonlinear characteristic of PAMs, Dang Xuan Ba *et al.* introduced the Grey-Box experimental model which consisted of uncertain, unknown, and nonlinear terms. The experimental setup for identifying the Grey-Box model of PAM was shown in Fig. 2.4.

According to Newton's second law, the load dynamics of the system can be presented as

$$\ddot{x} = f_1(x, \dot{x}, m, g, E, t_k, \mu, \theta_0, l_{s0}, k, L_{s0}, \vartheta_{f1}) + g_1(x, m, L_0, \theta_0, \vartheta_{g1}) \quad (2.10)$$

where f_1 is a nonlinear function of the system position or contraction length x , the system velocity \dot{x} , the system mass m (including the moving bar and load), the gravitational acceleration g , the elastic modulus E of the rubber, the thickness

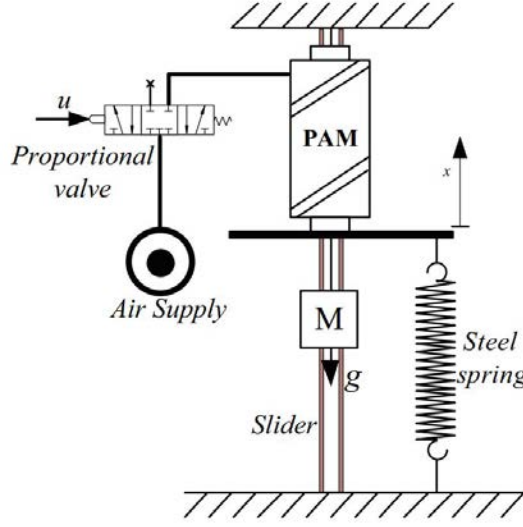


Figure 2.4: Experiment setup of the Grey-Box model of single PAM.

t_k of the rubber sleeve, the friction coefficient μ , the initial braiding angle θ_0 , the stiffness k , the pre-strained distance l_{s0} of the spring, the initial length L_0 of the actuator, the un-modeled term ϑ_{f1} ; g_1 is another nonlinear function of (m, g, L_0, θ_0) and the un-modeled term ϑ_{g1} ; and P is the absolute pressure inside the actuator.

In this report, the pressure dynamics of the system can be derived as follows:

$$\ddot{P} = f_2(x, P, L_0, \theta_0, \gamma, \vartheta_{f2}) + g_2(x, P, P_s, L_0, \theta_0, R, T, \psi, \gamma, K_\nu, \vartheta_{g2})u \quad (2.11)$$

where f_2 is a nonlinear function of (x, P, L_0, θ_0) , the specific heat ratio γ , and the un-modeled term ϑ_{g2} ; and g_2 is a nonlinear combination of $(x, P, L_0, \theta_0, \gamma)$, the supply pressure P_s , the universal gas constant R , the gas temperature T , the orifice function ψ , the valve coefficient K_ν , and the unmodeled term ϑ_{g2} . From (2.10) and (2.11), the system dynamics can be presented by a gray-box model as following equation:

$$\ddot{x} = Y(x, \dot{x}, \ddot{x}, P) + N(x, P)u \quad (2.12)$$

where $Y(\cdot)$, $N(\cdot)$ are the offset function and activation function of the system, respectively. Based on the built in model, the authors employed a sliding mode control (SMC) strategy [31] and an integrated intelligent nonlinear control method [40] for the tracking purpose. The control performance is much improved and the system is able to tracking the 10° amplitude sinusoidal signal with 1.5 Hz

of frequency. The Grey-box method is also reported in the works of Robinson *et al.* in 2016 [41] and by L. Cveticanin *et al.* in 2018 [42]. The relationships angle/torque and force/pressure are thoroughly investigated in the wide range of pressure. However, only the mathematical model was considered and verification in or can track only the low rate of desired trajectories.

2.3.4 The Linearized Model of Single PAM

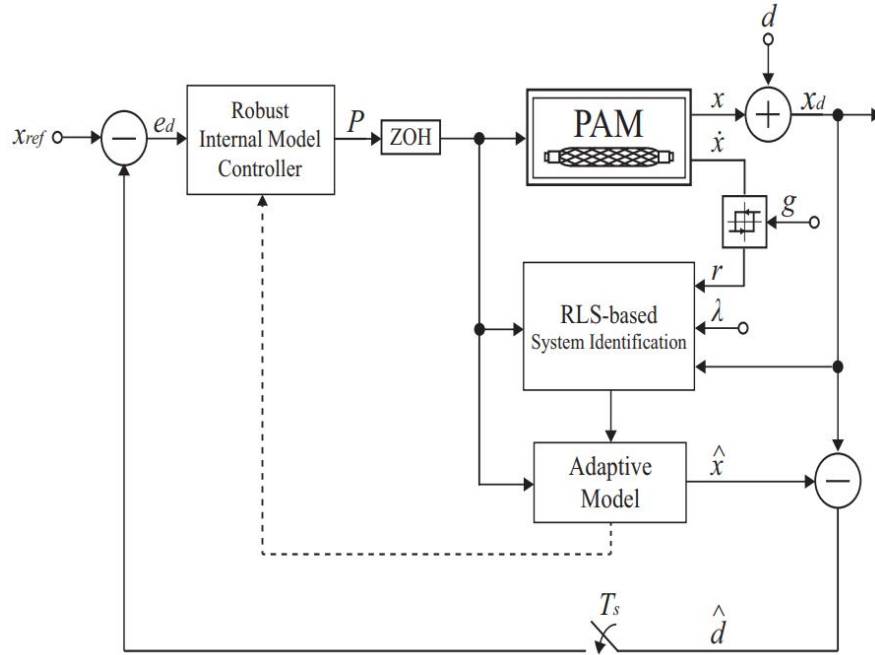


Figure 2.5: Robust Adaptive Internal Model Control Structure.

Due to the complicated in identification procedure and control design of the nonlinear approach, a linearized model of PAM is introduced by G. Andrikopoulos in [33]. In this research, the linearized model named Auto Regressive Moving Average (ARMA) was chosen to approximate the characteristic of PAM as follow

$$A(z)\tilde{x}(n) = B(z)P(n - k) \quad (2.13)$$

where $\tilde{x}(n)$ is the estimated PAM's displacement from its relaxed position, $P(n)$ is the pressure of the air supplied into the PAM and $k \in Z^+$ is the system delay. $A(z)$ and $B(z)$ are polynomials with respect to the backward shift operator z^{-1}

and defined by the following equations:

$$A(z) = 1 + \sum_{i=1}^{n_a} a_i z^{-i}, B(z) = 1 + \sum_{i=1}^{n_b} b_i z^{-(i-1)} \quad (2.14)$$

where $n_a, n_b \in R$ are the maximum orders of the denominator and numerator, respectively. All the model parameters are identified by using Recursive Least Square (RLS) algorithm. The robust adaptive internal model control technique (IMC) as shown in Fig. 2.5 was adopted for trajectory purpose. However, this system is able to achieve an acceptable tracking performance and low frequency i.e 0.05Hz of the sinusoidal reference signal. Recently, the linearized models of PAMs which combined with non-linear control strategies have been proposed for tracking purpose [43, 44, 45, 46, 47, 48, 49]. The control performances of these systems have been significantly improved and can track the 0.5Hz sinusoidal signal with tracking errors are about 3°.

However, in the AIRGAIT robotic orthosis, there are six PAMs are set up in an antagonistic configuration. If the control system is designed base on the single PAM, we will use overall six controllers for all muscles. Hence the control system becomes much complicated. In the next section, a simple and more effective control algorithm for PAMs in the antagonistic configuration is presented.

2.4 Feedforward-Feedback Control of an Antagonistic Actuator

In this section, a linearized model of PAMs in the antagonistic configuration is introduce with the simple identification procedure. Consequently, a modified feedforward-feedback control strategy is also developed for the joint angle tracking purpose.

2.4.1 The Discrete-time Second Order Plus Dead Time (SOPDT) Model of an Antagonistic Actuator

A typical configuration of antagonistic configuration of PAMs is shown in Fig.2.6a, and the proposed experiment platform is demonstrated in Fig.2.6b. The experimental system consists of two PAMs which have 1.0 inches of diameter and 22

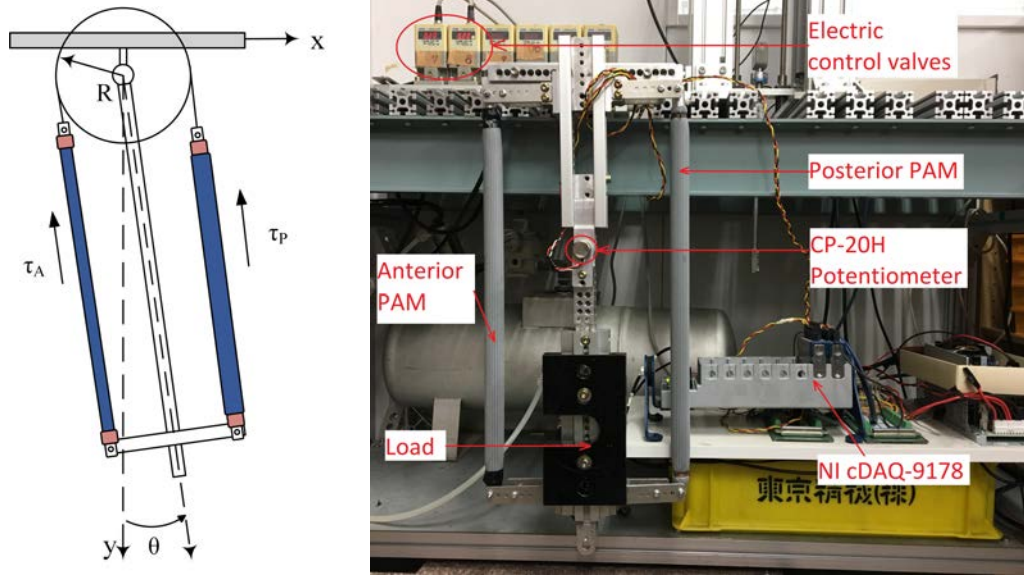


Figure 2.6: (a) The typical antagonistic configuration of two PAMs and (b) the experiment platform of an antagonistic actuator powered by PAMs.

inches of length. The PAMs are fabricated at our local institute. The pressures inside each PAMs are regulated by two proportional electric control valves series ITV 2030-212S-X26 from SMC company. One potentiometer CP-20H from Midori Precision, Japan is used to measure the actuator's angle. All the control system is implemented by using computer-based controller NI cDAQ-9178 from National Instrument, USA. The real-time controller collects the data from the potentiometer via analog input module and sends the control signal to the electric control valve via analog output modules. The developed control algorithm is implemented and compiled by the Labview software before downloading to the hardware controller.

Base on the geometry of the typical antagonistic configuration which is illustrated in Fig.2.6a, the length of each PAMs can be obtained from the measured joint angle, as in the following equations:

$$y_A = y_{AN} + R\theta \quad (2.15a)$$

$$y_P = y_{PN} - R\theta \quad (2.15b)$$

where y_{AN} and y_{PN} are the nominal length of the anterior and posterior PAMs when the joint angle $\theta = 0$. R is the rotation radius of the actuator. Because two similar PAMs are used in the system, we can consider that $y_{AN} = y_{PN} = y_N$.

Table 2.1: Initial parameters of PAMs.

| Parameters | y_0 [in] | y_N [in] | P_0 [MPa] |
|------------|------------|------------|-------------|
| Values | 22 | 15 | 0.2 |

Following that, the relationship between contraction of PAMs and measured angle can be expressed as

$$\varepsilon_A = \frac{y_0 - y_A}{y_0} \times 100\% = \frac{y_0 - (y_N + R\theta)}{y_0} \times 100\% \quad (2.16a)$$

$$\varepsilon_P = \frac{y_0 - y_P}{y_0} \times 100\% = \frac{y_0 - (y_N - R\theta)}{y_0} \times 100\% \quad (2.16b)$$

where y_0 is the length of PAMs in the complete deflation state. In (2.16), y_0 and y_N are fixed by the deflation and nominal lengths of PAMs. Therefore, the contraction of PAMs can be expressed as the function of the measured joint angle θ . As a result, the dynamic behaviour of an antagonistic muscle can be described by a single input single output (SISO) system, in which the input is the difference pressure of two PAMs (ΔP), and the output is the measured angle θ . The input pressure inside the anterior and posterior PAMs can be expressed as

$$P_P = P_0 + \Delta P \quad (2.17a)$$

$$P_A = P_0 - \Delta P \quad (2.17b)$$

where P_0 is the nominal pressure which determines the initial position of antagonistic actuator. The nominal pressure can be chosen so that the joint has the desired compliance for a specific application. It is fixed, so ΔP is chosen as a control variable of trajectory-tracking controller. All the system parameters P_0 , y_0 , and y_N are provided as in Table 2.1. In this research, the following discrete-time SISO system is chosen to describe the model of antagonistic actuator:

$$y_{k+1} = - \sum_{i=1}^n a_i y_{k-i+1} + \sum_{j=1}^m b_j u_{k-j-d+1} + p_k \quad (2.18)$$

where u_k represents the control pressure ΔP , y_k is the joint angle, d is a positive integer representing the dead time of the system (as a number of the sampling time), p_k is the unknown disturbance of the system, a_i and b_j are the model parameters with $b_1 \neq 0$, n and m are integers which satisfy $n \leq m$. The model

2.4 Feedforward-Feedback Control of an Antagonistic Actuator

parameters of the system are obtained by the identification experiment. To verify the mathematical model of PAM, the following experiment procedure is carried out.

Step 1: The initial position of the actuator is set at 0° by supplying nominal pressure P_0 to each PAMs of the actuator.

Step 2: The actuator angle can be changed by sending different types of control signal to the electrical control valves. Three types of control signals are used in this experiment:

- Step response: The control signal is a step wave with the final values 0.2, 0.4, 0.5, and 0.8 *MPa*.
- Sinusoidal signal: The control signal is the 0.2 *MPa* amplitude sinusoidal signal, where frequency varies from 0.2 to 1.0 *Hz*.
- A sine wave signal with time-varying amplitude and frequency, as in the following equation:

$$u(t) = A\sin(2\pi ft) + 0.8A\sin(2\pi 0.2ft) + 0.5A\sin(2\pi 1.5ft) + 0.2A\sin(2\pi 3ft) \quad (2.19)$$

where $A = 0.05\text{MPa}$ and $f = 0.5\text{Hz}$ are the basis amplitude and frequency of the control signal, respectively.

All the data, including control signals and measured angles of actuator, are recorded with sampling time $T_s = 5\text{ms}$ for further analysis.

Step 3: The discrete-time SOPDT, in which $m = n = 2$, is chosen as the mathematical model of the actuator with good accuracy. The precise values of the model's parameters are estimated by using the MATLAB software and provided in Table 2.2.

Figure 2.7 shows identification results: (a) the control inputs are step of 0.4 *MPa*, (b) 0.5 *Hz* sine wave signal, and (c) time-varying amplitude and frequency sinusoidal signal. The discrete-time SOPDT mathematical model depicts a good approximation of nonlinear behaviour of the antagonistic actuator. The maximum error of the estimated angle (dash red line) from the measured one (blue

2.4 Feedforward-Feedback Control of an Antagonistic Actuator

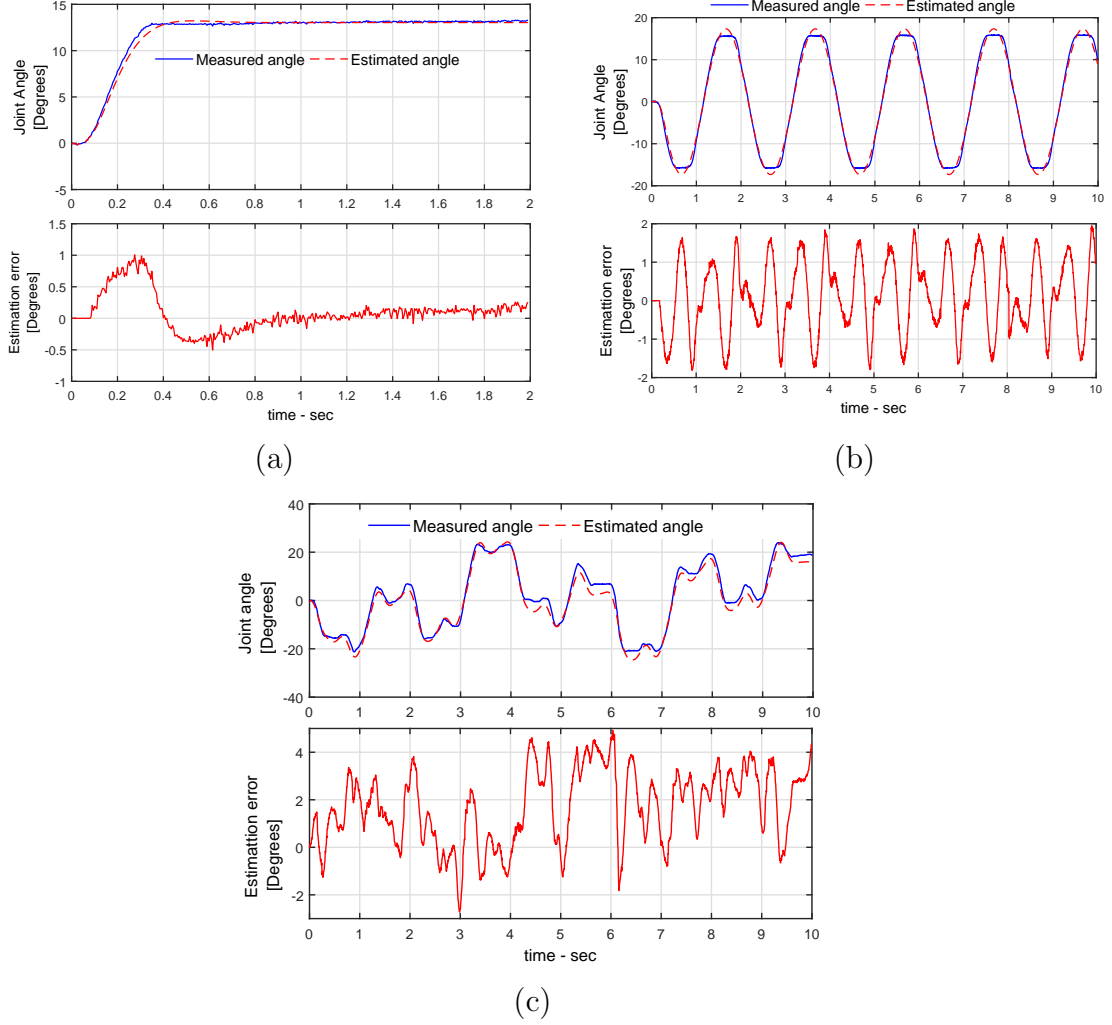


Figure 2.7: Identification results of the antagonistic actuator: (a) the step input of 0.4 MPa , (b) the 0.5 Hz sinusoidal signal, and (c) the time-varying amplitude and frequency control input. Upper sub-figures show measured (blue line) and estimated (dash red line) values of the actuator angle. Lower sub-figures show the estimation errors of the mathematical model.

line) is less than 5.0° , and the root mean square error did not exceed 2.5° . The mean values and standard deviations (SD) of the model parameters obtained by different types of control signals are provided in Table 2.2. As seen in Table 2.2, the standard deviations of the model parameters are much smaller than their mean values. Therefore, we can conclude that the model parameters obtained by different methods have similar values. As a result, we can use any aforementioned method for the identification purpose. The model parameters of

Table 2.2: Identified Parameters of the Antagonistic Actuator.

| Model parameters | a_1 | a_2 | b_1 | b_2 | d |
|-----------------------|--------------|--------------|--------------|--------------|------------|
| Value (Mean \pm SD) | -1.9139 | 0.9164 | 0.0472 | 0.0460 | 22 \pm 3 |
| | ± 0.0182 | ± 0.0180 | ± 0.0064 | ± 0.0061 | |

antagonistic muscles which identified by time-varying amplitude and frequency are chosen to design the controller in the next section of this research.

2.4.2 Control Design

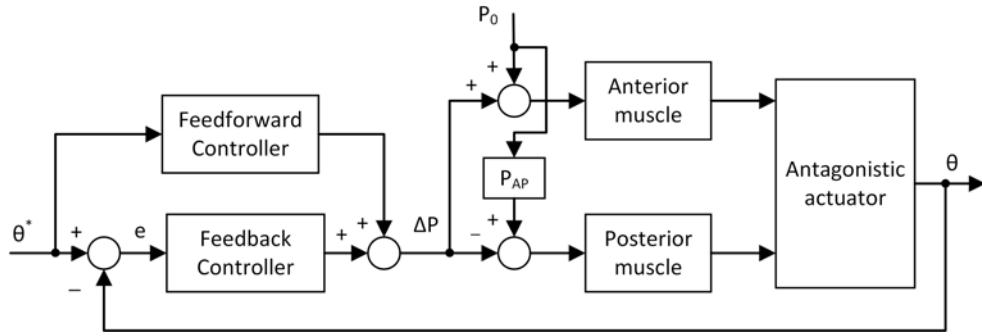


Figure 2.8: The typical block diagram of each joints. P_0 is the nominal pressure supplied to the PAMs, P_{AP} is the different pressure of two PAMs.

The feedforward-feedback control approach has been developed in the two last decades. The stable-inversion methodology is developed by S. Devasia [50] demonstrates good performance in output tracking. However, this control method is very sensitive to the modeling error and disturbances [51]. To overcome these unfavorable effects, the inverse feedforward is often combined with a feedback controller. In this research, we proposed a modified feedforward-feedback controller for the trajectory tracking control of the robot orthosis. The block diagram of the control system is shown in Fig. 2.8, where $G_P(z^{-1})$ is the transfer function of antagonistic muscle, $G_{FF}(z^{-1})$ and $G_{FB}(z^{-1})$ are the feedforward and feedback controllers, respectively. The transfer function of the entire system can be described as

$$G_{total}(z) = \frac{\theta_{i,k}}{\theta_{i,k}^*} = \frac{[G_{FF}(z^{-1}) + G_{FB}(z^{-1})] G_P(z^{-1})}{1 + G_{FB}(z^{-1})G_P(z^{-1})} \quad (2.20)$$

2.4.2.1 The Feedforward Controller

The feedforward controller is designed based on the inverse system dynamics:

$$G_{FF}(z^{-1}) = \hat{G}_P^{-1}(z^{-1}) \quad (2.21)$$

in which $\hat{G}_P^{-1}(z^{-1})$ is the modified inverse part of the plant transfer function $G_P(z^{-1})$ in (2.20) and can be simplified as

$$G_{FF}(z^{-1}) = \frac{1 + a_1 + a_2}{b_1 + b_2} z^d \quad (2.22)$$

From (2.22), it can be realized that the feedforward controller is capable of eliminating the dead time of the plant by utilizing the d step ahead value of the desired trajectory.

2.4.2.2 The Feedback Controller

The proportional integral (PI) controller is chosen for the feedback loop. The parameters of the PI controller are obtained based on the internal model control (IMC) tuning method. According to the IMC design procedure in [33], the PI controller transfer function can be formulated as

$$G_{FB}(z^{-1}) = \frac{G_f(z^{-1})}{\tilde{G}_P^-(z^{-1})[1 - G_f(z^{-1})\tilde{G}_P^+(z^{-1})]} \quad (2.23)$$

where $G_f(z^{-1})$ is a first order discrete-time low-pass filter (DLPF) with unity gain, which is connected in series with IMC controller to avoid the noncausal problems of the inverse model; $\tilde{G}_P^-(z^{-1})$ and $\tilde{G}_P^+(z^{-1})$ are the invertible and non-invertible elements of the antagonistic actuator model, respectively. The transfer function of the DLPF is described by

$$G_f(z^{-1}) = \frac{a_f}{1 - b_f z^{-1}} \quad (2.24)$$

where $a_f = \frac{1}{1 + \alpha}$, $b_f = \frac{\alpha}{1 + \alpha}$, $\alpha = \frac{1}{2\pi T_s f_c}$, T_s and f_c are the sampling time and cut-off frequency, respectively. From the model equation (2.20) we can obtain

$$\tilde{G}_P^-(z) = \frac{b_1 + b_2 z^{-1}}{1 + a_1 z^{-1} + a_2 z^{-2}} \quad (2.25)$$

$$\tilde{G}_P^+(z) = z^{-(d+1)} \quad (2.26)$$

The general form of the discrete-time PI controller is

$$G_{PI}(z) = \frac{q_0 + q_1 z^{-1}}{1 - z^{-1}} \quad (2.27)$$

in which $q_0 = K_c$, $q_1 = -K_c(1 + \frac{T_s}{T_I})$, K_c and T_I are the proportional gain and integral time of the PI controller, respectively. From (2.24) - (2.27), the parameters of the PI controller can be computed by

$$K_c = \frac{a_f}{(b_1 + b_2)(1 + a_f d)} \quad (2.28)$$

$$T_I = \frac{T_s}{(1 + a_1 + a_2)} \quad (2.29)$$

2.4.3 Experimental Evaluation

2.4.3.1 Experimental Setup

To verify the effectiveness of the proposed control method, multiple-scenario experiment with different desired trajectories is carried out. In the first scenario of the trajectory-tracking experiment, sinusoidal signals with amplitude 20° and 0.2, 0.5, 0.8, and 1 *Hz* frequency are given as desired trajectories. To evaluate the applicability of the proposed control method for a rehabilitation robot, a human-like pattern signal is employed as a desired trajectory in the second scenario of the experiment. The modified knee gait data profile in textbook [52], where the maximum flexion angle is set at 28° , is used to verify the control performance. In both experimental scenarios, the system is tested under two load conditions: no load and load $m = 2.5 \text{ kg}$.

In all experimental scenarios, the sampling time of the discrete-time control system was $T_s = 5 \text{ ms}$. All the data were recorded for ten cycles from the start time of the experiment. The data were processed by MATLAB software version R2016b. The parameters of proposed controller after being well tuned are provided in Table 2.3.

2.4.3.2 Experimental results

Figure 2.9 depicts experiment results when the actuator track the sine wave signals without load. The sinusoidal signal with amplitude of 20° and frequency

2.4 Feedforward-Feedback Control of an Antagonistic Actuator

Table 2.3: The parameters of the controllers

| Parameters | $K_p[V/^\circ]$ | $T_i[s]$ | $K_{FF}[V/^\circ]$ |
|------------|-----------------|----------|--------------------|
| Values | 0.05 | 0.02 | 0.028 |

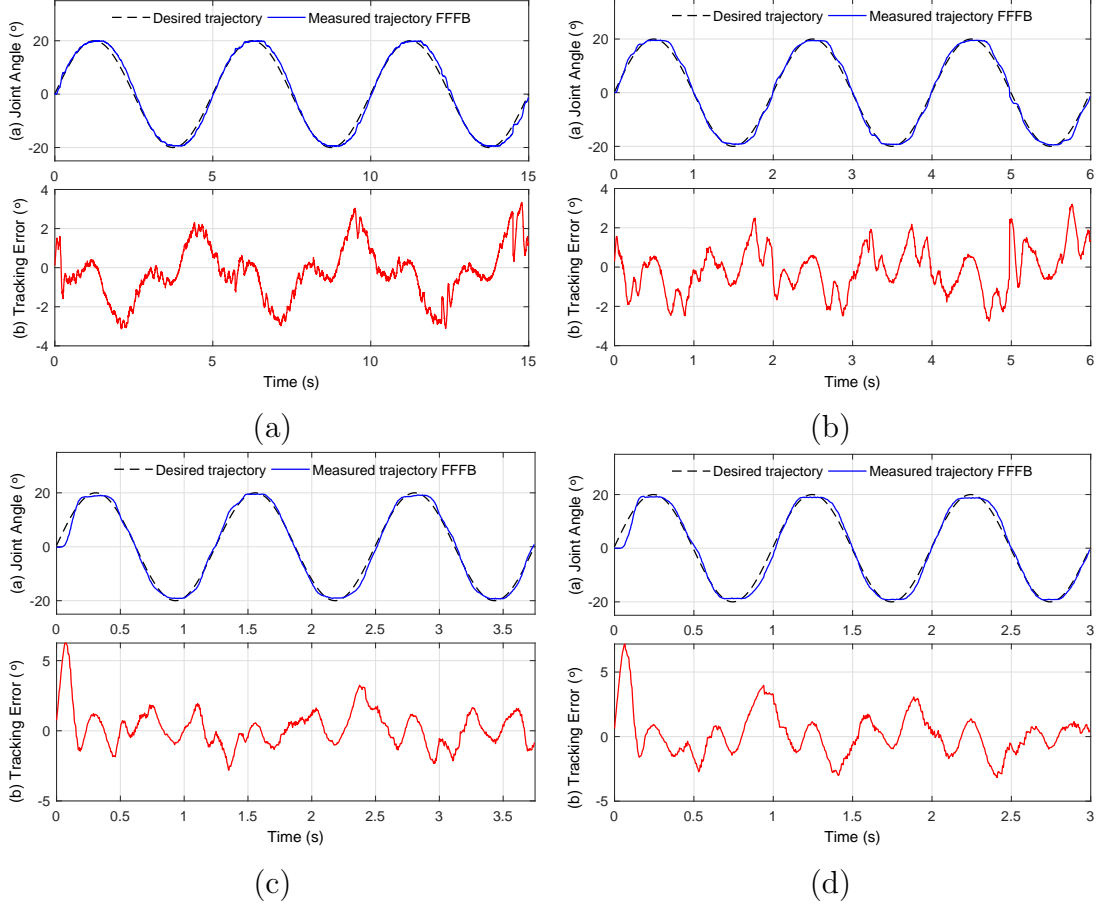


Figure 2.9: Experiment results without a load for tracking a sinusoidal trajectory: (a) 0.2 Hz, (b) 0.5 Hz, (c) 0.8 Hz and (d) 1.0 Hz of signal frequency.

from $0.2Hz$ to $1Hz$. In the second scenario, a knee gait pattern is given as a desired trajectory. The proposed controller is evaluated with two different gait cycle (GC) times: 2.5 seconds and 4 seconds. The experimental results of this scenario are shown in Figure 2.10. In both Figure 2.9 and Figure 2.10, the upper sub-figure of each image includes the desired trajectory (dash-black line) and measured angle controller by the proposed controller (blue line). The lower part of each figure shows the tracking errors of the measured trajectory from desired

2.4 Feedforward-Feedback Control of an Antagonistic Actuator

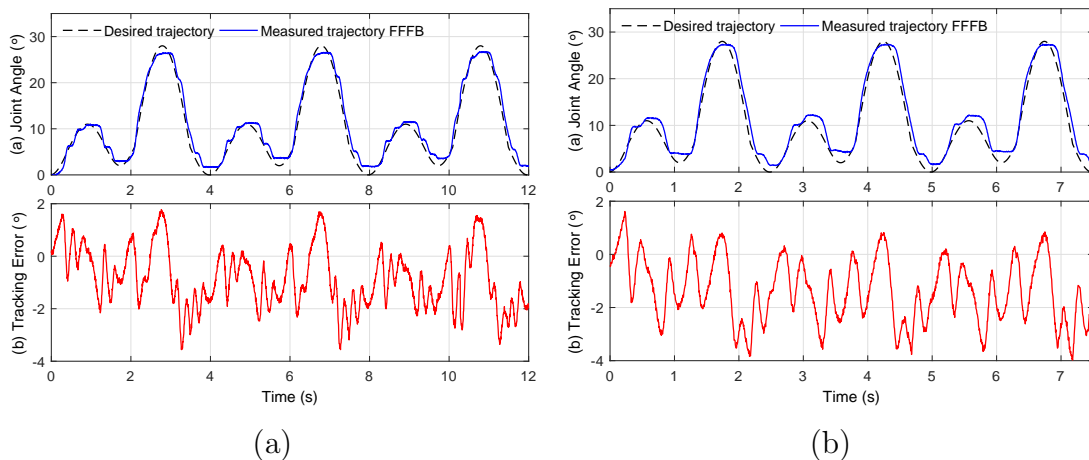


Figure 2.10: Experiment results of the proposed controller and conventional DSMC controller when tracking the human-gait pattern signal: (a) 4 seconds and (b) 2.5 seconds of gait cycle time. The experiment was carried out without a load.

Table 2.4: Experiment results of the FFFB controller.

| Trajectories | MTE | | RMSTE | |
|--------------|---------|--------------------|---------|--------------------|
| | No load | $m = 2.5\text{kg}$ | No load | $m = 2.5\text{kg}$ |
| 0.2Hz | 3.34 | 2.65 | 1.35 | 0.96 |
| 0.5Hz | 3.20 | 4.97 | 1.12 | 1.52 |
| 0.8Hz | 6.25 | 6.90 | 1.26 | 1.77 |
| 1.0Hz | 7.17 | 9.63 | 1.62 | 3.09 |
| Gait 4s | 1.78 | 2.00 | 1.50 | 1.64 |
| Gait 2.5s | 1.61 | 4.95 | 1.93 | 1.81 |

trajectory. As given in Table 2.4, in all scenarios of the experiment, the MTE and RMSTE are less than 8.0° and 2.0° , respectively. When the antagonistic actuator carries a load $m = 2.5\text{ kg}$, the tracking performance is slightly degraded where the MTE and RMSTE are about 10.0° and 3.1° , respectively. Figure 2.12 shows experiment results of all scenarios when the actuator drives 2.5kg of load. The proposed controller achieves a performance comparable to the experimental results with similar configuration and desired trajectory in [49] and [53]. In [49], when tracking a 0.4Hz frequency and 5° sinusoidal signal, the residual

2.4 Feedforward-Feedback Control of an Antagonistic Actuator

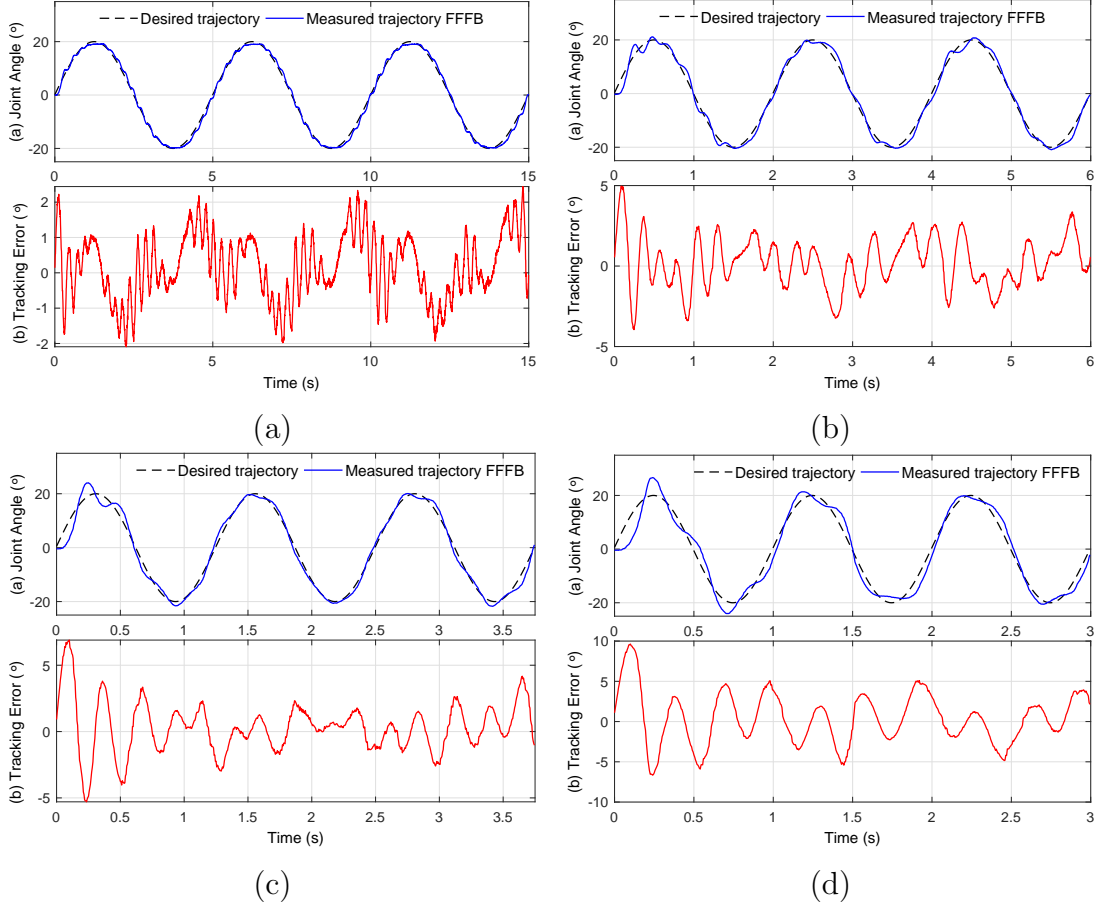


Figure 2.11: Experiment results with 2.5kg of load for tracking a sinusoidal trajectory: (a) 0.2 Hz, (b) 0.5 Hz, (c) 0.8 Hz and (d) 1.0 Hz of signal frequency.

error amplitude is 0.5° equivalent to 10%. When tracking a 0.5 Hz frequency and 20° amplitude sinusoidal signal, the RMSTE of the proposed controller is 1.12° , equivalent to 6.06% of amplitude. This result is better than the one in [53], in which a sinusoidal signal with 40° amplitude and frequency 0.25Hz is used as a desired trajectory. The experiments also show that the proposed controller can track a human-gait pattern with the MTE of less than 5° . This result is in accordance with the commercial gait training system LOKOMAT [26], in which the MTE is 15° . It is shown that the built-in model and proposed controller can be applied in robot gait training system. In the next section of this chapter, the tracking performance of the antagonistic actuator continue to be improve by employing the nonlinear control strategy.

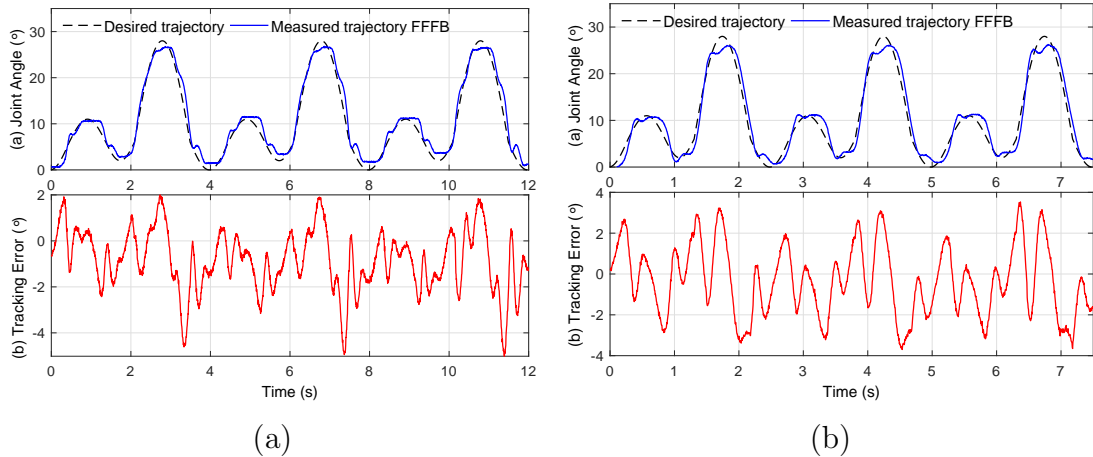


Figure 2.12: Experiment results for the proposed controller and conventional DSMC controller when tracking the human-gait pattern signal with a load $m = 2.5$ kg: (a) 4 seconds and (b) 2.5 seconds of gait cycle time

2.5 Fractional Order Integral Sliding Mode Control Strategy

2.5.0.1 Fractional Order Calculus

Recently, the fractional order calculus has become an interesting topic and extensively used in control design [54, 55, 56]. In comparison with the conventional controllers based on integer order integrator and differentiator, the fractional order controller offers more degree of freedom which can be utilized to further improve the performance of the control system.

Fractional-order calculus is a generalization of the integration and differentiation from integer to non-integer order. This section introduces only definitions which are widely used in the area of control system.

First, the gamma function $\Gamma(z)$ which is the extension of the factorial for non-integer number z is introduced

$$\Gamma(z) = \int_0^{\infty} e^{-t} t^{z-1} dt \quad (2.30)$$

The most important property of the gamma function is

$$z\Gamma(z) = \Gamma(z + 1) \quad (2.31)$$

Then, the definition of derivative of order $\alpha \in \mathbb{R}$ is presented. In continuous-time domain, the most often used one is the *Riemann-Liouville* definition

$${}_{t_0}^{\alpha} D_t f(t) = \frac{1}{\Gamma(n - \alpha)} \frac{d^n}{dt^n} \int_{t_0}^t \frac{f(\tau)}{(t - \tau)^{n-\alpha-1}} d\tau \quad (2.32)$$

where t_0 and t are the limits and n is an integer number satisfying $n - 1 < \alpha < n$. In practical applications where computer-based control devices are used, the following *Grünwald – Letnikov* definition with *short memory principle* is preferred:

$${}_{t_0}^{\alpha} D_t f(t) = T_s^{-\alpha} \sum_{j=0}^{\lfloor \frac{t-t_0}{T_s} \rfloor} (-1)^j \binom{\alpha}{j} f(t - jT_s) \quad (2.33)$$

in which $\lfloor \cdot \rfloor$ means the integer part, T_s is the sampling time and $\binom{\alpha}{j}$ is the binomial coefficient defined by

$$\binom{\alpha}{j} = \frac{\Gamma(\alpha + 1)}{\Gamma(j + 1)\Gamma(\alpha - j + 1)} \quad (2.34)$$

In *math.h* library of *C* compiler, the gamma function $\Gamma(z)$ is already supported. The syntax of this function is

$$\text{float } \text{tgamma} (\text{float } z) \quad (2.35)$$

Hence, (2.30) and (2.33) can easily be implemented in digital control systems.

2.5.1 Fractional Order Integral Approximation

Fractional-order calculus is a generalization of the integration and differentiation from integer to non-integer order. This appendix introduces only definitions which are widely used in the area of control systems. First, gamma function $\Gamma(z)$, which is the extension of the factorial for non-integer number z , is introduced as

$$\Gamma(z) = \int_0^{\infty} e^{-t} t^{z-1} dt \quad (2.36)$$

The most important property of the gamma function is

$$z\Gamma(z) = \Gamma(z + 1) \quad (2.37)$$

Then, the definition of integral of order $\alpha \in \mathbb{R}$ is presented. In continuous-time domain, the most often used one is the *Riemann-Liouville* definition:

$${}^{\alpha}\Xi e(t) = \frac{1}{\Gamma(\alpha)} \int_0^t (t - \tau)^{(\alpha-1)} e(\tau) d\tau \quad (2.38)$$

At this time, the FOI is not supported in any programming language. For this reason, its numerical approximation is required to implement the FOI in any real-time control system. In a digital control system with sampling time T_s , interval $(0, t)$ can be approximated by $k = \frac{t}{T_s}$ sub-intervals. Therefore,

$${}^{\alpha}\Xi e(t) = \frac{1}{\Gamma(\alpha)} \sum_{j=1}^k \int_{jT_s}^{(j+1)T_s} (t - \tau)^{(\alpha-1)} e(\tau) d\tau \quad (2.39)$$

Consider that T_s is small enough, so that e is constant in each sub-interval. Therefore,

$${}^{\alpha}\Xi e(t) \approx {}^{\alpha}\Xi_{e,k} = \frac{1}{\Gamma(\alpha)} \sum_{j=1}^k \int_{jT_s}^{(j+1)T_s} (t - \tau)^{(\alpha-1)} e(\tau) d\tau \quad (2.40)$$

Following that,

$${}^{\alpha}\Xi_{e,k} = \sum_{j=1}^k [(k - j + 1)^{\alpha} - (k - j)^{\alpha}] \frac{T_s^{\alpha}}{\alpha\Gamma(\alpha)} e_{j+1} \quad (2.41)$$

From (2.37) and (2.41), we have

$${}^{\alpha}\Xi_{e,k} = \sum_{j=1}^k \omega_j e_j \quad (2.42)$$

with the weighting factor ω_j as follows:

$$\omega_j = [(k - j + 1)^{\alpha} - (k - j)^{\alpha}] \frac{T_s^{\alpha}}{\alpha\Gamma(\alpha)}. \quad (2.43)$$

Because of the infinite data in (2.42), the approximation of FIO cannot be directly implemented in any digital system. In this research, the recursive approximation of FIO in [57] is employed. Denote $\Xi_{e,k-1}$ as FIO of the tracking error in the last step, and it can be computed as

$${}^{\alpha}\Xi_{e,k-1} = \sum_{j=2}^k \omega_j e_{j-1} \quad (2.44)$$

From (2.42) and (2.44), we have

$${}^{\alpha}\Xi_{e,k} = {}^{\alpha}\Xi_{e,k-1} + \sum_{j=2}^k \omega_j \tilde{e}_{j-1} + \omega_1 e_1 \quad (2.45)$$

where $\tilde{e}_j = e_j - e_{j-1}$. We apply the *short memory principle* to (2.45) and we can consider two cases:

(a). If $k < N$, where $N = \left\lceil \frac{L}{T_s} \right\rceil$ is the number of considered data samples, then

$${}^{\alpha}\Xi_{e,k} = {}^{\alpha}\Xi_{e,k-1} + \sum_{j=N-k+2}^N \Omega_j \tilde{e}_{N-k+j} + \Omega_{N-k+1} e_1 \quad (2.46)$$

(b). If $k \geq N$,

$${}^{\alpha}\Xi_{e,k} = {}^{\alpha}\Xi_{e,k-1} + \sum_{j=2}^N \Omega_j \tilde{e}_{k-N+j} + \Omega_1 e_{k-N+1} \quad (2.47)$$

where

$$\Omega_j = [(N-j+1)^\alpha - (N-j)^\alpha] \frac{T_s^\alpha}{\Gamma(\alpha+1)} \quad (2.48)$$

The FIO is approximated by equations (2.46) and (2.47), which can be easily implemented in any digital control system.

2.5.2 Control Design

Recently, SMC has been employed for designing the controller for PAMs or systems powered by PAMs [12, 14, 22, 23, 34, 35]. SMC is able to provide highly accurate tracking performance with a bounded error; however, “*chattering*” problem is a big challenge that SMC must overcome. SMC is a suitable control approach for PAM-based systems to deal with their uncertain, nonlinear and time varying characteristics. In this section, we addressed a DFISM to improve the tracking performance of the antagonistic actuator powered by PAMs. The fractional order integral is implemented together with disturbance observer to deal with the “*chattering*” problem. Figure 2.13 illustrates the block diagram of the proposed control system. We consider the following fractional integral sliding surface:

$$S_k = e_k + {}^{\alpha}\Xi_{e,k} \quad (2.49)$$

2.5 Fractional Order Integral Sliding Mode Control Strategy

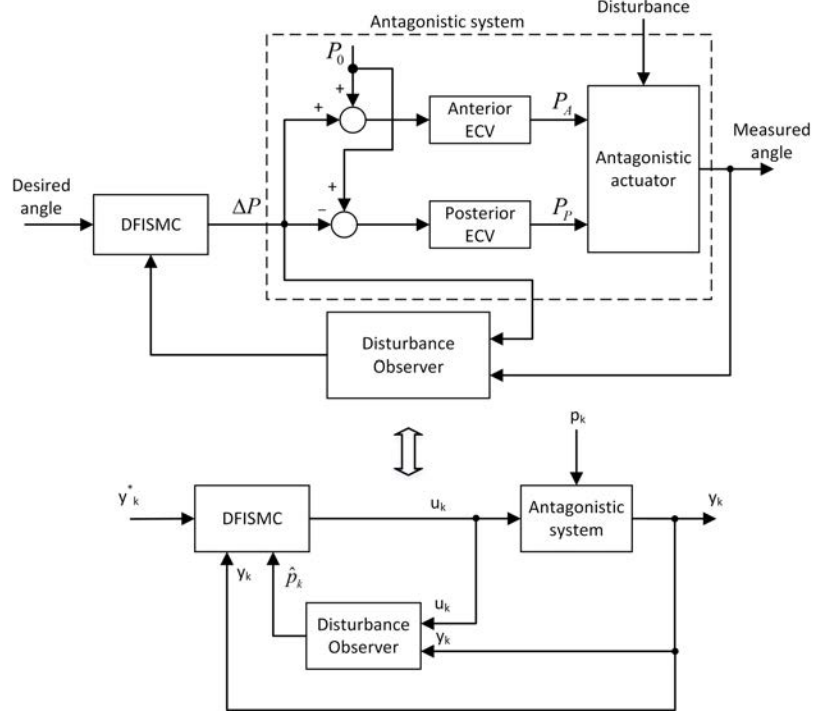


Figure 2.13: Block diagram of the discrete-time fractional integral sliding mode control.

where $e_k = y_k^* - y_k$ is the tracking error with the desired trajectory y_k^* , and ${}^\alpha \Xi_{e,k}$ is the integral of the tracking error with fractional order α and integral gain K_I . ${}^\alpha \Xi_{e,k}$ can be calculated as follows:

$${}^\alpha \Xi_{e,k} = {}^\alpha \Xi_{e,k-1} + K_I \left(\sum_{j=2}^N \Omega_j \tilde{e}_{k-N+j} + \Omega_1 e_{k-N+1} \right) \quad (2.50)$$

and ${}^\alpha \Xi_{e,0} = \omega_N e_0$ at the initial state. We also obtain

$${}^\alpha \Xi_{e,k+1} = {}^\alpha \Xi_{e,k} + K_I \left(\sum_{j=2}^N \Omega_j \tilde{e}_{k-N+j+1} + \Omega_1 \tilde{e}_{k-N+2} \right) \quad (2.51)$$

From (2.49), (2.50), and (2.51), we can obtain

$$S_{k+1} = e_{k+1} + S_k - e_k + K_I \left(\sum_{j=2}^N \Omega_j \tilde{e}_{k-N+j+1} + \Omega_1 \tilde{e}_{k-N+2} \right) \quad (2.52)$$

Therefore,

$$S_{k+1} - S_k = (1 + K_I \Omega_N) e_{k+1} - (1 + K_I \tilde{\Omega}_N) e_k - K_I \sum_{j=2}^{N-1} \tilde{\Omega}_j e_{k-N+j} \quad (2.53)$$

where e_{k+1} is one-step-ahead tracking error, which can be computed from the SISO model of the actuator in (2.18) as

$$e_{k+1} = y_{k+1}^* + \sum_{i=1}^n a_i y_{k-i+1} - \sum_{j=1}^m b_j u_{k-d-j+1} - p_k \quad (2.54)$$

where y_{k+1}^* is one step ahead of the desired trajectory, which is considered to be known when apply the model to a specific application. In (2.18), disturbance p_k is unknown and needs to be estimated. In this study, one-step delayed technique was used to estimate p_k . This technique is based on the following assumptions:

Assumption 1 *Sampling time T_s is sufficiently small and system disturbance p_k is bounded, so the difference between two consecutive time samples is also bounded, i.e.*

$$p_k - p_{k-1} = O(T_s) \quad (2.55)$$

$$p_k - 2p_{k-1} + p_{k-2} = O(T_s^2) \quad (2.56)$$

where $O(T_s)$ is the thickness boundary layer. It means there always exist constants A and B , $\forall k > 0$, such that

$$|p_k - p_{k-1}| \leq AT_s \quad (2.57)$$

$$|p_k - 2p_{k-1} + p_{k-2}| \leq BT_s^2 \quad (2.58)$$

The aforementioned assumption is based on the Taylor expansion as follows. For a very small constant T_s , we have

$$p(t - T_s) = p(t) - \frac{dp(t)}{dt} T_s + \sum_{i=2}^{\infty} (-1)^i \frac{d^{(i)}p(t)}{dt^i} \frac{T_s^i}{i!} \quad (2.59)$$

Then, it can be derived from (2.59) that

$$\begin{aligned} p(t) - p(t - T_s) &= \frac{dp(t)}{dt} T_s - \sum_{i=2}^{\infty} (-1)^i \frac{d^{(i)}p(t)}{dt^i} \frac{T_s^i}{i!} \\ &\approx \frac{dp(t)}{dt} T_s + O(T_s^2) \end{aligned} \quad (2.60)$$

Assume that signal $p(t)$ is smooth, and its differential is bounded. Then there exists a constant A such that

$$|p(t) - p(t - T_s)| \leq AT_s + O(T_s^2) \quad (2.61)$$

which means

$$P(t) - p(t - T_s) = O(T_s) \quad (2.62)$$

and (2.55) holds.

Now, ignore the small term $O(T_s^2)$ and differentiate both sides of (2.60). This gives us

$$\frac{dp(t)}{dt} - \frac{dp(t - T_s)}{dt} \approx \frac{d^2p(t)}{dt^2} T_s \quad (2.63)$$

By using (2.60) on the left side of (2.63),

$$p(t) - 2p(t - T_s) + p(t - 2T_s) \approx \frac{d^2p(t)}{dt^2} T_s^2 \quad (2.64)$$

Again, assume that the second order differential of $p(t)$ is bounded by a constant B , then it leads to

$$|p(t) - 2p(t - T_s) + p(t - 2T_s)| \leq BT_s^2 \quad (2.65)$$

which means that (2.58) holds.

Estimation \hat{p}_k of disturbance p_k can be computed based on (2.18) as

$$\hat{p}_k = 2p_{k-1} - p_{k-2} \quad (2.66)$$

where

$$p_{k-1} = y_k + \sum_{i=1}^n a_i y_{k-i} - \sum_{j=1}^m b_j u_{k-j} \quad (2.67)$$

Hence, the error of estimation \tilde{p}_k is

$$\begin{aligned} \tilde{p}_k &= p_k - \hat{p}_k \\ &= p_k - 2p_{k-1} + p_{k-2} = O(T_s^2) \end{aligned} \quad (2.68)$$

Finally, the one-step-ahead tracking error (2.54) can be expressed by

$$e_{k+1} = y_{d,k+1} + \sum_{i=1}^n a_i y_{k-i+1} - \sum_{j=1}^m b_j u_{k-j+1} - \hat{p}_k - \tilde{p}_k \quad (2.69)$$

When substituting e_{k+1} in (2.54) and $p_k = \hat{p}_k + \tilde{p}_k$ into (2.53), we can obtain

$$\begin{aligned} S_{k+1} - S_k &= -(1 + K_I \tilde{\Omega}_N) e_k - K_I \sum_{j=2}^{N-1} \tilde{\Omega}_j e_{k-N+j} \\ &+ (1 + K_I \Omega_N) \left(y_{k+1}^* + \sum_{i=1}^n a_i y_{k-i+1} - \sum_{j=1}^m b_j u_{k-j-d+1} - \hat{p}_k - \tilde{p}_k \right) \end{aligned} \quad (2.70)$$

Disturbance estimation error \tilde{p}_k is unknown in practice; however, it is very small and bounded by assumption 1. Control signal u_k can be obtained by solving the reaching law $S_{k+1} = 0$ with the absence of \tilde{p}_k as follows:

$$u_k = b_1^{-1} \left(y_{k+1}^* + \sum_{i=1}^n a_i y_{k-i+1} - \sum_{j=1}^m b_j u_{k-j-d+1} - \hat{p}_k \right) - \frac{(1 + K_I \tilde{\Omega}_N) e_k - K_I \sum_{j=2}^{N-1} \tilde{\Omega}_j e_{k-N+j}}{b_1(1 + K_I \Omega_N)} \quad (2.71)$$

Adjusting integral gain K_I and fractional order integral α may improve performance of the control system.

2.5.3 Experimental Evaluation

2.5.3.1 Experimental Procedure

To verify the effectiveness of the proposed control method, the multiple-scenario experiment in section 2.4.3.1 is carried out with the DFISMC controller. In the first scenario of the trajectory-tracking experiment, sinusoidal signals with amplitude 20° and 0.2, 0.5, 0.8, and 1 *Hz* frequency are given as desired trajectories. To evaluate the applicability of the proposed control method for a rehabilitation robot, a human-like pattern signal is employed as a desired trajectory in the second scenario of the experiment. The modified knee gait data profile in textbook [52], where the maximum flexion angle is set at 28° , is used to verify the control performance. In both experimental scenarios, the system is tested under two load conditions: no load and load $m = 2.5 \text{ kg}$.

In all experimental scenarios, the sampling time of the discrete-time control system was $T_s = 5 \text{ ms}$. All the data were recorded for ten cycles from the start time of the experiment. The data were processed by MATLAB software version R2016b. The proposed controller is also compared with the conventional DSMC controller and the FFFB controller in terms of tracking performance. The parameters of both DSMC and DFISMC controllers after being well-tuned are provided in Table 2.5.

2.5 Fractional Order Integral Sliding Mode Control Strategy

Table 2.5: Parameters of the DFISM and conventional DSMC controller.

| Parameters | DFISM | | DSMC | |
|------------|----------|-------|-----------|----------------------|
| | α | K_I | λ | K_{sw} |
| Values | 0.8 | 0.01 | 0.1 | 1.5×10^{-3} |

2.5.3.2 Experimental Results

To quantitatively evaluate the tracking performance, the maximum tracking error (MTE) and root mean square tracking error (RMSTE) are computed.

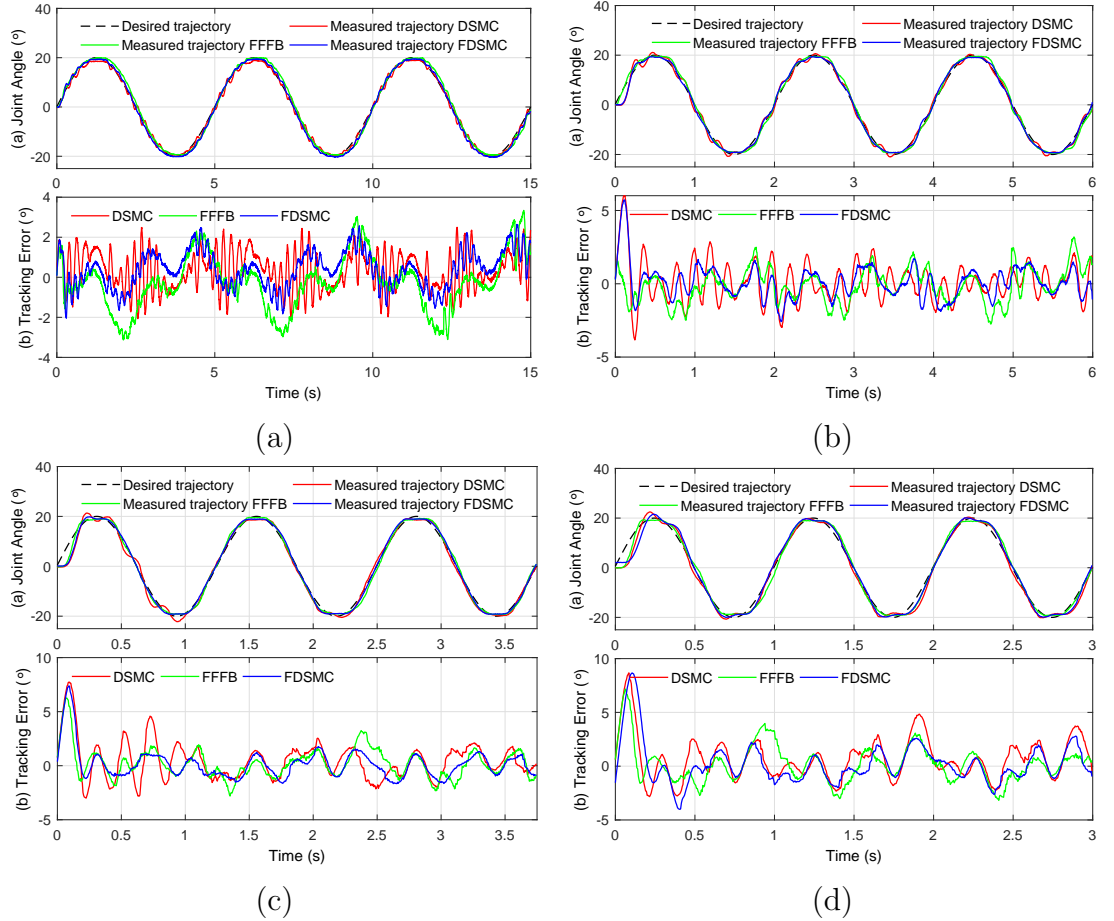


Figure 2.14: Experiment results without a load for tracking a sinusoidal trajectory: (a) 0.2 Hz, (b) 0.5 Hz, (c) 0.8 Hz, and (d) 1.0 Hz of signal frequency.

Figure 2.14 depicts the experimental results when the actuator tracks the sine

2.5 Fractional Order Integral Sliding Mode Control Strategy

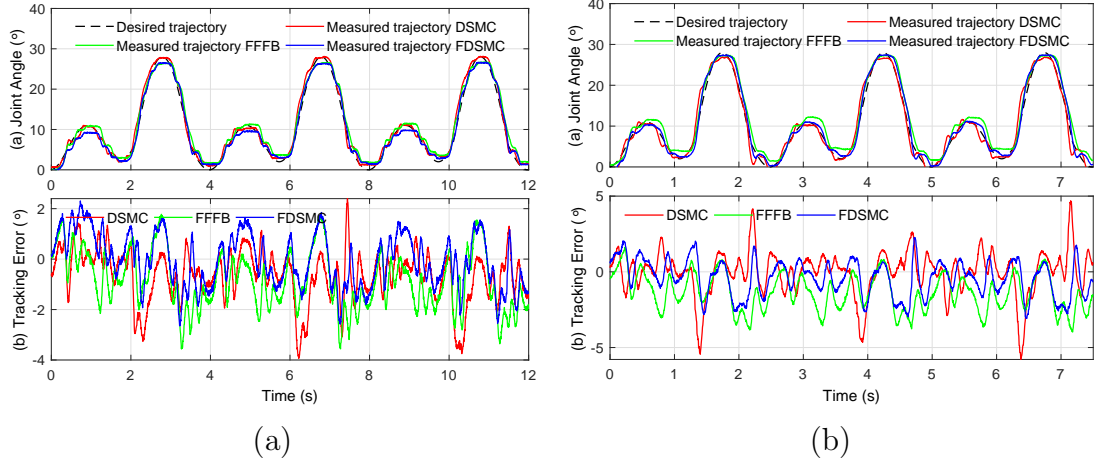


Figure 2.15: Experiment results of the proposed controller and conventional DSMC controller when tracking the human-gait pattern signal: (a) 4 seconds and (b) 2.5 seconds of gait cycle time. The experiment was carried out without a load.

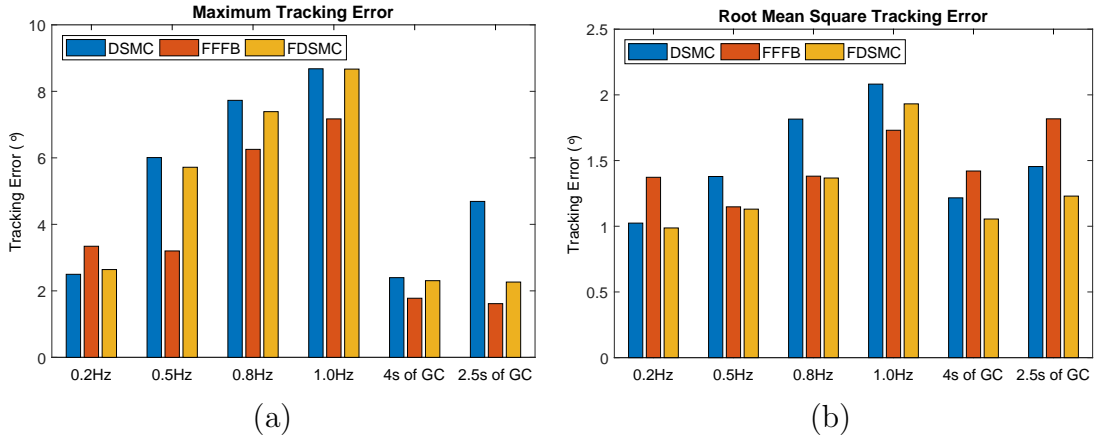


Figure 2.16: MTE and RMSTE of the proposed controller and conventional DSMC controller with 0.2 Hz, 0.5 Hz, 0.8 Hz, and 1.0 Hz of the desired signal frequency in case of no load.

wave signals without load. The sinusoidal signal with amplitude of 20° and frequency from $0.2Hz$ to $1Hz$. In the second scenario, a knee gait pattern is given as a desired trajectory. The proposed controller is evaluated with two different gait cycle (GC) times: 2.5 seconds and 4 seconds. The experimental results of this scenario are shown in Figure 2.15. In both Figure 2.14 and Figure 2.15, the upper sub-figure of each image includes the desired trajectory (dash-back line), measured angle controlled by FFFB controller (green line), measured angle

2.5 Fractional Order Integral Sliding Mode Control Strategy

Table 2.6: MTE and RMSTE of the DFISMC control method, conventional DSMC control method, and FFFB controller in case of no load.

| Signal Frequency | MTE ($^{\circ}$) | | | RMSTE ($^{\circ}$) | | |
|---------------------|--------------------|------|--------|----------------------|------|--------|
| | FFFB | DSMC | DFISMC | FFFB | DSMC | DFISMC |
| 0.2 Hz | 3.34 | 3.14 | 2.65 | 1.35 | 1.03 | 0.98 |
| 0.5 Hz | 3.20 | 6.01 | 5.71 | 1.12 | 1.12 | 1.00 |
| 0.8 Hz | 6.25 | 7.73 | 7.39 | 1.26 | 1.43 | 1.11 |
| 1.0 Hz | 7.17 | 8.68 | 8.67 | 1.62 | 1.63 | 1.43 |
| 4s of GC | 1.78 | 2.40 | 2.31 | 1.50 | 1.30 | 1.04 |
| 2.5s of GC | 1.61 | 4.69 | 2.26 | 1.93 | 1.45 | 1.20 |

controlled by conventional DSMC (red line), and measured angle controller by DFISMC (blue line). The lower part of each figure shows the tracking errors of three controllers. In comparison with the traditional DSMC and FFFB controller, the DFISMC was able to provide a better performance in both transient and steady states. As demonstrated in Figure 2.16, in all scenarios of the experiment, both MTE and RMSTE of the proposed control approach are smaller than the ones of the conventional DSMC control method. For example, when tracking the 1.0 Hz frequency sinusoidal signal, the RMSTE of the DFISMC is 1.43° . These values of DSMC and FFFB controllers are 1.63° and 1.62° , respectively. It means that DFISMC is able to provide a better performance than the conventional DSMC controller and the FFFB controller. In particular, as seen in the error graphs in Figure 2.14 and Figure 2.15, the finite amplitude oscillation of the tracking error in DFISMC is much smaller than in DSMC. It can be concluded that the inherent "*chattering*" phenomenon of SMC control is reduced with DFISMC. The numerical values of the experimental results in all scenarios are given in Table 2.6.

When the antagonistic actuator carries a load $m = 2.5\text{kg}$, the difference among three controllers is not significant in terms of MTE. Particular, the FFFB controller can provide the best startup process. However, the RMSTEs of the DFISMC controller are smallest one, as shown in Figure 2.19. For example, when tracking the 2.5 seconds human-gait trajectory, the RMSTE of the DFISMC is

1.22°, and these values of DSMC and FFFB controllers are 1.68° and 1.81°, respectively. Furthermore, the same conclusion about the "chattering" phenomenon is drawn out in this experiment scenario. Figure 2.17 and Figure 2.18 show the control performances of the system when tracking the sinusoidal signals and human-gait pattern, respectively. All numerical values of MTE and RMSTE in this experimental scenario are also shown in Table 2.7.

From experimental results with multiple scenarios, we can conclude that the DFISM C controller obtains a better tracking performance than the conventional DSMC controller which used the "sign" function of tracking errors. In addition, the implemented disturbance observer and fractional order integral term are able to deal with the finite-amplitude oscillation of sliding mode implementations. As a result, the "chattering" phenomenon is reduced. It also obtain a better tracking performance than the FFFB controller in steady state.

Table 2.7: MTE and RMSTE of the proposed control method, conventional DSMC control method, and FFFB controller with load $m = 2.5\text{kg}$.

| Signal Frequency | MTE (°) | | | RMSTE (°) | | |
|---------------------|---------|-------|---------|-----------|------|---------|
| | FFFB | DSMC | DFISM C | FFFB | DSMC | DFISM C |
| 0.2 Hz | 2.65 | 3.94 | 2.16 | 0.96 | 1.67 | 0.93 |
| 0.5 Hz | 4.97 | 5.11 | 5.39 | 1.52 | 2.31 | 1.47 |
| 0.8 Hz | 6.90 | 8.13 | 7.13 | 1.77 | 2.64 | 1.56 |
| 1.0 Hz | 9.63 | 10.56 | 11.13 | 3.09 | 3.28 | 2.61 |
| 4s of GC | 2.00 | 4.09 | 2.20 | 1.64 | 1.38 | 1.16 |
| 2.5s of GC | 4.95 | 5.23 | 3.41 | 1.81 | 1.68 | 1.22 |

2.6 Conclusions

This chapter focuses on the modeling and control strategies of PAM. Firstly, the literature review of the latest methods for modeling and control of PAM is discussed. After that, the author presents a simple linear model of PAMs in the antagonistic configuration. The chosen model demonstrated a good approximation

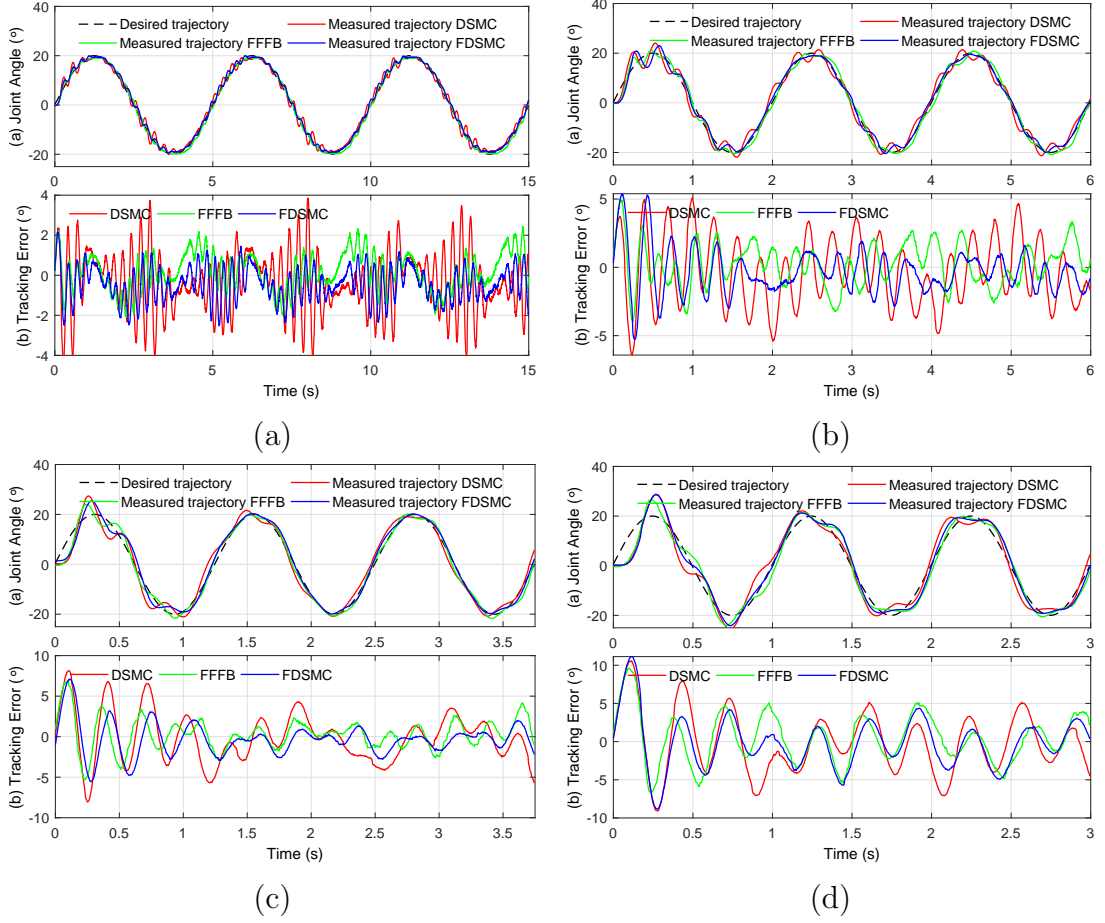


Figure 2.17: Experiment results with 2.5 kg of load for tracking a sinusoidal trajectory: (a) 0.2 Hz, (b) 0.5 Hz, (c) 0.8 Hz, and (d) 1.0 Hz of the desired signal frequency.

of nonlinear characteristics of the actuator: the root mean square errors between estimated and measured values are less than 2.5° . In comparison with the three-elements model [29], hysteresis model [32, 36, 37], and mechanism-based model [43, 48], the identification procedure of the proposed method is simplified. Besides, this procedure does not need to measure the load's acceleration, which is very sensitive to noise.

Base on the built-in model, both linear and nonlinear control strategies are employed for trajectory tracking control of PAM in the antagonistic configuration. In Section 2.4, a modified feedforward-feedback control strategy to handle the tracking control problems of the antagonistic actuator in discrete-time domain. The modified feedforward term which is designed based on the d step ahead

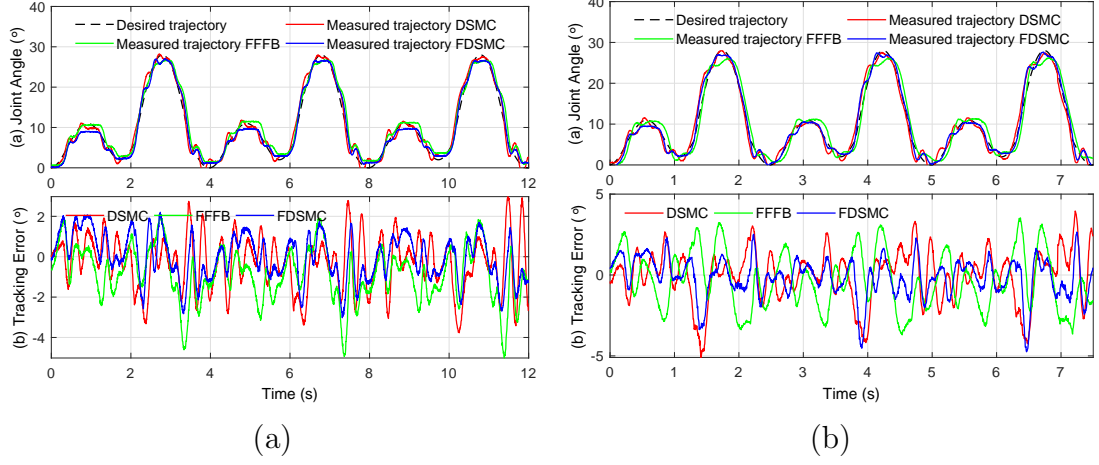


Figure 2.18: Experiment results for the proposed controller and conventional DSMC controller when tracking the human-gait pattern signal with a load $m = 2.5$ kg: (a) 4 seconds and (b) 2.5 seconds of gait cycle time.

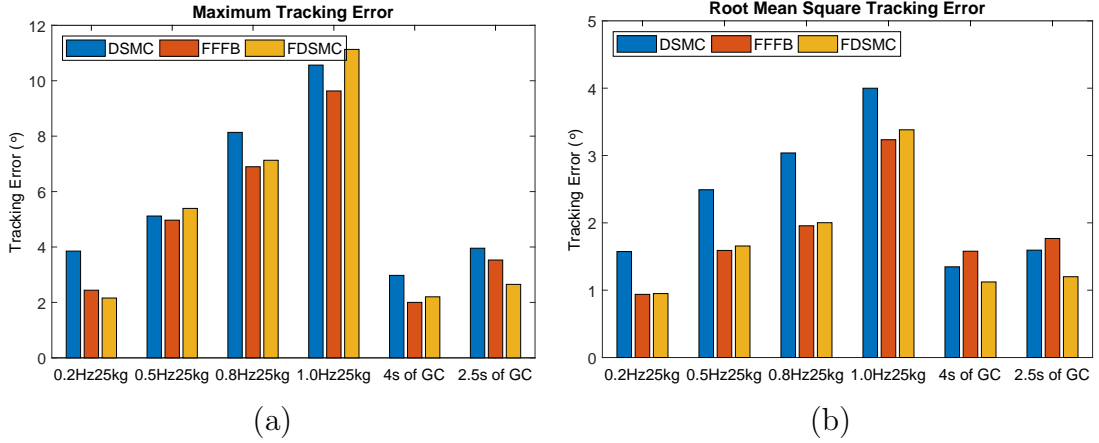


Figure 2.19: MTE and RMSTE of the proposed controller and conventional DSMC controller with 0.2 Hz, 0.5 Hz, 0.8 Hz, and 1.0 Hz of the desired signal frequency and load $m = 2.5$ kg.

value of the reference trajectory is able to improve the tracking performance. In Section 2.5, the DFISMCM controller based on a DSO and the approximated FOI is used to improve the tracking performance. The implementation of DSO and FOI also helps the system reduce the “chattering” phenomenon. Besides, the tracking performance of the DFISMCM also better than the FFFB controller in the steady state of all experiment scenarios. The experimental results illustrate the applicability of the proposed model and controller to a robotic gait training system with a human-gait pattern trackable ability.

Table 2.8 provides the comparison performance of both proposed controllers to the existing control methods in the literature.

However, this chapter focuses only on the trajectory tracking of the antagonistic actuator without considering the dynamic behavior of the overall robot. In the next chapter, the mathematical model of the AIRGAIT orthosis which considers the contribution of bi-articular muscles will be studied. The interaction between hip and knee control loop also must be implemented to the trajectory tracking control system. Future work will also involve the impedance control of the antagonistic actuator to increase the applicability of PAMs in the field of rehabilitation. The impedance of the actuator can be regulated by manipulating the nominal pressure P_0 of two PAMs. To integrate the impedance controller into the system, the relationship between the actuator compliance and nominal pressure P_0 would be considered and modeled in future work.

Table 2.8: The Comparison Results About Modeling and Control of PAMs.

| PAM model | Platform | Control strategy | Control performance | | References |
|---------------------|--------------------|------------------|-----------------------|--------|------------------------------|
| | | | Ampli | Error | |
| Three element model | Single PAM | - | - | - | [29] |
| | Single PAM | SMC and NDO | $\varepsilon = 15\%$ | 0.2 Hz | [30] |
| | Antagonistic | BASMC | $\theta = 60^\circ$ | 3.0 Hz | [12, 35] |
| | Overall robot | Modified SMC | $\theta = 50^\circ$ | 0.6m/s | [9, 22, 23] |
| | Overall robot | CRCV | $\theta = 50^\circ$ | 0.6m/s | [24] |
| Hysteresis model | Maxwell-slip | Cascade PID | $\varepsilon = 05\%$ | 0.2Hz | [32, 38, 39] |
| | Prandtl Ishlinskii | Cascade PID | $\varepsilon = 20\%$ | 0.1Hz | [36] |
| | Preisach | Cascade PID | $\varepsilon = 8\%$ | 0.2Hz | 7.9×10^{-3} mm [37] |
| Grey-box model | Single PAM | SMC | $\varepsilon = 5.6\%$ | 0.1Hz | [31] |
| | Single PAM | IIN controller | $\varepsilon = 5.6\%$ | 1.5Hz | [40] |
| Linearized model | Single PAM | ANN-PID | $\theta = 80^\circ$ | 0.25Hz | [33, 53] |
| | Antagonistic | Modified SMC | $\theta = 10^\circ$ | 0.5Hz | [43]-[49] |
| Discrete-time SOPDT | Antagonistic | FFFB | $\theta = 20^\circ$ | 1.0Hz | 9.63° |
| | Antagonistic | DFISMC | $\theta = 20^\circ$ | 1.0Hz | 11.13° |

Abbreviations:

SMC: Sliding mode control

NDO: Nonlinear disturbance observer

IMC: Internal model control

IIN: Integrated intelligent nonlinear control

BASMC: Boundary layer augmented sliding mode control.

CRCV: Robust Variable structure Controller

ANN: Adaptive neural network

FFFB: Feedforward feedback

DFISMC: Discrete-time fractional integral SMC.

Chapter 3

Trajectory Tracking Control of the AIRGAIT Orthosis

3.1 Introduction

Rehabilitation robot is designed to support patients with movement disability caused by neurological pathologies such as spinal cord injury (SCI), stroke, or traumatic brain injuries, during the training process. This type of robot may help the patient improve their recovery by supporting them to perform repetitive, systematic training sessions. In the early stage, the exoskeleton robot leads the patient's limbs passively to a predefined gait trajectory of rehabilitation therapy. Since one of the most important requirements for the gait training robotic orthosis is having high stiffness enough to provide the assistive force when the subject's limbs deviate from the designated trajectory.

Most of the existing rehabilitation systems [3, 5, 8, 9, 10, 15, 27, 58, 59] are implemented by the trajectory tracking controller. The AIRGAIT robotic orthosis also is integrated the trajectory tracking function by implementing the co-contraction control strategy [20] and computed torque controller [21]. Nevertheless, the system is able to track the low speed of reference trajectory with these types of control approach. Besides, these types of control system were developed without considering the contribution of the bi-articular muscles. In this chapter, the AIRGAIT system will be implemented the modified computed torque control strategy for improving the tracking performance. The effectiveness of the proposed control strategy is verified by the experiments with the participation of various subjects.

3.2 Contributions

This chapter presents the development of a modified computed torque controller for the trajectory tracking purpose of the AIRGAIT robotic orthosis. First, the mechanism of overall robot exoskeleton is evaluated in high compliance mode. Secondly, the dynamic behavior of the robot exoskeleton which considers the contribution of the bi-articular muscles will be built. After that, the modified computed torque control strategy which employs the fractional order calculus is investigated to improve the tracking performance. Finally, the closed-loop system stability analysis is conducted by using the Lyapunov direct method.

3.3 Mechanism Evaluation of the Robotic Orthosis

Table 3.1: The information of five subjects participating the mechanism evaluation experiment.

| Information | Value (Mean \pm SD) |
|-------------------|-----------------------|
| Age (Years) | 21.4 \pm 0.5 |
| Body weight (kg) | 59.7 \pm 3.2 |
| Height (cm) | 171.5 \pm 6.0 |
| Femur length (cm) | 51.2 \pm 2.6 |

The mechanism of the robotic orthosis must be designed to ensure the safety and comfort of the patient during training. In order to evaluate the mechanism of the AIRGAIT robotic orthosis, five healthy male subjects are asked to participate in the experiment. Table 3.1 provides detail information about the lower-limb of the subjects.

The subjects wear the orthosis which is set up at low stiffness and walk on the treadmill. The hip and knee joint angle trajectories of the orthosis are measured and recorded by the potentiometer. The angle trajectories of the hip and knee joint of the subject are recorded by K100 Amplifier Base Unit from Biometrics Ltd company with 1000Hz sampling frequency. In experiments, the subjects walk

3.3 Mechanism Evaluation of the Robotic Orthosis

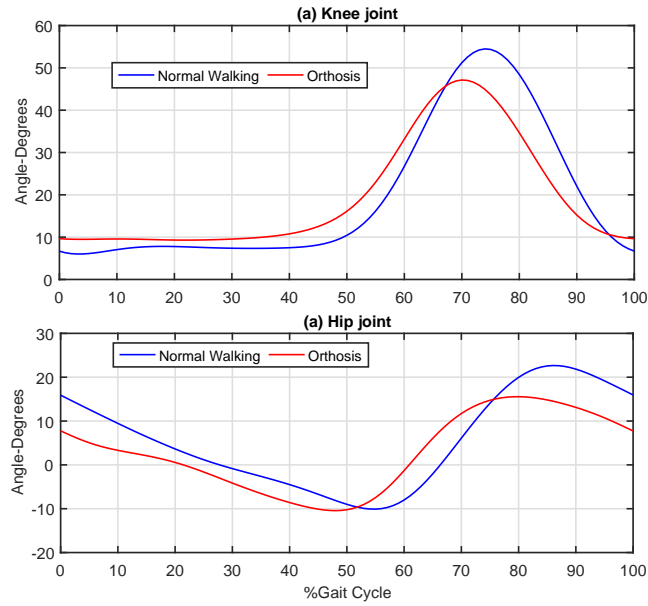


Figure 3.1: The average value of angle trajectory of orthosis joint compared to subject normal walking in one gait cycle.

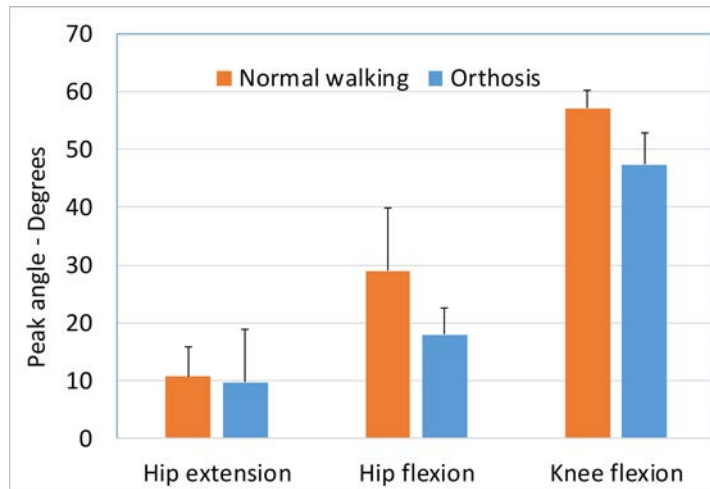


Figure 3.2: The peak value of orthosis angle compared to normal walking.

in 2 minutes to familiar with the experiment condition first and then the data is recorded for 1 minute for further analysis. The treadmill speed is set at 2.5 km/h for all experiments. This speed is the normal walking speed of a healthy subject. The BWS is not used in this mode because the subjects are healthy and do not need any support. The average value of the hip and knee joint angle trajectory in one gait cycle (GC) is given in Fig.3.1 where the blue line is the joint angle trajectory of the subject in normal walking condition and the red line is the

3.4 Modeling of the 2-DOF Robot Manipulated by Bi-articular Muscles

data collected from the angle sensor. As shown in Fig.3.2, the peak value of the robotic orthosis hip and knee joint in extension and flexion states are not much difference in comparison with the normal walking of a subject. This experiment results show that the angle trajectory of the AIRGAIT orthosis is similar to the human walking trajectory. Hence, the subject can feel comfortable while wearing the orthosis during training.

3.4 Modeling of the 2-DOF Robot Manipulated by Bi-articular Muscles

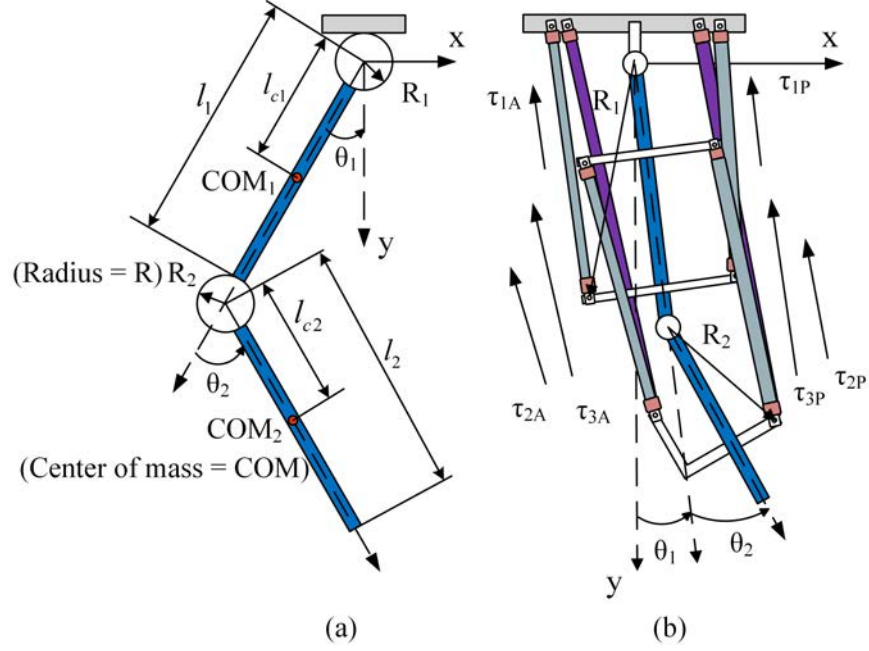


Figure 3.3: (a) Typical 2DOF robotic (b) Robotic Orthosis with two mono-articular and one bi-articular muscles. The 1, 2, 3 subscripts represent hip, knee and bi-articular muscle. A and P subscripts denote the anterior and posterior PAMs.

The general configuration of a two degree of freedom (2DOF) is shown in Fig. 3.3a where θ_i , l_i and l_{ci} are joint angles, length of links and the distance from joints to the corresponding center of mass (COM), respectively. These parameters of the AIRGAIT robotic orthosis are given in Table 3.2 in details. The dynamics

3.4 Modeling of the 2-DOF Robot Manipulated by Bi-articular Muscles

Table 3.2: Parameters of the AIRGAIT Robotic Orthosis.

| Parameters | Value |
|---------------------------|-------|
| m_1 [kg] | 1.34 |
| m_2 [kg] | 0.97 |
| I_1 [kgm ²] | 0.052 |
| I_2 [kgm ²] | 0.032 |
| L_1 [m] | 0.4 |
| L_{c1} [m] | 0.2 |
| L_2 [m] | 0.35 |
| L_{c2} [m] | 0.15 |

of 2DOF robotic is described by the following Euler-Lagrange equation

$$D(\theta)\ddot{\theta} + C(\theta, \dot{\theta})\dot{\theta} + G(\theta) = T \quad (3.1)$$

where $T = [T_1, T_2]^T$ and $\theta = [\theta_1 \ \theta_2]^T$ are the vector of applied torques and joint angles, respectively. The system mass $D(\theta)$, the coriolis matrix $C(\theta, \dot{\theta})$ and the vector of gravity $G(\theta)$ are

$$D(\theta) = \begin{bmatrix} D_{11} & D_{12} \\ D_{21} & D_{22} \end{bmatrix} \quad (3.2)$$

$$C(\theta, \dot{\theta}) = \begin{bmatrix} C_{11} & C_{12} \\ C_{21} & C_{22} \end{bmatrix} \quad (3.3)$$

$$G(\theta) = [G_1 \ G_2]^T \quad (3.4)$$

with

$$D_{11} = m_1 l_{c1}^2 + m_2 (l_1^2 + l_{c2}^2 + 2l_1 l_{c2} \cos\theta_2) + I_1 + I_2 \quad (3.5a)$$

$$D_{12} = D_{21} = m_2 (l_{c2}^2 + l_1 l_{c2} \cos\theta_2) \quad (3.5b)$$

$$D_{22} = m_2 l_{c2}^2 + I_2 \quad (3.5c)$$

$$C_{11} = -m_2 l_1 l_{c2} \sin\theta_2 \dot{\theta}_2 \quad (3.6a)$$

$$C_{12} = -m_2 l_1 l_{c2} \sin\theta_2 (\dot{\theta}_1 + \dot{\theta}_2) \quad (3.6b)$$

$$C_{21} = m_2 l_1 l_{c2} \sin\theta_2 \dot{\theta}_1 \quad (3.6c)$$

$$C_{22} = 0 \quad (3.6d)$$

$$G_1 = (m_1 l_{c1} + m_2 l_1) g \cos \theta_1 + m_2 l_{c2} g \cos(\theta_1 + \theta_2) \quad (3.7a)$$

$$G_2 = m_2 l_{c2} g \cos(\theta_1 + \theta_2) \quad (3.7b)$$

As seen in Fig. 3.3b, in the AIRGAIT orthosis configuration, the hip and knee joints are actuated by two mono-articular muscles, whereas the bi-articular which connects between the hip and knee joints has an influence on both joints simultaneously. Hence, the relation between the torques τ_1 , τ_2 and τ_3 generated by the corresponding pair of PAMs and the joints torques can be described by

$$T = W\tau \quad (3.8)$$

where

$$\tau = [\tau_1 \quad \tau_2 \quad \tau_3]^T \quad (3.9)$$

and $W \in \mathbb{R}^{2 \times 3}$ is the transformation from the muscle to joint space:

$$W = \begin{bmatrix} 1 & 0 & 1 \\ 0 & 1 & 1 \end{bmatrix} \quad (3.10)$$

Since W is not a square matrix, τ can be derived from (3.8) and (3.10) by using the Moore-Penrose pseudo-inverse matrix W^+ [60] of W as

$$\tau = W^+ T \quad (3.11)$$

From (3.1) and (3.11), the dynamic model of the lower-limb robotic orthosis considering the additional bi-articular muscle can be expressed by the following equation

$$\tau = \bar{D}(\theta)\ddot{\theta} + \bar{C}(\theta)\dot{\theta} + \bar{G}(\theta) \quad (3.12)$$

where $\bar{D}(\theta) = W^+ D(\theta)$, $\bar{C}(\theta) = W^+ C(\theta)$, and $\bar{G}(\theta) = W^+ G(\theta)$, respectively.

3.5 Trajectory Tracking Control Design

3.5.1 Computed Torque Control Strategy

The dynamic model 3.12 that characterizes the behavior of the AIRGAIT robotic orthosis manipulated by additional bi-articular muscles. This model might lead

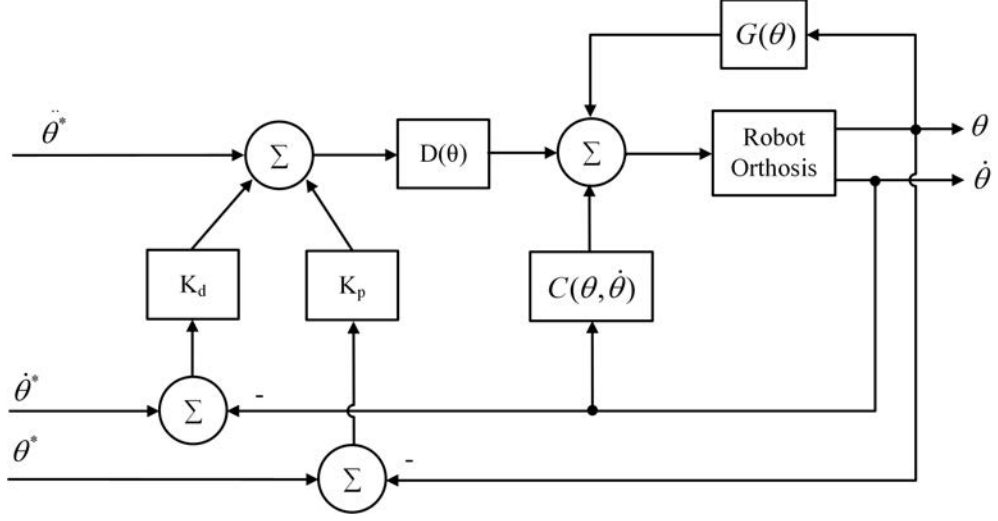


Figure 3.4: Block diagram of the computed torque control strategy.

us to believe that the needed muscle torques to guide the subject's limbs to designate motion can be obtained from the desired, measured trajectories together its velocities. This controller named computed torque control.

The computed torque control law is given by

$$\tau = D(\theta) \left[\ddot{\theta}^* + K_d \dot{e} + K_p e \right] + C(\theta, \dot{\theta}) \dot{\theta} + G(\theta) \quad (3.13)$$

In (3.13), θ^* is the reference trajectory, $e = \theta^* - \theta$ is the tracking error, K_p and K_d are symmetric positive definite gain matrices. Notice that, the controller (3.13) contains the terms $K_d \dot{e} + K_p e$ are the PD type. However, the others term $D(\theta)$, $C(\theta, \dot{\theta}) \dot{\theta}$, $G(\theta)$ are not constant, since this controller is not a linear one as the PD. Beside, this controller depends on only the position error e , this can be clearly explained when rearranging the computed torque control law as

$$\tau = D(\theta^* - e) \left[\ddot{\theta}^* + K_d \dot{e} + K_p e \right] + C(\theta^* - e, \dot{\theta}^* - \dot{e}) \dot{\theta} + G(\theta^* - e) \quad (3.14)$$

The block diagram which represented the computed torque control strategy of the AIRGAIT orthosis is demonstrated in Fig. 3.4. The closed loop equation of the system can be obtained by substituting the control action (3.13) to the robot model (3.12) as

$$D(\theta) \ddot{\theta} = D(\theta) \left[\ddot{\theta}^* + K_d \dot{e} + K_p e \right] \quad (3.15)$$

Since $D(\theta)$ is a positive definite matrix and it also invertible, the equation (3.15) is reduced to

$$\ddot{e} + K_d \dot{e} + K_p e = 0 \quad (3.16)$$

which in turn, may be expressed in terms of the state vector $[e^T \ \dot{e}^T]^T$ as

$$\begin{aligned} \frac{d}{dt} \begin{bmatrix} e \\ \dot{e} \end{bmatrix} &= \begin{bmatrix} \dot{e} \\ -K_p e - K_d \dot{e} \end{bmatrix} \\ &= \begin{bmatrix} 0 & I \\ -K_p & -K_d \end{bmatrix} \begin{bmatrix} e \\ \dot{e} \end{bmatrix} \end{aligned} \quad (3.17)$$

It is important to remark that the closed-loop (3.17) of the system is represented by a linear differential equation which unique equilibrium point is given by $[e^T \ \dot{e}^T]^T = 0 \in \mathbb{R}^{2n}$. The unicity of the equilibrium follows from the fact that the matrix K_p is positive definite and nonsingular.

3.5.2 Modified Computed Torque Control Strategy

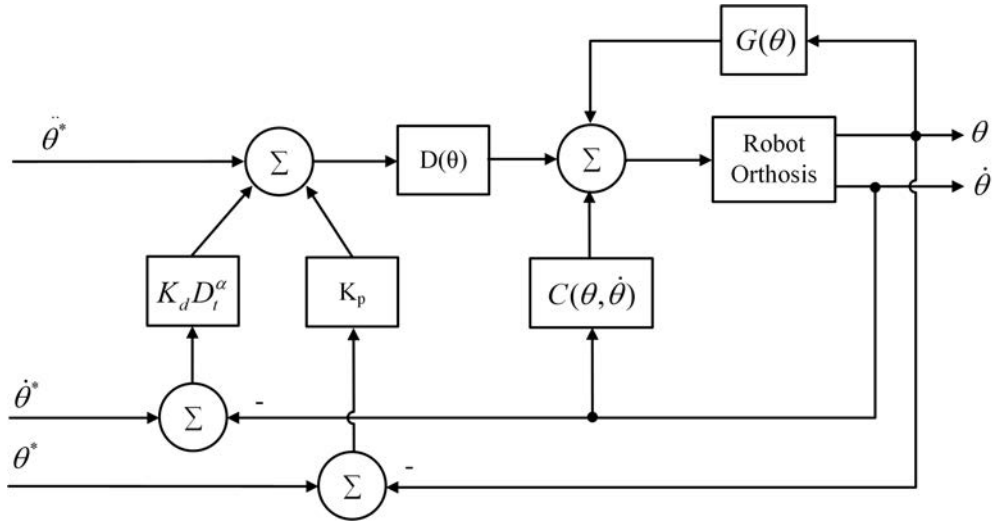


Figure 3.5: Block diagram of the modified computed torque control strategy.

In this section, a modified computed torque controller is proposed to enhance the tracking performance of the robotic orthosis, in which the conventional integer order derivative is replaced by a fractional order one.

$$\tau = \bar{D}(\theta) \left[\ddot{\theta}^* + K_d D_t^\alpha e + K_p e \right] + \bar{C}(\theta, \dot{\theta}) \dot{\theta} + \bar{G}(\theta) \quad (3.18)$$

In (3.18), θ^* is the reference trajectory, $e = \theta^* - \theta$ is the tracking error, K_p and K_d are positive definite gain matrices. $D_t^\alpha e$ is the differential of fractional order $\alpha \in (0, 1)$ of e .

By substituting (3.18) into (3.12), the dynamics of tracking error is

$$\bar{D}(\theta)(\ddot{e} + K_d D_t^\alpha e + K_p e) = 0 \quad (3.19)$$

Since $\bar{D}(\theta)$ is positive definite, the dynamics of the tracking error actually only depends on

$$\ddot{e} + K_d D_t^\alpha e + K_p e = 0 \quad (3.20)$$

By adjusting K_d , K_p and the additional fractional order α , the required tracking performance can be achieved. Moreover, the control law (3.18) can be rewritten as

$$\tau = \underbrace{\bar{D}(\theta)\ddot{\theta}^* + \bar{C}(\theta, \dot{\theta})\dot{\theta} + \bar{G}(\theta)}_{\tau_{ff}} + \underbrace{\bar{D}(\theta)(K_d D_t^\alpha e + K_p e)}_{\tau_{fb}} \quad (3.21)$$

It can be seen from (3.21) that the configuration of the controller is combined

Table 3.3: The Parameters of the Proposed Controller.

| Controller channel | K_p | K_d | α |
|---------------------|-------|--------|----------|
| Knee mono-articular | 0.05 | 0.8e-3 | 0.8 |
| Hip mono-articular | 0.05 | 0.5e-3 | 0.9 |
| Bi-articular | 0.04 | 1.0e-3 | 0.85 |

of two terms including a feedforward (τ_{ff}) and a feedback (τ_{fb}). For practical purpose, the design matrices K_d and K_p may be chosen diagonal. This means that equation (3.21) represents a decoupled multi-variable linear system. Hence, the control system actually consists of three channels for hip, knee and bi-articular actuators which are independent of each other. Figure 3.5 demonstrate the control scheme of the modified computed torque controller of which the parameters after being well tuned are provided in Table. 3.3.

3.5.3 Stability Analysis

The following content is related to the stability analysis of the AIRGAI closed loop system by using Lyapunov's direct methods. The main objective in Lyapunov stability theory is to study the behavior of dynamical systems described by ordinary differential equations of the form

$$\dot{x} = f(t, x), \quad x \in \mathbb{R}^n, \quad t \in \mathbb{R}_+ \quad (3.22)$$

where the vector x corresponds to the state of the system represented by (3.22). If the function f does not depend explicitly on time, the system is autonomous and the equation (3.22) becomes

$$\dot{x} = f(x), \quad x \in \mathbb{R}^n \quad (3.23)$$

Firstly, we present the basic concepts in Lyapunov theory i.e. equilibrium, stability, asymptotic stability, etc. which mentioned in many textbooks.

3.5.3.1 Definitions of Stability

Definition 3.1 *Equilibrium*

A constant vector $x_e \in \mathbb{R}^n$ is an equilibrium or equilibrium state of the system (3.22) if

$$f(t, x_e) = 0 \quad \forall t \geq 0 \quad (3.24)$$

Definition 3.2 *Stability*

The origin is a stable equilibrium of equation (3.22) if, for each pair of numbers $\varepsilon > 0$ and $t_0 \geq 0$, there exists $\delta = \delta(t_0, \varepsilon) > 0$ such that

$$\|x(t_0)\| < \delta \Rightarrow \|x(t)\| < \varepsilon \quad \forall t \geq t_0 \geq 0 \quad (3.25)$$

Correspondingly, the origin of equation (3.23) is said to be stable if for each $\varepsilon > 0$ there exists $\delta = \delta(\varepsilon) > 0$ such that (3.25) holds with $t_0 = 0$.

Definition 3.3 *Uniform stability*

The origin is a uniformly stable equilibrium of equation (3.22) if for each number $\varepsilon > 0$ there exists $\delta = \delta(\varepsilon) > 0$ such that (3.25) holds.

Definition 3.4 *Global uniform asymptotic stability*

The origin is a globally uniformly asymptotically stable equilibrium of equation (3.22) if:

1. the origin is uniformly stable with $\delta(\varepsilon)$ in Definition (3.25) which satisfies $\delta(\varepsilon) \rightarrow \infty$ as $\varepsilon \rightarrow \infty$ (uniform boundedness) and
2. the origin is globally uniformly attractive, i.e. for all $x(t_0) \in \mathbb{R}^n$ and all $t_0 \geq 0$,

$$\|x(t)\| \rightarrow 0 \text{ as } t \rightarrow \infty \tag{3.26}$$

with a convergence rate that is independent of t_0

3.5.3.2 Lyapunov Functions

Definition 3.5 *Lyapunov function candidate*

A continuous and differentiable function $V: \mathbb{R}_+ \times \mathbb{R}^n \rightarrow \mathbb{R}_+$ is said to be a Lyapunov function candidate for the equilibrium $x = 0 \in \mathbb{R}^n$ of the equation (3.22) if:

1. $V(t, x)$ is locally positive definite;
2. $\frac{\partial V(t, x)}{\partial t}$ is continuous with respect to t and x ;
3. $\frac{\partial V(t, x)}{\partial x}$ is continuous with respect to t and x ;

Definition 3.6 *Lyapunov function*

A Lyapunov function candidate $V(t, x)$ for equation (3.22) is a Lyapunov function for (3.22) if its total time derivative along the trajectories of (3.22) satisfies

$$\dot{V}(t, x) \leq 0, \quad t \geq 0 \text{ and for small } \|x\|. \tag{3.27}$$

Correspondingly, a Lyapunov function candidate $V(x)$ for equation (3.23) is a Lyapunov function $\dot{V}(t, x) \leq 0$ and for small $\|x\|$.

3.5.3.3 Lyapunov's Direct Method

Theorem 3.1 *Stability and uniform stability*

The origin is a stable equilibrium of (3.22), if there exists a Lyapunov function candidate $V(t, x)$ (i.e. a locally positive definite function with continuous partial derivatives with respect to t and x) such that its total time derivative satisfies

$$\dot{V}(t, x) \leq 0, \quad \forall t \geq 0 \quad \text{for small } \|x\| \quad (3.28)$$

If moreover $V(t, x)$ is decrescent for small $\|x\|$ then the origin is uniformly stable.

Theorem 3.2 *Global (uniform) asymptotic stability*

The origin of (3.22) (respectively of 3.23) is globally asymptotically stable if there exists a radially unbounded, globally positive definite Lyapunov function candidate $V(t, x)$ (respectively $V(x)$) such that its time derivative is globally negative definite. If, moreover, the function $V(t, x)$ is decrescent, then the origin is globally uniformly asymptotically stable.

3.5.3.4 Stability Analysis of the Closed Loop System

We can see that, the closed-loop equation of the AIRGAIT system (3.17) can be rewrite as the (3.23) with the state vector $x = [e^T \quad \dot{e}^T]^T$. In general assumption, the constant ε satisfying $\lambda_{\min} \{K_v\} > \varepsilon > 0$ for some $\lambda_{\min} \{K_v\}$. Multiplying by $x^T x$ where $x \in \mathbb{R}^n$ is any nonzero vector, we obtain $\lambda_{\min} \{K_v\} x^T x > \varepsilon x^T x$. Since, K_v is designed as a symmetric matrix then $x^T K_v x \geq \lambda_{\min} \{K_v\} x^T x$ and therefore,

$$x^T [K_v - \varepsilon I] x > 0 \quad \forall x \neq 0 \in \mathbb{R}^n. \quad (3.29)$$

This means that the matrix $[K_v - \varepsilon I]$ is positive definite. Considering all this, the positivity of the matrix K_p and the constant ε we conclude that

$$K_p + \varepsilon K_v - \varepsilon^2 I > 0 \quad (3.30)$$

Consider the Lyapunov function candidate

$$\begin{aligned} V(e, \dot{e}) &= \frac{1}{2} \begin{bmatrix} e \\ \dot{e} \end{bmatrix}^T \begin{bmatrix} K_p + \varepsilon K_v & \varepsilon I \\ \varepsilon I & I \end{bmatrix} \begin{bmatrix} e \\ \dot{e} \end{bmatrix} \\ &= \frac{1}{2} [\dot{e} + \varepsilon e]^T [\dot{e} + \varepsilon e] + \frac{1}{2} e^T [K_p + \varepsilon K_v - \varepsilon^2 I] e \end{aligned} \quad (3.31)$$

where the constant ε satisfies (3.30). From this, the function (3.31) is global positive definite. For more clear, the equation (3.31) is rewritten as

$$V(e, \dot{e}) = \frac{1}{2}\dot{e}^T \dot{e} + \frac{1}{2}e^T [K_p + \varepsilon K_v]e + \varepsilon e^T \dot{e} \quad (3.32)$$

Evaluating the total time derivative of $V(e, \dot{e})$ we get

$$\dot{V}(e, \dot{e}) = \ddot{e}^T \dot{e} + e^T [K_p + \varepsilon K_v] \dot{e} + \varepsilon \dot{e}^T \dot{e} + \varepsilon e^T \ddot{e} \quad (3.33)$$

Substituting \ddot{e} from the closed-loop equation (3.17) and making some simplifications we obtain

$$\begin{aligned} \dot{V}(e, \dot{e}) &= -\dot{e}^T [K_v - \varepsilon I] \dot{e} - \varepsilon e^T K_p e \\ &= \begin{bmatrix} e \\ \dot{e} \end{bmatrix}^T \begin{bmatrix} \varepsilon K_p & 0 \\ 0 & K_v - \varepsilon I \end{bmatrix} \begin{bmatrix} e \\ \dot{e} \end{bmatrix} \end{aligned} \quad (3.34)$$

Since ε is chosen so that $K_v - \varepsilon I > 0$, and K_p is positive definite, the function $\dot{V}(e, \dot{e})$ in (3.34) is global negative definite.

According to the theorem (3.2) (Global uniform asymptotic stability), we conclude that the origin $\begin{bmatrix} e \\ \dot{e} \end{bmatrix}^T = 0 \in \mathbb{R}^{2n}$ of the AIRGAIT system closed-loop equation is global uniformly stable and therefore

$$\begin{aligned} \lim_{t \rightarrow \infty} \dot{e}(t) &= 0 \\ \lim_{t \rightarrow \infty} e(t) &= 0 \end{aligned} \quad (3.35)$$

from which it follows that the trajectory tracking purpose is achieved.

3.6 Experimental Evaluation

3.6.1 Experimental Setup

Eight healthy male subjects, age (29.7 ± 3.9 [years])(mean (M) \pm standard deviation (SD)), height (166 ± 3.6 [cm]), weight (62.4 ± 8.1 [kg]) with no known neurological disorders participate in the experiment. The subjects are asked to wear the orthosis and allow it guide to the designated trajectory for 10 minutes. The treadmill speed is set at 2.2 [km/h]. All subjects gave their written informed consents before they participated in the experiments. The experimental

procedures involving human subject described in this paper were approved by the Ethics Committee of Shibaura Institute of Technology.

During the experiments, the desired trajectory of the hip $\theta_{1,t}^*$ and knee $\theta_{2,t}^*$ mono-articular actuator are modified from the gait data provided in textbook [52]. Particularly, the reference trajectory for the third channel, which shows the contribution of the antagonistic bi-articular muscles to the motion of the robot, is the sum of the hip and knee reference values $\theta_{3,t}^* = \theta_{1,t}^* + \theta_{2,t}^*$. The sampling frequency for the overall system is set at 100 [Hz]. The data from the load cells, pressure sensors, as well as the data of the angle sensor are processed by 6 [Hz] low pass filter. All analyses are carried out by MATLAB (MathWorks, Natick, MA, USA) software version R2016a.

3.6.2 Experimental Protocol

The experiment procedure for verifying the proposed controller consists of three following steps:

Step 1:

Each subject was asked to wear the robotic exoskeleton and the hardness of the BWS system. The support level is set at 100% of the subject weight to pick the subject up from the treadmill. The robotic exoskeleton is operated in trajectory tracking mode. After 1 minute, the system reaches steady state and the subject familiar with the experiment condition.

Step 2:

The operator runs the treadmill and accelerates to the speed which synchronizes to the orthosis speed. After that, the support level is slowly decreased from 100 % to 0%. The total time of this step is about 5 minutes. For all subjects, the data of the robot joints angle trajectories are recorded in 25 gait cycles (GCs) equivalent to 1 minute for assessing.

Step 3:

The operator raises the support level of BWS from 0% to 100% to pick the subject up from the treadmill again. After that, both robotic exoskeleton and treadmill are shut down. The experiment is complete.

3.6.3 Experimental Results

In order to evaluate the performance of the proposed control strategy during the startup process, the data of the desired and measured trajectories are collected and compare with the normal computed torque approach which using Proportional Derivative (PD) controller. As shown in Fig. 3.6 the proposed controller

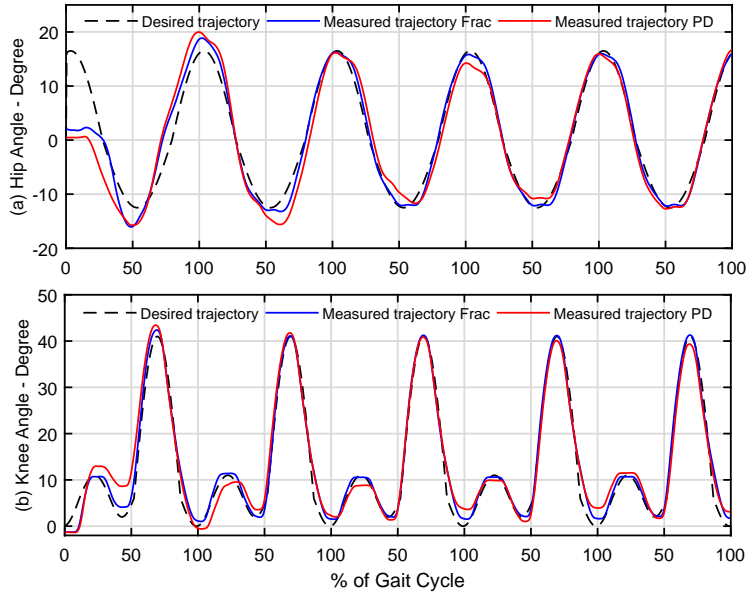


Figure 3.6: The hip and knee joint angle trajectories of the proposed controller and normal computed torque one during the startup process: (a) Hip joint (b) Knee joint.

is able to provide a better startup process than the normal computed torque controller. With the proposed control method, the system reaches the steady state in the time of 2 GCs and the root mean square tracking errors (RMSTEs) are 2.96^0 and 1.89^0 for hip and knee joints, respectively. With the conventional computed torque controller, these values are 3.94^0 and 2.78^0 , besides the system achieves the steady state in 5 GCs. This comparison is executed without the participation of a subject. The RMSTE is computed by

$$RMSTE = \sqrt{\frac{1}{N} \sum_{k=0}^N e_k^2} \quad (3.36)$$

in which N is the total number of sampled data. To evaluate the performance of the system during the steady state of the trajectory tracking mode the maximum

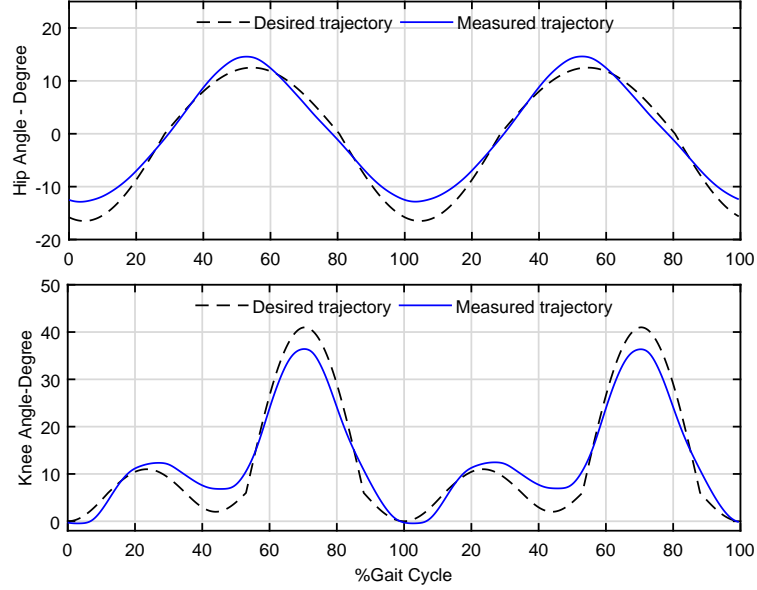


Figure 3.7: The trajectory tracking performance of the proposed controller, the hip and knee trajectories are averaged over all subjects for two gait cycles.

tracking error (MTE) and RMSTE between the desired and measured trajectories are assessed. Besides, for studying the inter subject variability, standard deviation over these different values of all subjects are also considered. Fig. 3.7 illustrates the desired and measured trajectory of robot joint angles of the proposed controller and normal computed torque control strategy. The trajectories are averaged over all subjects and shown for two GCs. As given in Table 3.4, the MTE and RMSTE are below $5.85^0 \pm 0.56$ and $4.25^0 \pm 1.01$ for both hip and knee joints. These results are acceptable for the rehabilitation system in practice. Not to much standard deviation values between the trajectory MTE and RMSTE show that the control system is robust with the variability of the subjects and is able to guide different types of patient in the rehabilitation process. Besides, from the Table 3.4 we also can conclude that the proposed control method is able to provide a better performance than the previous versions of the AIRGAIT system in [19, 20, 21] which is only operated at low speed (0.8 km/h) or without a subject. It is also comparable to the 6-DOF system [9, 22, 23, 24, 25] in which the MTEs are about 4° and 9° for the hip and knee joint, respectively. Both systems are operated under similar treadmill speed which is about 0.6m/s. This result is also in accordance with the commercial gait training system LOKOMAT [26], in which the MTE is 15° . Table 3.5 shows the comparison results of the proposed

Table 3.4: Absolute Values of Maximum Tracking Error, Root Mean Square Tracking Error Averaged over All subjects in Two Gait Cycles.

| Gait Parameter | Value (Mean \pm SD) | |
|-------------------------|-----------------------|------------------|
| | Proposed system | 6-DOF system[23] |
| MTE_{hip} (degree) | 4.25 ± 1.01 | 3.96 ± 1.08 |
| $RMSTE_{hip}$ (degree) | 2.09 ± 0.14 | - |
| MTE_{knee} (degree) | 5.85 ± 0.56 | 9.31 ± 1.60 |
| $RMSTE_{knee}$ (degree) | 3.09 ± 0.70 | - |

controller to the existing systems in the literature.

3.7 Conclusions

In this chapter, we continue improving the control system for the AIRGAIT lower limb robotic orthosis. First, the dynamic behavior of the robot is modeled with the contribution of the bi-articular muscle. Then, based on the built-in model, the modified computed torque control approach which employs a fractional order derivative is proposed to improve the tracking performance. Experiments with the participation of various subjects are conducted to verify the effectiveness of the proposed control method. In comparison with normal computed torque strategy, the proposed controller provides a better performance not only in the steady state but also during the transient process. The results show that the system is much improved in comparison with its previous version in both speed and tracking error of the system. It is also comparable to the existing PAM-based systems in literature [9, 22, 23, 24, 25].

The overall system with the proposed control strategy is applied and evaluated with only healthy subjects in trajectory tracking mode. In order to provide the therapeutic efficacy to the neurological impaired patients, the impedance of the robot orthosis must be considered to encourage the volunteer of the patients during training. More safety condition and clinical evaluations also must be considered and implemented to the system in next chapters.

Table 3.5: The Comparison Results of the AIRGAIT System to the Existing Systems.

| Prototype | Covered joints | Configuration | Control system | Performance | References |
|--------------|----------------|------------------|--------------------------|---|---------------------|
| Hip Orthosis | Hip | single PAM | Position control | - | [3] |
| RGT | Ankle | 2 single PAMs | Position control | - | [10] |
| AFO | Ankle | Mono-articular | Proportional control | - | [5] |
| PLLO | All leg | Mono-articular | PID | - | [6] |
| WGTO | All leg | Mono-articular | - | - | [16] |
| KAFO | Knee & Ankle | Mono-articular | Torque control | - | [8] |
| KNEXO | Knee & Ankle | Mono-articular | PID & Feedforward | 0.7m/s | [11] |
| AIRGAIT | Hip & Knee | Bi-articular | PID & computed torque | - | [19, 20, 21] |
| 6-DOF robot | All leg | Mono-articular | Modified SMC | $\theta = 50^\circ, e = 9.31^\circ,$ 0.6m/s | [9, 22, 23, 24, 25] |
| LOKOMAT | All leg | Motorized system | - | $\theta \geq 60^\circ, e = 15^\circ,$ 2.0km/h | [26] |
| AIRGAIT | Hip and Knee | Bi-articular | Modified Computed Torque | $\theta \geq 40^\circ, e = 7^\circ,$ 2.2km/h | [61] |

Abbreviations:

PID: Proportional Integral Derivative

SMC: Sliding mode control

Chapter 4

Impedance Control of the AIRGAIT Orthosis

4.1 Introduction

In trajectory tracking mode, a rehabilitation robot interacts with patients in a “master-slave” relationship, it means the robot force the patients to follow a pre-defined motion without consideration of active voluntary efforts of the patient. In that traditional position control mode, the human subject usual remains passive and the robot ignores the active contribution of the subject. Furthermore, the robot does not systematically allow for deviation from the predefined movement pattern. However, the execution and repetition of the inflexible pattern are not optimal for training. In contrast, variability and the possibility to make errors are considered as essential components of practice for locomotor training. A recent study by Lewek *et al.* [62] reported that manual training with therapist assistance resulted in significant improvements in the consistency of intralimb movements of the impaired limb, which enabled kinematic variability, but was not improved by position-controlled Lokomat training, which reduced kinematic variability to a minimum. Another report also conducts to a similar conclusion, all indicating that more freedom and more active participation during the movement lead to a better outcome after the training [63, 64, 65]. Thus, for more effective training, rehabilitation robot it should be ensured,

- (i) the robot assists only as needed so that the patient can contribute to the movement with own voluntary effort, and

- (ii) that the limb movement deviates from a given and repetitive trajectory. We call this kind of robotic behavior “patient cooperative” or ”assist-as-needed”.

It is expected that patient-cooperative training strategies will stimulate active participation by the patient. They have also the potential to increase the motivation of the patient because changes in muscle activation will be reflected in the walking pattern, causing consistently a feeling of success. It is assumed that patient cooperative strategies will maximize the therapeutic outcome. Intensive clinical studies with large patient populations have still to be carried out to prove these hypotheses.

Assist-as-needed training strategies are developed by regulating robot impedance. It means that the control system is able to “recognize” the patient’s disability level and adapt the robotic assistance to the patient’s contribution, thus, giving the patient more movement freedom and variability than during position control. The patient’s effort can be estimated by measuring the human-robot interaction force or by monitoring muscular efforts via EMG sensors. In this chapter, we are going to integrate the assist-as-needed training strategy for the AIRGAIT rehabilitation system by implementing an impedance controller.

4.2 Contributions

In this chapter, the development of the impedance controller for the AIRGAIT rehabilitation system is proposed. The joint compliance of the robot is controllable via estimation of a new defined human-robot interaction force. As a result, the support of the robotic orthosis varies with the disability level of patients following that the AAN training strategy is achieved. Furthermore, by using the bio-information feedback from EMG sensors, the patient’s muscle activations are also monitored and the robot orthosis can provide the assistance accordingly. Finally, experiments on the developed system with the participation of different subjects are conducted to verify the effectiveness of the proposed method.

4.3 Human Robot Interaction Force Based Impedance Controller

4.3.1 Control Design

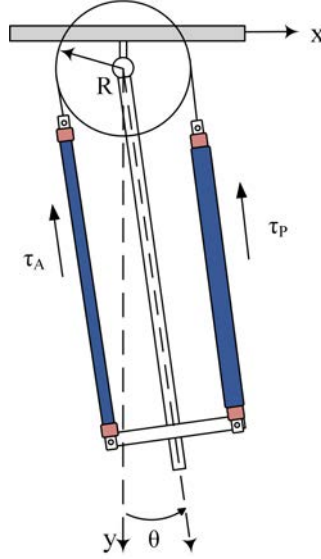


Figure 4.1: The typical antagonistic configuration.

AAN is one of the most important requirements of the robotic rehabilitation system due to the fact that the disability level of patients not only varies from subject to subject but also changes during the training process with each subject. In order to implement the AAN strategy, the disability level of the patient is needed to be estimated first. Then, the compliance of the system is changed accordingly to encourage patient effort during training.

This chapter begin with the joint compliance of antagonistic muscle in Fig. 4.1. In this study, the relationship between joint compliance and the nominal pressure in the work by Choi et al. [12] is employed. The spring torque of the anterior and posterior PAM is as following

$$\tau_{sA} = n [K_0 + K_1(P_{A0} - \Delta P)] y_A \cdot R \quad (4.1a)$$

$$\tau_{sP} = n [K_0 + K_1(P_{P0} + \Delta P)] y_P \cdot R \quad (4.1b)$$

in which K_0 and K_1 are the parameters of spring element of both PAMs which drive actuator, respectively. These parameters of the developed system are pro-

vided in Table 4.1. y_A and y_P are the contraction length of the anterior and posterior PAMs. R is the rotation radius of joint. n is number of PAMs. Following that, the torque by joint's spring force term is

$$\begin{aligned}\tau_s &= -\tau_{sA} + \tau_{sP} = \frac{\theta}{\gamma_j} \\ &= -n [K_0 + K_1(P_{A0} - \Delta P)] y_A \cdot R + n [K_0 + K_1(P_{P0} + \Delta P)] y_P \cdot R\end{aligned}\quad (4.2)$$

From (2.15), we have

$$y_A = y_{AN} + R\theta \quad (4.3a)$$

$$y_P = y_{PN} - R\theta \quad (4.3b)$$

Due to the similar lengths of anterior and posterior PAMs ($y_{AN} = y_{PN} = y_N$), we can obtain

$$\begin{aligned}\tau_s &= n [K_0 + K_1(P_{P0} + \Delta P)] (y_N - \theta R) R - n [K_0 + K_1(P_{A0} - \Delta P)] (y_N + \theta R) R \\ &= n(-2K_0 + 2K_1 y_N \Delta P + 2K_1 P_{A0} + K_1 P_{AP}) \theta R^2 + n K_1 P_{AP} y_N R\end{aligned}\quad (4.4)$$

The compliance γ_j of an antagonistic actuator powered by n couple of PAMs can be described by

$$\gamma_j = \frac{\theta}{n(-2K_0 + 2K_1 y_N \Delta P + 2K_1 P_{A0} + K_1 P_{AP}) \theta R^2 + n K_1 P_{AP} y_N R} \quad (4.5)$$

Note that θ and ΔP are regulated by the trajectory tracking controller while P_{AP} is fixed since it decides the initial position of the actuator. Therefore, the nominal pressure P_{A0} dominates the compliance of the actuators. For estimation of the

Table 4.1: The spring parameters of PAMs.

| Spring Element | Hip PAM | Knee PAM | Bi PAM |
|-----------------------|----------------|-----------------|---------------|
| K_0 [N] | 0.691 | 0.572 | 0.453 |
| K_1 [N/100kPa] | 1.096 | 0.835 | 1.217 |

disability level, a new strategy is proposed as follows. Define the human-robot interactive torque (HRIT) as

$$T_{int} = T_{int}^{passive} - T_h \quad (4.6)$$

4.3 Human Robot Interaction Force Based Impedance Controller

in which $T_h = [T_h^{hip} \ T_h^{knee}]$ are active torques represent the contributions of subjects to the movement of the robotic orthosis. The HRIT is measured by using bar-shaped load cells attached on the thigh and shank as shown in Figure 4.2a. If the effort of subjects is trivial, i.e., $T_h \approx [0 \ 0]$, the signals provided by the load cells represent the HRIT of the passive mode in which the disability level of the patient is highest and the robotic orthosis provides full support to dominate the movement of the lower limb. In this case, $T_{int} = T_{int}^{passive}$ is saved as the torque profile of the subject as illustrated by the black line in Figure 4.2b. If the subject generates active force which positively contributes to the movement ($T_h > 0$), the signal T_{int}^{active} from load cells tends to be smaller in comparison with $T_{int}^{passive}$ (Zone A in Figure 4.2b). In contrast, T_{int}^{active} increases when the active force against the movement of the robotic lower limb ($T_h < 0$) which is illustrated by Zone B in Figure 4.2b. This difference can be treated as human active torque T_h and is utilized to adjust the compliance of the robotic orthosis. Since $T_{int}^{passive}$ not only varies from subjects to subjects, but also changes with the same subject during the training process, the following procedure is proposed to online estimate T_h .

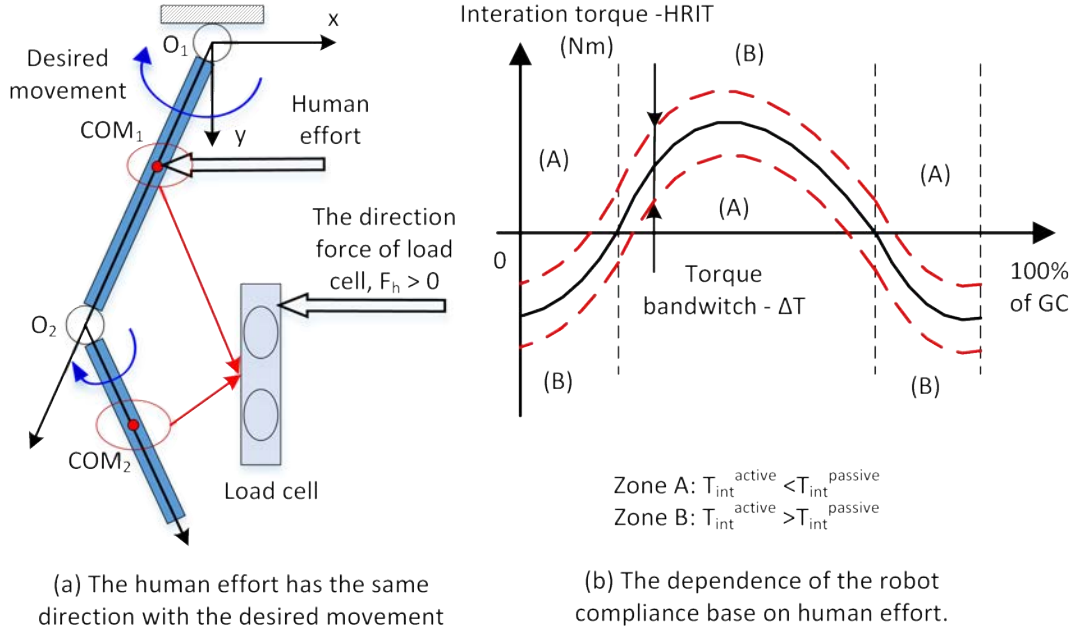


Figure 4.2: The compliance control method of the AIRGAIT robot orthosis: (a) The position of the load cell on robot orthosis and (b) the dependence of the robot compliance base on the human effort.

Step 1: At the beginning of the training process, the subject is asked to walk on the treadmill in passive mode with full support from the robotic orthosis. Then, the data from the load cells attached to the thigh and shank positions in 30 gait cycles (GCs) are saved as $T_{int}^{passive}$. This data is the basic profile of each subject and used during the training process.

Step 2: In this step, the subject is encouraged to move actively. The signals from the load cells in this step represent T_{int}^{active} . The active torque T_h generated by human effort can be estimated by

$$\hat{T}_h = T_{int}^{passive} - T_{int}^{active} \quad (4.7)$$

Based on the estimated \hat{T}_h , the compliance of the robotic orthosis is adjusted by the following rule

$$P_{tA,i} = \begin{cases} P_{0A,i} - K_{imp}\hat{T}_h \text{sgn}(T_{int}^{passive}) & \text{for } |\hat{T}_h| > \Delta T \\ P_{0A,i} & \text{for } |\hat{T}_h| \leq \Delta T \end{cases} \quad (4.8)$$

In Equation (4.8), ΔT is the width of a boundary layer in which $T_{int}^{passive}$ is the center. In experiment $\Delta T = 0.1T_{int}^{passive}$. $K_{imp} > 0$ is the gain of the compliance controller and $\text{sgn}(x)$ is the sign function of x :

$$\text{sgn}(x) = \begin{cases} +1 & \text{if } x > 0 \\ -1 & \text{if } x < 0 \\ 0 & \text{if } x = 0 \end{cases} \quad (4.9)$$

The block diagram of the proposed control system for each channel including AAN strategy is shown in Figure 4.3.

4.3.2 Experimental Procedure

To evaluate the performance of the proposed control strategy with the developed lower-limb robotic orthosis system, various experiments are conducted with the participation of eight healthy male subjects who do not have neurological disorders. The detail information about these subjects is given in Table 4.2. All subjects gave their written informed consents for inclusion before they participated in the experiments. The experiment protocol was approved by the Ethics Committee of Shibaura Institute of Technology.

The system is evaluated in two gait training modes including trajectory tracking mode and compliance control mode. The experiment time for each subject

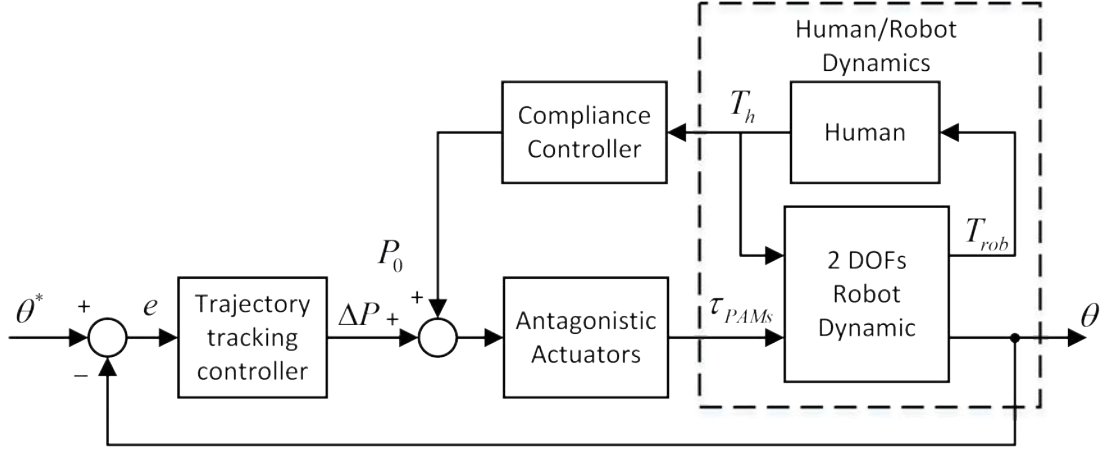


Figure 4.3: Compliance control architecture of the AIRGAIT robotic orthosis.

Table 4.2: The information of eight subjects.

| Information | Value (Mean \pm SD) |
|-------------------|-----------------------|
| Age (Years) | 29.7 \pm 3.9 |
| Body weight (kg) | 62.4 \pm 8.8 |
| Height (cm) | 166.2 \pm 4.0 |
| Shank length (cm) | 47.1 \pm 1.4 |
| Thigh length (cm) | 45.3 \pm 3.6 |

is about 10 min. In the first 5 min when the trajectory tracking mode is tested the robot compliance is set to the minimum value so that the movement of the subject lower limb is dominated by the robotic orthosis. The subject is also asked to completely relax. Therefore, the data of $T_{int}^{passive}$ in 30 GCs are collected and saved together with the desired and measured trajectories. In the next 5 min of the experiment, the robotic orthosis is switched to the compliance control mode. In this case, the subject is asked to be more active in moving. The data are also recorded in the last 30 GCs for further analysis.

During the experiments, the body weight support system is used due to the safety requirements for the subjects. The reference trajectories of the hip (θ_1^*) and knee (θ_2^*) mono-articular actuator are modified from the gait data profile in textbook [52] according to each subject with the maximum of hip and knee flexion/extension angles are $+20^\circ/-20^\circ$ and $45^\circ/0^\circ$, respectively. The speed of the treadmill is set at 2.2 km/h. The sampling frequency of the control system is

Table 4.3: The parameters of the proposed controller.

| Controller Channel | K_p | K_d | α | K_{imp} |
|---------------------|-------|----------------------|----------|-----------|
| Knee mono-articular | 0.05 | 0.8×10^{-3} | 0.80 | 0.20 |
| Hip mono-articular | 0.05 | 0.5×10^{-3} | 0.90 | 0.15 |
| Bi-articular | 0.04 | 1.0×10^{-3} | 0.85 | 0.25 |

100 Hz. Low pass filters with unity gain and 6 Hz cut-off frequency are employed to reduce the noise from signals getting from the load cells, pressure sensors as well the angle sensors. All analyses are carried out by MATLAB (MathWorks, Natick, MA, USA) software version R2016a. The parameters of the controllers after being well tuned are provided in Table 4.3.

4.3.3 Experimental Results

4.3.3.1 Trajectory Tracking Control

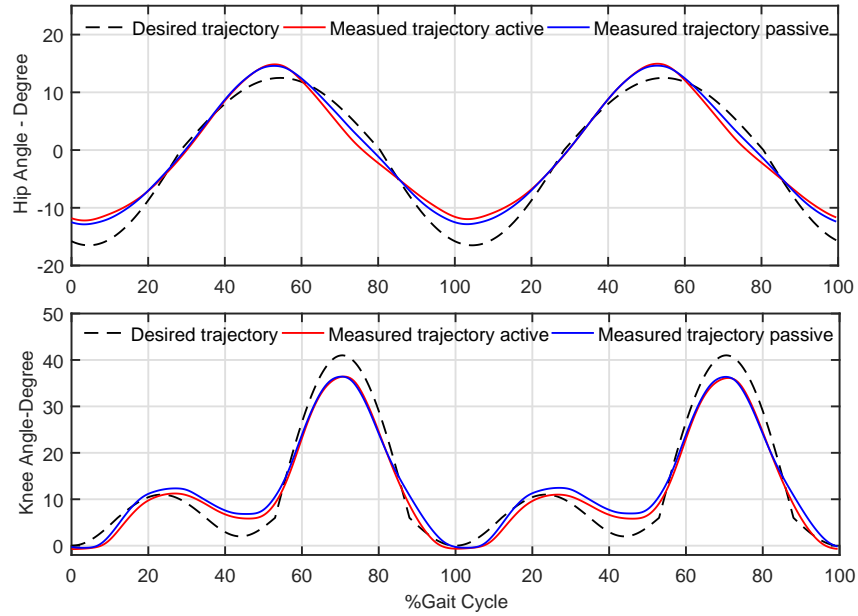


Figure 4.4: Trajectory tracking control performance of AIRGAIT robotic orthosis in passive mode (blue line) and active mode (red line). The gait data is normalized and plotted as reference trajectories.

4.3 Human Robot Interaction Force Based Impedance Controller

Table 4.4: Maximum tracking error (MTE), RMSTE and maximum compliance ($Comp^{max}$) of hip and knee joint in the experiment. Standard deviation (\pm) are presented for subject variability. * means the significantly improve.

| Gait Parameter | Passive Walking | | Active Walking | |
|------------------------------|-----------------|-----------|----------------|-------------|
| | AIRGAIT | 6-DOF[23] | AIRGAIT | 6-DOF[23] |
| MTE_{Hip} [degrees] | 4.25±1.01 | 3.96±1.08 | 5.7 ± 3.17* | 14.22 ± 3.2 |
| $RMSTE_{Hip}$ [degrees] | 2.09±0.14 | - | 3.04±1.91 | - |
| MTE_{Knee} [degrees] | 5.85±0.56 | 9.31±1.60 | 6.81±2.32* | 15.0 ± 4.15 |
| $RMSTE_{Knee}$ [degrees] | 3.09±0.70 | - | 3.16±1.26 | - |
| $Comp_{Hip}^{max}$ [rad/Nm] | 2.09±0.14 | 1.10±0.15 | 4.94±1.07 | 3.96±0.23 |
| $Comp_{Knee}^{max}$ [rad/Nm] | 5.08±0.20 | 2.93±0.36 | 9.01±0.40 | 11.4±0.58 |

First of all, we are going to evaluate the tracking performance of the system which is compensated the impedance controller. The process starts with the computerised record of the mean of all measured trajectories of participants to evaluate the performance of the system during trajectory tracking mode. Then follows by the maximum tracking error (MTE) and the RMSTE between the average and the desired trajectory are evaluated. Throughout the process, standard deviations (SDs) over the maximum joint angular and compliance errors of subjects are also considered for further study on the intersubject variability. These results are shown in detail in Table 4.4. The experimental results in passive and active modes are also depicted in Figure 4.4. As can be observed in Table 4.4, the MTEs and RMSTEs are below $5.85^\circ \pm 0.56$ and $4.25^\circ \pm 1.01$ for both hip and knee joints in passive walking mode. These values are not too much different from the equivalent values of the 6-DOF system in [23]. It means that the proposed controller has a similar control performance during passive mode with the 6-DOF system.

In active mode where the participants contribute force to the movement of their lower limb, the tracking performance is slightly degraded, i.e., $MTE = 6.81^\circ \pm 2.32$ and $RMSTE = 3.16^\circ \pm 1.26$. The proposed controller is able to provide the maximum values of joint compliances, i.e. 4.94 ± 1.07 and 9.01 ± 0.40 for knee and hip joints, respectively. These values are similar to the 6-DOF system which are 3.96 ± 0.23 and 11.4 ± 0.58 for hip and knee joints.

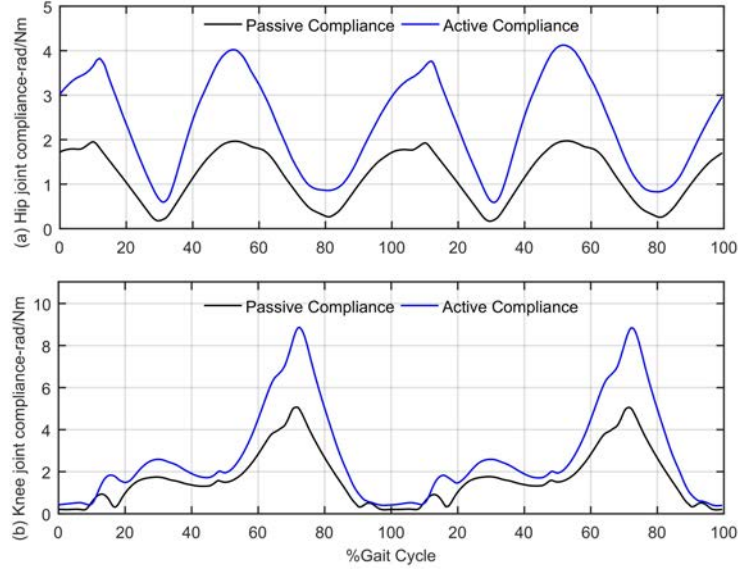


Figure 4.5: Joint sagittal plane compliance of AIRGAIT robot orthosis: (a) Hip joint and (b) Knee joint.

However the proposed controller is able to provide a better tracking performance ($MTE = 6.81^\circ \pm 2.32$) than the 6-DOF system ($MTE = 15.0 \pm 4.15$). Generally, these results are deemed suitable for rehabilitation system in practice. Also, the small value of SDs means that the control system is robust against the variance of the subjects and is able to guide different types of patients in the rehabilitation process.

4.3.3.2 Joint Compliance Control

The joint compliances of the robotic orthosis in tracking control and impedance control mode in the sagittal plane are shown in Figure 4.5. The torque profile of subjects $T_{int}^{passive}$ (the black line) and the estimation of the active human torque \hat{T}_h (the green line) are depicted in Figure 4.6. All these data are also averaged over all subjects for two GCs.

It can be observed that in passive mode, the compliance is set at low level such that movement of the lower limb is dominated by the robotic orthosis. When the subject is in active mode, T_{int}^{active} is outside the bandwidth where the center is the passive one $T_{int}^{passive}$. Consequently, the compliance controller increases the joint compliance to encourage the contributions of the subjects in training pro-

4.3 Human Robot Interaction Force Based Impedance Controller

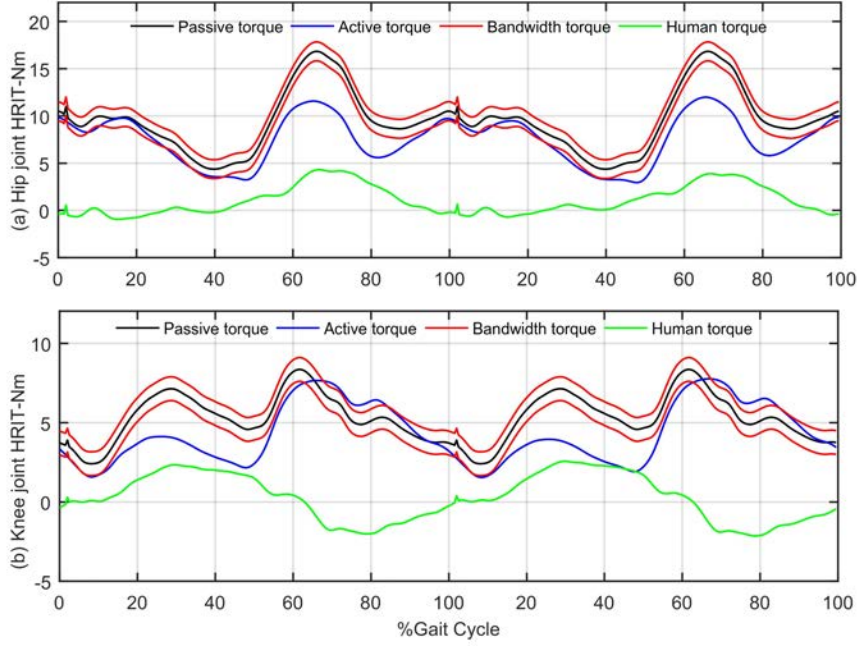


Figure 4.6: The human-robot interactive torque (HRIT) of AIRGAIT robotic orthosis during active and passive modes: (a) Hip joint and (b) Knee joint.

cess. For example, $|T_{int}^{active}| < |T_{int}^{passive}|$ in the first half of GC which means the robotic orthosis reduces the support to the subjects. The unexpected behavior of the system in the range of 60% to 100% of gait cycle in knee joint may be caused by the healthy subjects whose contribution against the movement of the robotic. However, the adaptation of the compliance demonstrated that the compliance controller is able to provide the assistance based on the effort of the subjects while the tracking controller is still stable to guide the subject limb. In comparison with the 6-DOF system, the proposed impedance control approach need two bar-shape load cells instead of the 4 load cells in series with the muscles. Due to the fact that the AIRGAIT orthosis is powered by an additional pair of bi-articular muscles. The number of used load cells will be 6 if the similar control approach in 6-DOF was applied to the AIRGAIT system. The proposed control method can optimize the cost of the system.

4.4 Muscles Activation Level Based Impedance Controller

4.4.1 The Equivalent Muscles in Subject Body of the AIR-GAIT Robotic Orthosis

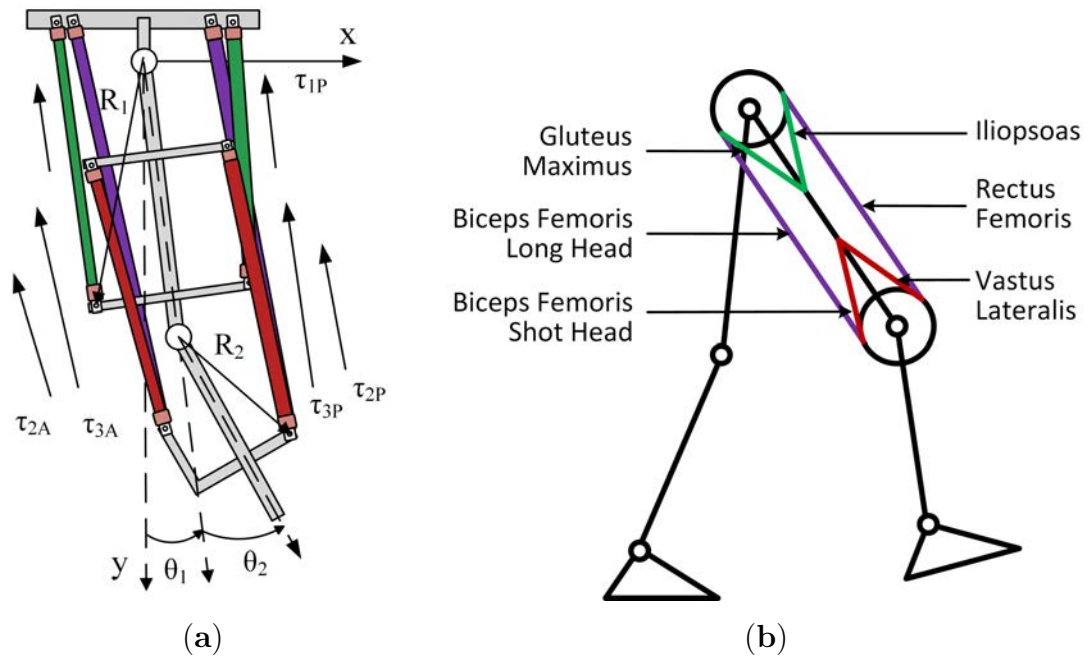


Figure 4.7: The muscle system: (a) The actuator arrangement of the AIRGAIT orthosis. (b) The human musculoskeletal system .

In the previous section of this chapter, the AIRGAIT gait training system is integrated the impedance controller based on the human-robot interaction force. Due to the fact that the patient disability is caused by different reasons, i.e., stroke or spinal cord injury, etc. which results in different responses of the patient muscles, the use of electromyography (EMG) sensor is going to be exploited. In that case, the AAN controller may evaluate the activity levels of the muscles and provide the assistance accordingly. This is expected to enhance the patient's volition during the gait training process. The AIRGAIT mechanism design have the actuator arrangement (Fig. 4.7a) similar to the human musculoskeletal system (Fig. 4.7b) in which Gluteus Maximus (GM), Iliopsoas muscles (IL), Biceps Femoris Long head (BFLH), Rectus Femoris (RF), Biceps Femoris Long head

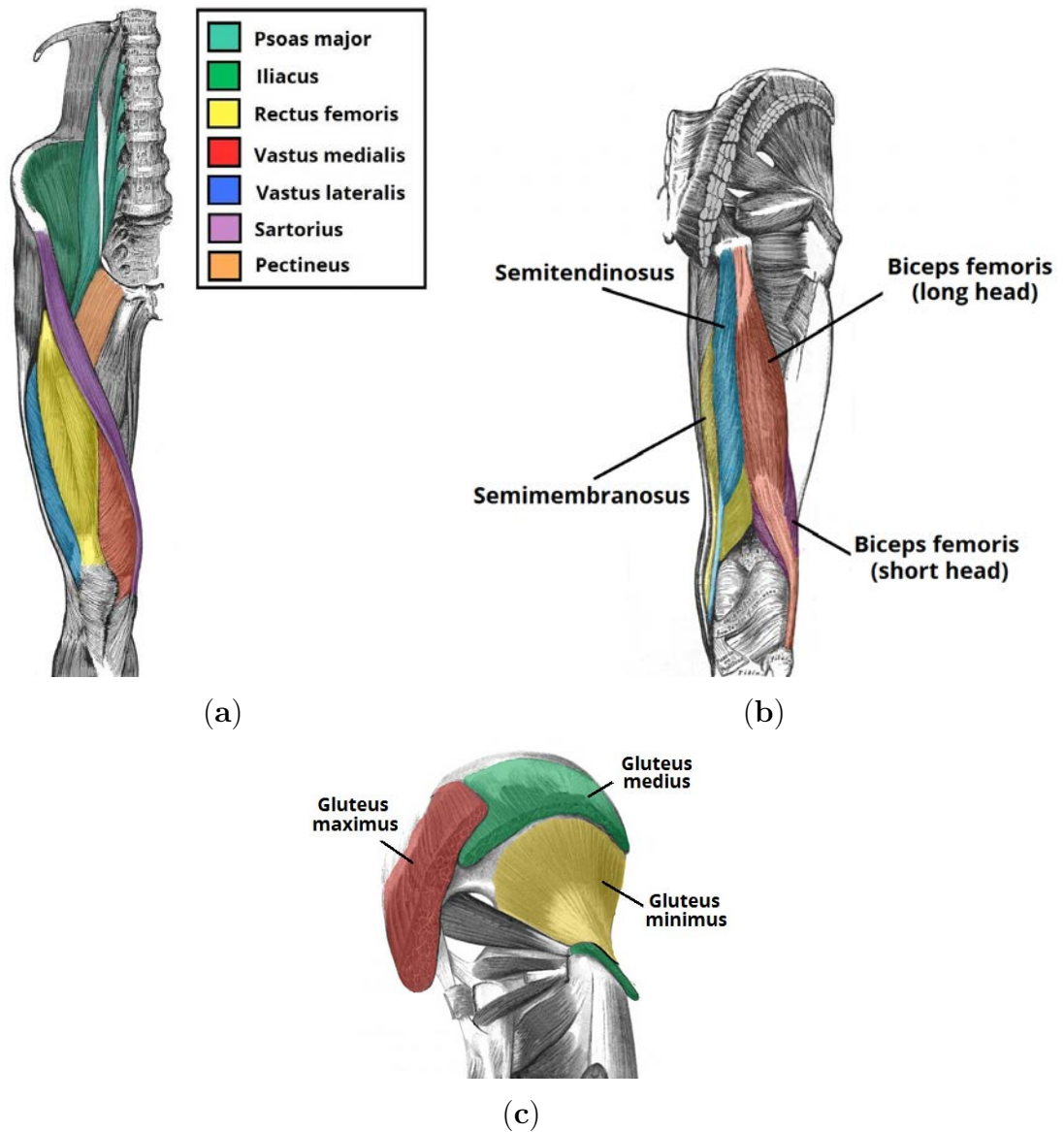


Figure 4.8: The muscle system: (a) The actuator arrangement of the AIRGAIT orthosis. (b) The human musculoskeletal system .

(BFSH), and Vastus Lateralis (VL) are the equivalent muscles. The specific positions of these muscles on the lower limb are shown in Fig. 4.8. However, the GM and IL mono-articular muscles are located on the hip area of the subject and very difficult to attach EMG sensors on them during the training process. Since, only four muscles RF, VL, BFLH, and BFSH which not belong to the gluteal region are monitored for assist control purpose. The detailed procedure for estimating the activation level of these muscles will be provided in the next section.

4.4.2 The Muscle Activation Level based EMG Signal

Table 4.5: The information of three subjects.

| Information | Value (Mean \pm SD) |
|-------------------|-----------------------|
| Age (Years) | 29.7 \pm 3.9 |
| Body weight (kg) | 62.4 \pm 8.8 |
| Height (cm) | 166.2 \pm 4.0 |
| Shank length (cm) | 47.1 \pm 1.4 |
| Thigh length (cm) | 45.3 \pm 3.6 |

In order to estimate the muscle activation level of a subject, the various experiments are conducted with three healthy male subjects who do not have neurological disorders. The detail information of the subject is provided in Table 4.5. All subjects gave their written informed consents for inclusion before they participated in the experiments. The experiment protocol was approved by the Ethics Committee of Shibaura Institute of Technology.

The EMG signals of the specific muscles are collected in three conditions including sitting, standing and walking on the treadmill with various speeds up to 3.5[km/h]. The subjects are asked to rest 5 minutes after each experiment by sitting on the chair. The data is recorded in 1 minute for analysis. All the walking data is processed by a full-wave rectifier and a 5[Hz] low-pass filter after that is standardized in the percentage of the subject gait cycle. Figure 4.9a illustrates the subject 1's standardized EMG signal of Vastus Lateralis muscle while he walking on the treadmill with a speed of 3.5[km/h]. The blue line presents the measured signal and the dash red line is the equivalent standardized signal which is resampled to the same frequency. All standardized EMG signals of the subject 1 are shown in the rest images of Fig. 4.9. The solid line presents the mean values and the shaded zone is the equivalent standard deviation in one gait cycle. For more detail assessment, the RMS value of EMG signal each muscle in one gait cycle is computed and provided in Fig. 4.10. As we can observe, the RMS value of EMG voltage of each muscle is increase when the subject change from the rest condition, i.e. sitting and standing, to the more active condition (walking). These values also increase when the subject speedup. It means that the RMS of

4.4 Muscles Activation Level Based Impedance Controller

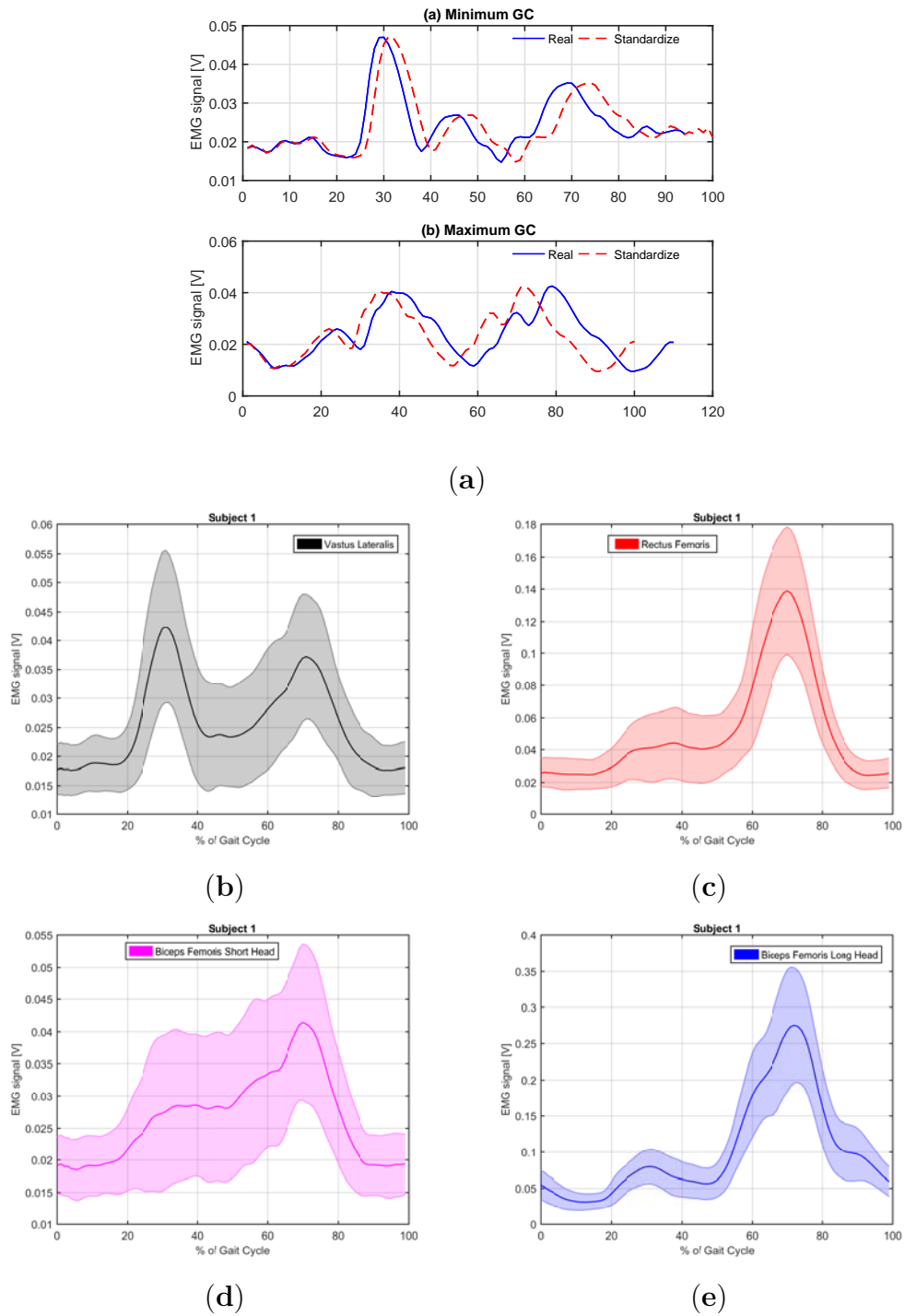


Figure 4.9: The example of subject 1's EMG signal: (a) standardized of Vastus Lateralis EMG signal. Means and standard deviations of the EMG signals after standardizing: (b) The Vastus Lateralis, (c) Rectus Femoris, (d) Biceps Femoris Short Head and (e) Biceps Femoris Long Head muscles.

4.4 Muscles Activation Level Based Impedance Controller

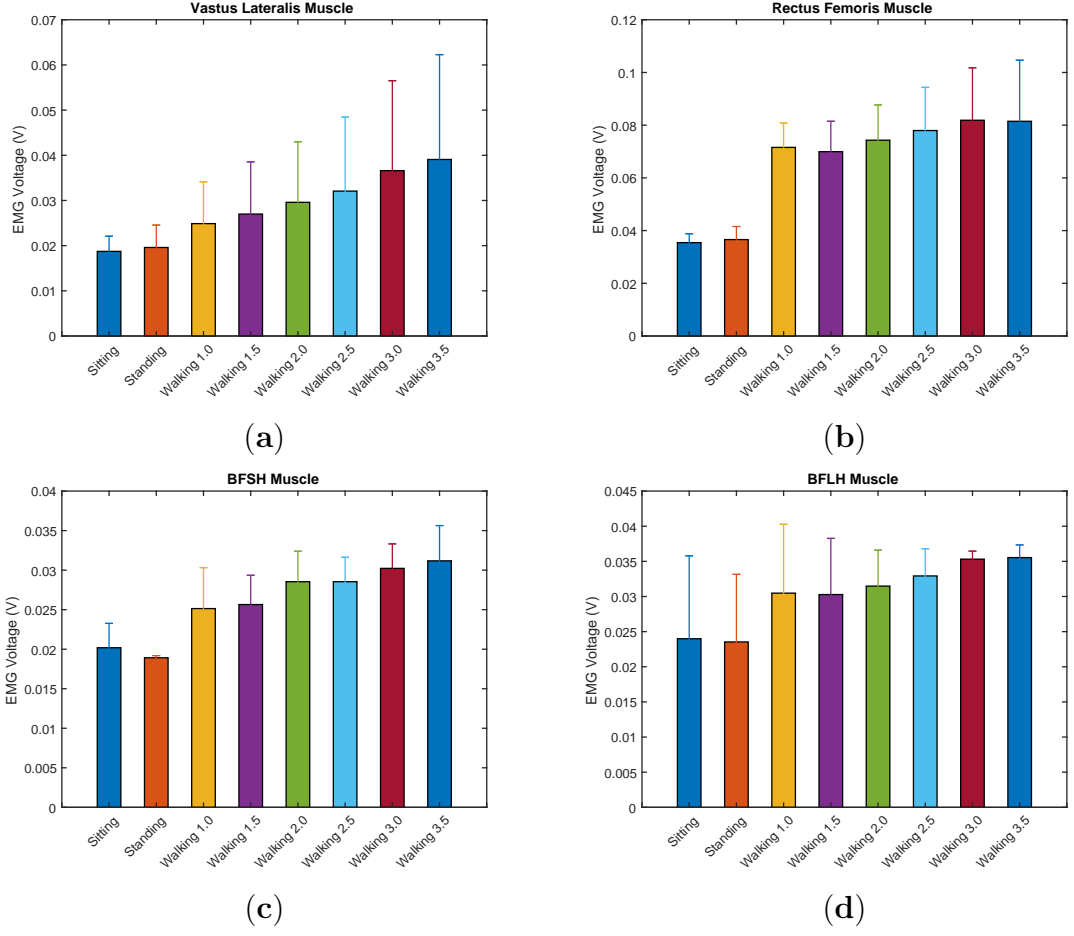


Figure 4.10: The RMS of EMG signal over all subjects: (a) The Vastus Laterelis, (b) Rectus Femoris, (c) Biceps Femoris Short Head and (d) Biceps Femoris Long Head muscles.

EMG voltage is proportional to the subject muscle activation level. Hence we can estimate the muscle torque from EMG voltage as the following linear equation

$$\tau_m = ae_m + b \quad (4.10)$$

in which a and b are the linear parameters. e_m is the RMS value of EMG voltage. Consequently, the torque which subject impact to the orthosis joint can be obtained as

$$\begin{bmatrix} T_1 \\ T_2 \end{bmatrix} = \begin{bmatrix} a_{11} & a_{12} & a_{13} & a_{14} \\ a_{21} & a_{22} & a_{23} & a_{24} \end{bmatrix} \begin{bmatrix} \tau_1 \\ \tau_2 \\ \vdots \\ \tau_4 \end{bmatrix} = \begin{bmatrix} 1 & -1 & 1 & -1 \\ 0 & 0 & 1 & -1 \end{bmatrix} \begin{bmatrix} \tau_1 \\ \tau_2 \\ \vdots \\ \tau_4 \end{bmatrix} \quad (4.11)$$

where T_1 and T_2 are the torques which subject impact to the robot joints, τ_i are the muscle torques, $i = 1 \rightarrow 4$ equivalent to RF, BFLH, VL, and BFSH muscles.

4.4.3 The EMG-Based Fuzzy Controller

Fuzzy Variables As discussed in the previous section, human muscle torques can

Table 4.6: The RMS range of each muscle's EMG voltage.

| Muscle name | Maximum value | Minimum value | Scale factor | |
|-------------|---------------|---------------|--------------|---------|
| | [V] | [V] | a | b |
| RF | 0.116 | 0.022 | 106.5 | -0.0575 |
| VL | 0.066 | 0.016 | 113.4 | -0.0651 |
| BFLH | 0.042 | 0.016 | 35.64 | -0.0781 |
| BFSH | 0.036 | 0.018 | 46.06 | -0.0733 |

be estimated by using EMG sensors. However, it is very difficult for the estimation to achieve high accuracy. Since in this research, the muscle torque τ_m is described by a fuzzy system in which τ_m is divided into seven levels from the lowest (level 1) to the most active (level 7) equivalent to the RMS range of the EMG voltage from the minimum to the maximum value. The detail range of the RMS value of each muscle is provided in Table 4.6. For practical purpose, the fuzzy system is designed in the Labview program and the *Gaussian shape* type is chosen for representing fuzzy variables. The RMS range of EMG voltage is scaled to the electric voltage from $0 \rightarrow 10[V]$ and the scale factors are also provided in Table 4.6. Consequently, the support level of the robotic orthosis also is designed as seven levels from the minimum assistant (level 1) to the maximum assistant (level 7) which equivalent to the range from level 7 to level 1 of muscle torque. The details fuzzy variables of the RMS EMG voltages and support levels of the orthosis are shown in Fig 4.11.

Fuzzy Rules Due to the fact that, the pair of bi-articular muscle RF and BFLH impact to both hip and knee joints, the mono pair knee articular muscle impacts to the knee joint only. Hence, the muscle torques τ_{RF} and τ_{BFLH} can be used to determine the assistant level of the robot for the hip joint and the sums $\tau_{RF} + \tau_{VL}$ and $\tau_{BFLH} + \tau_{BFSH}$ are used to determine the assistant level of the robot for the knee joint. The following fuzzy rules are chosen for the controller design.

4.4 Muscles Activation Level Based Impedance Controller

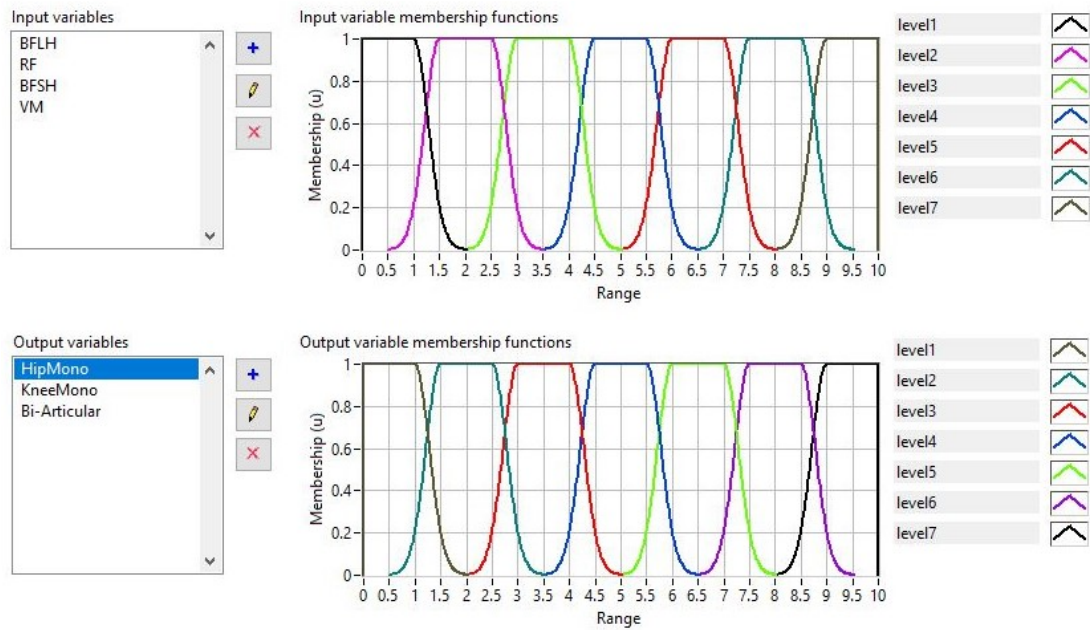


Figure 4.11: The system fuzzy variables designed in LabView.

- (-) Antecedent connective: OR (Maximum).
- (-) Defuzzification method: Center of area.

Example the assistant level of the hip joint is level 7 (the maximum assistant) if the muscle torque τ_{RF} or τ_{BFLH} is level 1 (the minimum activation level).

4.4.4 Simulation Results

The proposed EMG-based fuzzy controller is simulated by using the *Test System* function of the Fuzzy System Designer tool in LabView Program. The simulation result is illustrated in Fig. 4.12. From the simulation result, the assistant level of the robotic orthosis is inverse proportional to the equivalent muscle activation level which represented by the RMS of EMG voltage. Since the EMG-based fuzzy controller might be employed to the AIRGAIT orthosis experiment system. This works can be done in the near future.

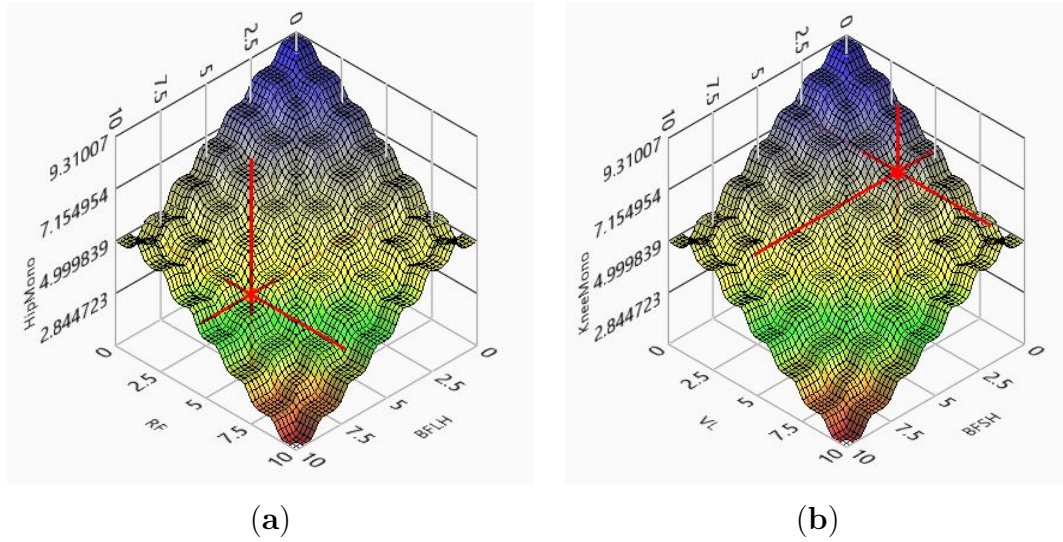


Figure 4.12: The simulation result of EMG-based fuzzy controller: (a) The hip joint and (b) knee joint assistant level.

4.5 Conclusions

In this chapter, the control system for the developed AIRGAIT lower limb robotic orthosis is continued to be improved. First, a new compliance controller based on new defined human-robot interactive torque and human active torque is proposed. As a result, the AAN strategy is successfully implemented, i.e., the robotic orthosis dominates the movement of subjects in passive mode and reduces the support when the subjects become more active. Besides, the modified computed torque controller is still able to track the designated trajectory.

Due to the fact that different type of patients, i.e. a stroke patient or SCI, lead to different activation of the muscles. The estimation of the human muscle activation level by using EMG sensors is also introduced in this chapter. The estimation level of the human muscle torques are directly proportional to the RMS value of EMG signals, and the EMG-based fuzzy controller is able to provide the assistance accordingly. The significance in simulation results illustrates the applicability of the proposed controller. In future works, the effectiveness of the EMG-based fuzzy controller should be verified by the experiment with the participation of a subject. In order to bring the AIRGAIT system to commercial, more incident conditions also must be considered and implemented to the system for safety enhancement in the next step of this research.

Chapter 5

Troubleshooting of the AIRGAIT System

5.1 Introduction

Because all systems always meet the trouble during operation. Many reasons which come from the environment or the inherent components of the system such as sensor faults, actuator malfunctions, or the interrupt of any power sources, etc. might lead to the system failure. Since the detection of any malfunctions and troubleshoot the cause is the requirement of any system.

In the work reported by Graham *et al.* in 1986 [66], the sensor fusion method is useful to detect high-risk obstacles in the workspace and prevent the robot from the robot colliding with these obstacles. The similar conclusion also reported by Karlson *et al.* [67]. Ohashi *et al.* [68] proposed the method to stop the robot in front of an obstacle by utilizing the arm force which is generated as a function of the robot body to the obstacle. However, these researches focused on the hazards caused by the environment effect only.

To reduce collision injury come from the inside components of the system, Zinn *et al.* [69] employed the new actuator mechanism which includes low- and high- frequency terms. For enhance human safety during collisions, Choi and Lee [12, 35] investigated pneumatic artificial muscles (PAMs). PAMs are attractive actuators in the rehabilitation robot field due to their safety characteristic. Besides, PAMs also have many advantages such as intrinsic elasticity, high ratio of torque from their weight and size. In case of rehabilitation robot, PAMs have been applied in many developed systems [3, 6, 8, 9, 11, 27]. However, the detail

reasons of the collision injury have not been considered in these systems.

Similarity with the above mentioned systems, the AIRGAIT robotic orthosis for gait training employed PAMs as its actuator [18]. It can guide the subject's limbs to the designated trajectory by using a modified computed torque control approach [70]. To provide the AAN training strategy, the impedance control method also implemented to the AIRGAIT system by using the new defined human active torque [61]. In this chapter, some frequent troubles of the AIRGAIT orthosis are investigated and the proper procedure to solve them is considered. Experiment results which are carried out without the participation of any subject show that the control system of the AIRGAIT orthosis can detect any malfunctions inside the system and provide the suitable solution for safety enhancement for the patients.

5.2 Contribution

This chapter addresses the safety issues of the AIRGAIT robotic orthosis. Firstly, common problems of the system are carefully investigated and classified into three groups based on their sources including sensor malfunction, actuator broken, and interrupt of power sources. Secondly, the developed control system capable of detecting the failure and choosing the suitable methods for accident risk reduction. The effectiveness of the proposed method is confirmed by experimental results without the participation of any subject.

5.3 Failure Classification

To enhance the safety of the patient during training, all the hazards must be determined and classified first. The failures lead to hazard can be caused by a broken system mechanism as well as environmental conditions. In this section, we focus only on the failures which occur inside the system mechanism. Base on the cause of the failure we can classify these types of failure base on their causes: sensor malfunction, actuators are broken and interrupt of power sources as shown in Fig.5.1. Base on the critical level of the danger, these failures can be divided into two types fatal and minor errors.

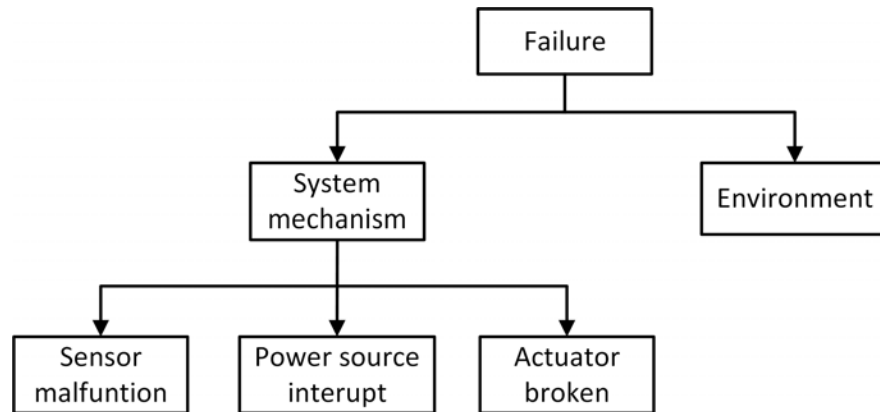


Figure 5.1: The failure classification.

Sensor Malfunction

In the case of the AIRGAIT orthosis, some types of sensor are used including EMG sensors, load cells, potentiometers, and pressure sensors. The potentiometer named CP-20H of Midori Precisions, Japan is used for the trajectory tracking purpose. The load cell LC62SP-20KG from Omega, USA and the P-EMG Plus from Oisaka, Japan is implemented for AAN training strategy. The pressure inside PAM is measured by integrated sensors of proportional electric control valves ITV2000/3000 of SMC company. The pressure is used for monitoring and collecting data. Under the safety point of view, if the trajectory tracking controller is out of control, the robotic orthosis will deviate from the predefined trajectory and the patient will be pained so much by the collision. The malfunction of the potentiometer which leads to the tracking out of control is the fatal error. Since the system must be stopped immediately if the potentiometer malfunction occurs.

If the load cells or the EMG sensors do not work properly, the AIRGAIT system can not provide the optimal training strategy for patients. However, the missing of these sensors do not lead to collision injury to the patients. The malfunctions of these sensors are minor errors. The control system does not need to stop the device immediately and indicate the warning signal to the operator. Similar conclusion is carried out by the case of the broken pressure sensor.

Broken Actuator

The high compliant PAM is used to actuate the robotic exoskeleton of the AIRGAIT system. The PAMs are arranged similar to the human musculoskeletal system including two pair of mono-articular muscles, and one pair of additional

bi-articular muscles connecting between hip and knee joint. Since the AIRGAIT robotic orthosis can provide not only more power but also more redundancy in comparison to similar systems. As a result, it is more safety for the patient during the training process. However, all the actuators are controlled to provide the needed torque for guiding the subject's limbs to the predefined trajectory. If any muscles are broken or not working properly, the robotic orthosis is not strong enough to lead the subject's limbs normally. Since the control system must detect the broken muscle and give the suitable control procedure to ensure the safety for patients. The failure of the PAM is also a fatal error.

The power source interruption

One thing for sure that no system can work properly with the interruption of any power source. The missing of the power sources is the fatal error, and the system must be stopped immediately. In the AIRGAIT system, electrical power is used for supplying the sensors and control system. Besides, the PAM is supplied by the pneumatic power source via the electric proportional control valve. The workings of two power sources are monitoring for safety enhancement.

5.4 Safety Enhancement Procedure

5.4.1 General Definition

Table 5.1: The Equivalent Range of the Sensor System.

| Sensors | Physical Signal Range | Sensor's Voltage Range | Gain |
|-----------------|-----------------------|------------------------|------|
| Potentiometer | -170 ~ 170 [°] | 0 ~ 5 [V] | 2.0 |
| Pressure Sensor | 0 ~ 1.0 [MPa] | 0 ~ 10 [V] | 1.0 |
| Load cell | 0 ~ 20 [N] | 0 ~ 10 [V] | 1.0 |
| EMG sensor | - | 0 ~ 10 [V] | 1.0 |

First of all, some following basic notation and definitions are the starting point of our exposition.

Definition 5.1 *All the sensors physical signal ranges will be converted to the electrical voltage from 0V to 10V via an amplifier or the proportional gain in software. The detail physical value of each sensor and the equivalent gain are provided in Table 5.1.*

Definition 5.2 *The output signal of each controller is in the range from 0V to 10V of the analog output channel.*

Definition 5.3 *Because all the sensors always send the signal greater than zero even the measured physical value is zero. In this research, we define U_{min} is the minimum voltage which represents the input signal when the physical value is zero.*

Definition 5.4 *If there is any break in a sensor or wires which connect the sensor to the analog input module, the voltage of the equivalent channel is 10V.*

5.4.2 Safety Enhancement Procedure

For safety requirements of the patients during the training process, the control system must detect any fatal errors occur and stop the device as soon as possible. When a minor error occurs, the information about it must also be informed to the operator, i.e. the message on the screen, and the procedure to solve it together. The detailed procedure for safety enhancement as shown in Fig. 5.2.

Sensor broken detection and the power source interruption

First of all, the control program acquires all the input signals from the sensors. If all the sensors work properly, their input voltage will be less than $V_{in} \leq U_{max}$. If the input voltage reaches the maximum value $V_{in} = U_{max}$, the control system starts to count the time t_{max} which represents the time the signal reaches the maximum value. Because of the continuous movement of the robot, this time is not too long. In this research $t_{lim} = 0.2$ seconds is chosen as the limited time of t_{max} . It is equivalent to about 10% of GC time and greater than $\theta = 0.1$ seconds which is the dead time of the control valve. If the time t_{max} is greater than or equal t_{lim} , it means that the sensor is broken or the wire is damaged. The type of broken sensors can be determined by the physical address of the analog channels. If the broken sensors are pressure sensors or potentiometers, it is a fatal error of

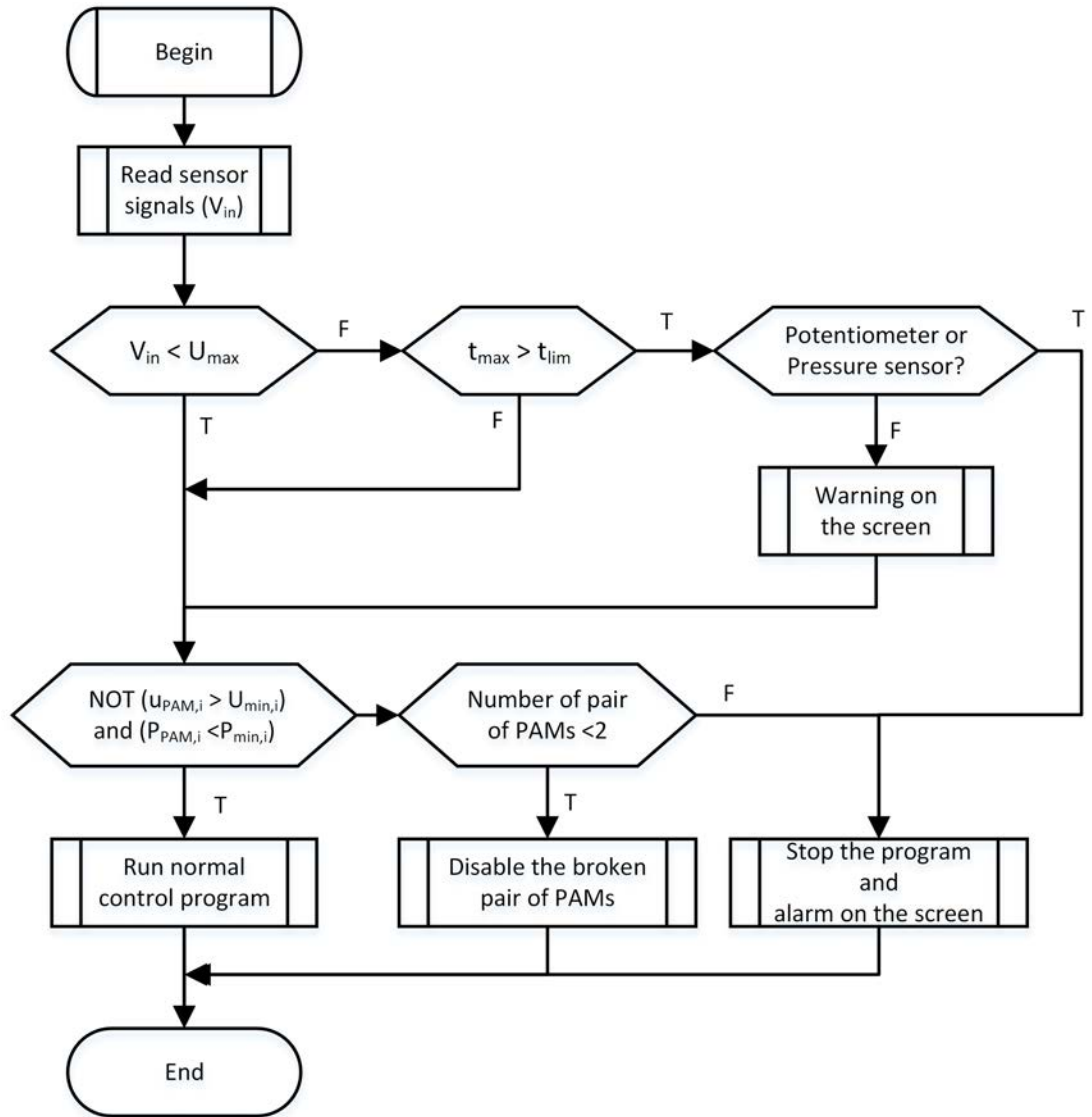


Figure 5.2: The flowchart for determining the safety procedure.

the device and the control program will stop the system to prevent the patient from the collision injury. The safety of the patient is also ensured by the BWS system. If the broken sensors are the load cells or EMG sensors, the AIRGAIT system cannot operate the AAN training strategy. The warning message will be pop up on the screen together with the alarm sound to notify the therapy about the error. The system will automatically stop after 2 minutes from the minor errors occur.

The similar safety procedure is given when having any interruption of the power source which is also the fatal error.

Broken PAM

Table 5.2: The minimum pressure inside each PAMs.

| PAMs | Minimum pressure (x100 kPa) |
|--------------------------------------|-----------------------------|
| Anterior PAM of bi-articular | 0.7583 |
| Posterior PAM of bi-articular | 0.0836 |
| Anterior PAM of knee mono-articular | 0.1165 |
| Posterior PAM of knee mono-articular | 0.8671 |
| Anterior PAM of hip mono-articular | 1.3908 |
| Posterior PAM of hip mono-articular | 1.2774 |

If all the sensors work properly, the control program will check the status of the PAMs. Due to the control strategy of the AIRGAIT robotic orthosis, the pressure inside each PAMs (P_i) always greater than $P_{min,i}$. The broken PAM can be concluded if the pressure $P_i < P_{min}$ while control voltage send to the equivalent ECV greater than $U_{min,i}$. The authors refer the reader to the paper [61] for more details regarding the control strategy of the AIRGAIT robotic orthosis. These minimum values are obtained by measuring the pressures inside each PAMs during the normal operation of the orthosis and are provided in Table 5.2. The AIRGAIT robotic orthosis is designed base on the human musculoskeletal configuration with an additional bi-articular muscle connecting between the hip and knee joints. The existence of an antagonistic pair of bi-articular muscles can provide more redundancy for the system. Since, if have one PAM is broken, i.e. the anterior hip mono-articular PAM, the control program will stop the paired PAM of it, i.e. the posterior hip mono-articular PAM. As a result, the robotic orthosis is continuously powered by the rest pair of muscles which are knee mono-articular and bi-articular muscles. It reduces the collision injury which is caused by loss control of the system. For more safety enhancement, the control program also informs the operator about the error and stop the system after 2 minutes.

5.5 Experimental Evaluation

The sampling time of the control program is set to $T_s = 10ms$, since all the hardware failure such as sensor malfunction, wire disconnect, lost of the power source,

etc can be detected in one scan cycle. In this section, only the safety enhancement is ensured by redundancy in actuators of the AIRGAIT robotic exoskeleton is evaluated. Various experiments are conducted without the participation of a subject. Firstly, the robotic exoskeleton is operated in trajectory tracking mode. After that, the broken PAM is simulated by suddenly stop the air which is supplied to the equivalent PAM. Because of the pair of PAMs are used for each anterior and posterior hip mono-articular muscle, since we can assume that the redundancy of the hip mono-articular is enough for the safety. The other PAMs including anterior, posterior of knee mono-articular, and bi-articular muscles are tested.

The experimental results are shown in Fig. 5.3. The dashed blue and the black lines represent for the desired and measured trajectories of each joint. The simulation signal of the PAM fault (green line) changes from “0” to “1” when the PAM is broken, and the detection signal (red line) also changes its level when the control system detects the fault. From experiment results, we can

Table 5.3: The detection time of the system when the broken PAMs.

| Broken PAM | Time to detect (s) |
|--------------------------------------|---------------------------|
| Anterior PAM of bi-articular | 0.50 |
| Posterior PAM of bi-articular | 0.25 |
| Anterior PAM of knee mono-articular | 0.24 |
| Posterior PAM of knee mono-articular | 0.37 |

conclude that the orthosis is still able to track the desired trajectories and not too much deviation in trajectories before and after the broken PAMs event occur. Particular, the time which the control system can detect the broken PAMs is less than 0.5 seconds. The detail values of the detection time equivalent to each case of broken PAMs are provided in Table 5.3. As a result, the control system can prevent the patient from the collision injure during the training process.

5.6 Conclusions

In this chapter, the control system of the AIRGAIT robotic orthosis is continued to be improved by integrating the safety procedure. The common risks, i.e. sensor

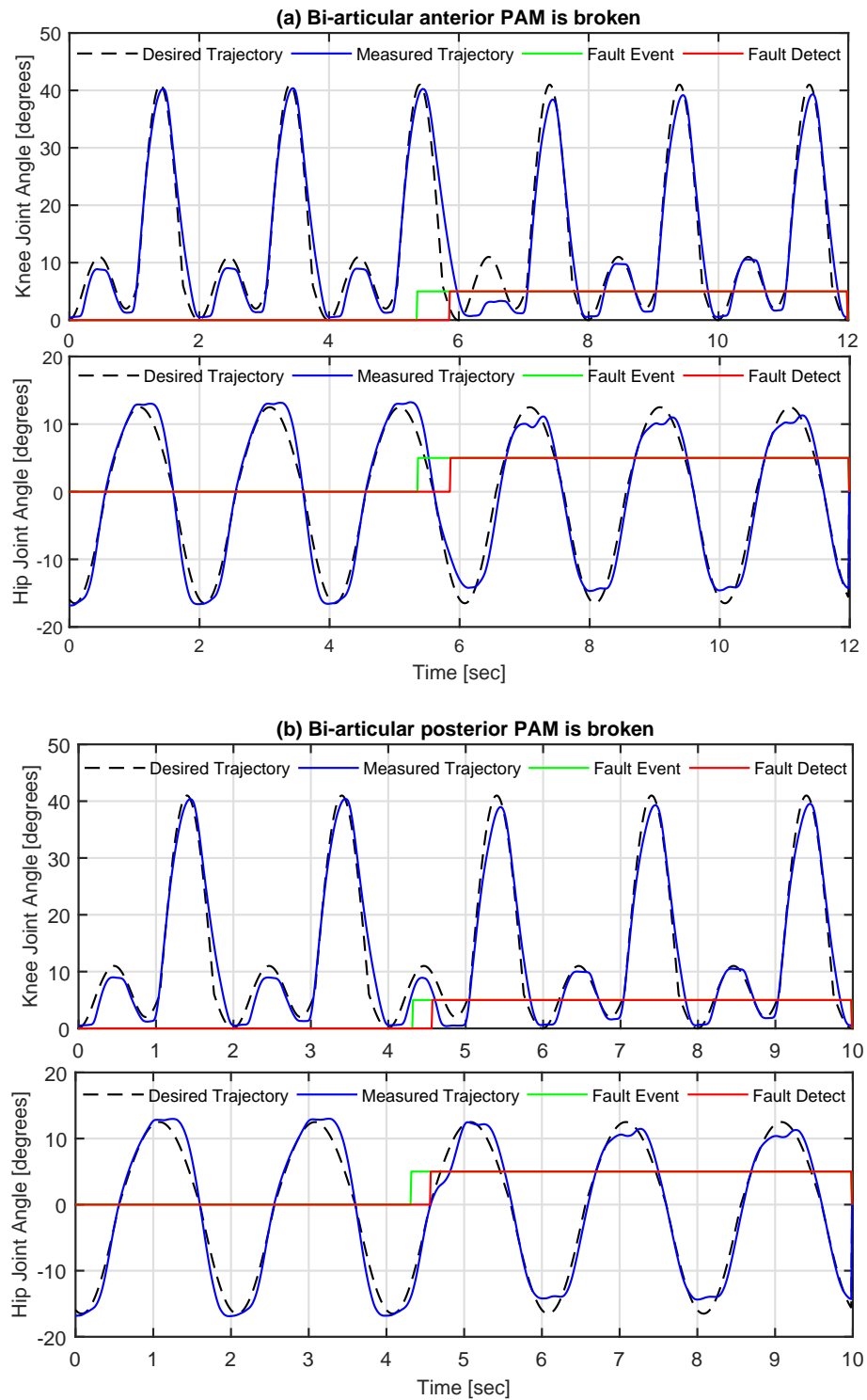


Figure 5.3: The detection of broken PAMs: (a) Anterior PAM and (b) posterior PAM of bi-articular muscles.

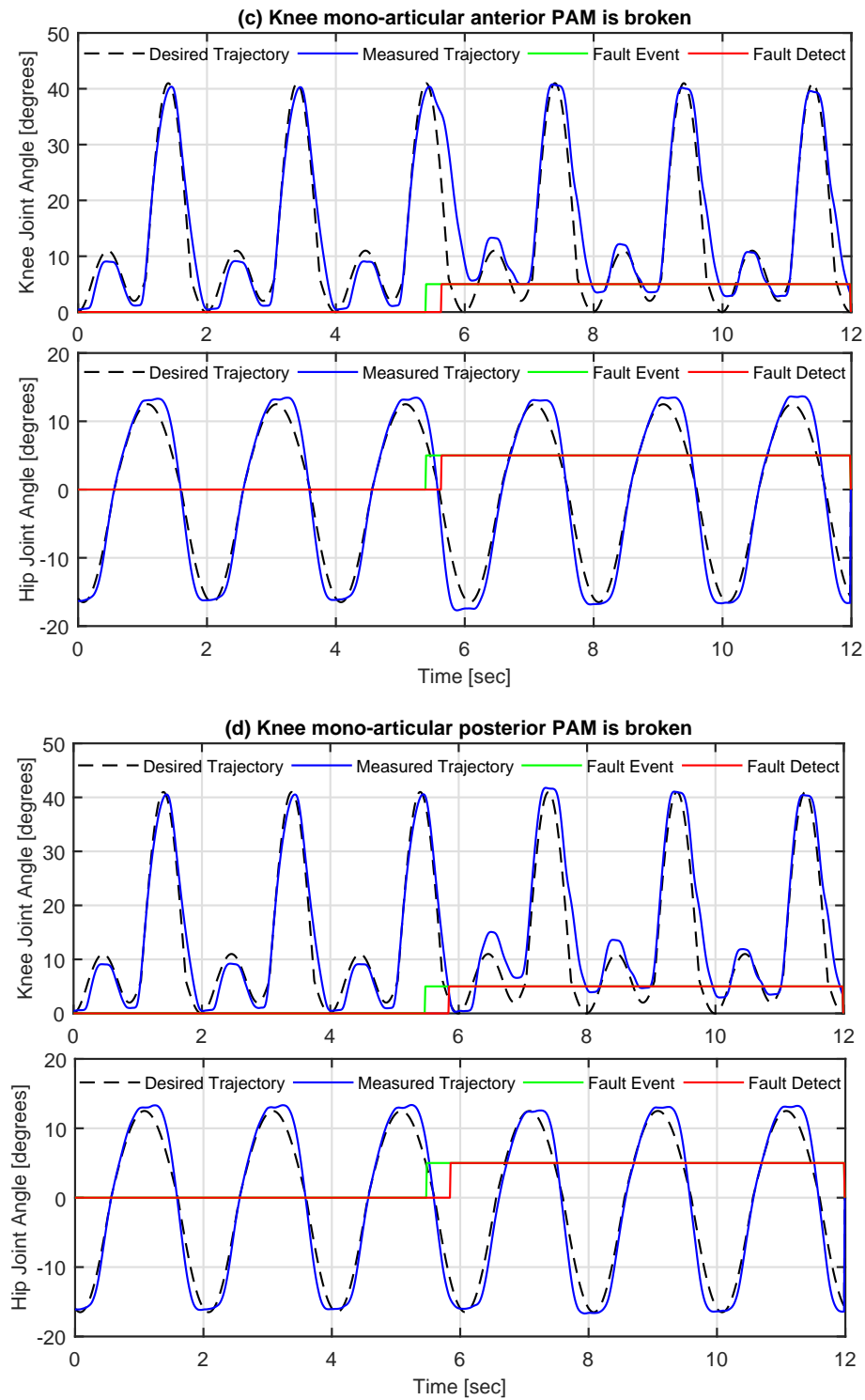


Figure 5.3: The detection of broken PAMs: (c) anterior PAM and (d) posterior PAM of knee mono-articular muscles.

malfunction, an actuator is broken, and interrupt of power sources, which may lead to the injury of the patient are carefully investigated. After that, based on the safety requirement, these risks are classified into two main groups including minor and fatal errors together with their suitable safety solutions. Particularly, the redundancy of additional bi-articular muscles allows the AIRGAIT orthosis to continue the trajectory tracking mode even if the case of broken PAMs. The time to detect the fault of PAM is less than 0.5 seconds, it might reduce the risk to the patient during training. The content of this chapter is a necessary step to bring the AIRGAIT system to become a commercial product.

Chapter 6

Conclusions and Recommendation

6.1 Conclusions

Aiming to develop the AIRGAIT system towards commercialization, numerous control strategies are implemented in this study to improve the trajectory tracking performance as well as integrated the new function such as assist-as-needed training strategy to the system.

First, throughout the literature reviews on existing reports of the modeling and control of single pneumatic muscle or PAMs in antagonistic configuration, both linear and nonlinear mathematical model types are carefully reviewed together with the equivalent control algorithms in *Chapter 2*. Even though many considerable studies have been reported, it could be said that the field is still wide open in both modeling and control algorithm of PAMs. This chapter also introduces a feedforward-feedback control strategy for an antagonistic actuator. Both control algorithms use a linear discrete-time second order plus dead time model to describe the behavior of the actuator. This type of model requires a simple procedure for identifying the model parameters. In advanced, high performance is fulfilled for trajectory tracking purpose. With the proposed control principle, a nominal pressure is supplied to both PAMs can provide a good stiffness for the antagonistic muscles. The joint angle of the actuator is controllable by regulating the different pressure in both PAMs. This chapter also introduces a feedforward-feedback control strategy and a discrete-time fractional order integral sliding mode controller for trajectory tracking purpose of an antagonistic actuator. Both control algorithms use a linear discrete-time second order plus dead time model to describe the behavior of the actuator. The identification procedure

of the proposed model is simplified. Experiment results show that both proposed controllers achieve better performances than the existing control approaches of the AIRGAIT system in the literature.

Second, the trajectory tracking control of the AIRGAIT robotic orthosis is proposed in *Chapter 3*. In comparison with the other PAM based rehabilitation systems, the novelty of the AIRGAIT orthosis is an additional pair of bi-articular muscle in actuator arrangement which similar to the human musculoskeletal system. The existing of the bi-articular muscles provide more powerful and redundancy for the system. However, this pair of muscle also makes the modeling and control of the system more complicated. In this chapter, the behavior of the robotic exoskeleton which considers the contribution of the additional bi-articular muscles is built. Based on the built-in model, the modified computed torque control strategy is investigated for the trajectory tracking purpose. Particularly, the fractional order calculus $PI^\alpha D^\beta$ of the integration and differentiation term is used instead of the conventional integer ones. The fractional order controller offers more degree of freedom which can be utilized to further improve the tracking performance. By implementing the proposed controller, the AIRGAIT robotic orthosis can track the 0.5 Hz desired trajectory which equivalent to about 2.2 km/h of the treadmill speed. In comparison with the conventional computed torque controller, the proposed control algorithm provides a better performance not only in the steady state but also during the transient process. This result is also much better than any existing control approaches of the AIRGAIT system. This result is also in accordance with the commercial gait training system LOKOMAT [26], in which the MTE is 15°.

The assist-as-needed training strategy is one of the most important requirements of any rehabilitation system because disability level of patients not only varies from subject to subject but also changes during the training process with each subject. Since the control system must be able to measure or estimate the disability level of the patient and change the robot impedance accordingly to encourage patient effort. *Chapter 4* of this thesis presents a development of impedance controller for AIRGAIT robotic orthosis. Base on the control algorithm of PAMs in the antagonistic configuration in *Chapter 2*, the compliance of the antagonistic actuator can be controlled by regulating the nominal pressure of both two PAMs. Also in this chapter, the patient's effort is estimated by the load cell by introducing the new defined human active torque. As a result, the

support of the robotic varies with the patient's effort following that the AAN training strategy is achieved.

Finally, *Chapter 5* presents the troubleshooting of the AIRGAIT system. In rehabilitation devices, the safety of the patient who interacts directly with the robot is the highest priority. All the common issues might lead to the hazard of the patient during training such as sensors malfunction, broken actuators, or the interrupt of any power sources, etc. have been carefully investigated first. After that, based on the safety requirement, the control system classifies these risks and give suitable safety solutions. Particularly, the redundancy of additional bi-articular muscles allows the AIRGAIT orthosis to prevent the patients from collision injury even the case of broken PAM. This troubleshooting helps the AIRGAIT system go one step ahead on the way to become a commercial product.

6.2 Recommendation and Future Works

Throughout this study, the author continues to develop the control system of the AIRGAIT robotic orthosis. Although the performance is much improved as well as the AAN training strategy is integrated into the system, the robot exoskeleton is designed to operate independently only. The other parts of the system, i.e. the body weight support, the treadmill are operated separately by therapy. Hence in the next step of this study, the synchronization of all elements of the AIRGAIT system should be considered. The following recommendations are going to exploit shortly:

- (1) To automatically synchronize the speed of the robot exoskeleton with the treadmill speed for more convenience for the therapy during training.
- (2) To combine the AAN training strategy of the robot exoskeleton with the control system of BWS in which the support level also change according to the patient disability level.
- (3) To estimate the disability level of the subject by using an observer to reduce the used sensors, i.e. load cell or EMG sensor. This is necessary to optimize the cost of the system and bring it home.

6.2 Recommendation and Future Works

- (4) To continue improving the performance of the system by applying other advanced control strategies.
- (5) To integrate some tools for statistic and analysis the training data. It would be helpful for the therapy to provide more effective rehabilitation to the patient.

References

- [1] A. Wernig, A. Nanassy, and S. Mueller, “Maintenance of locomotor abilities following laufband (treadmill) therapy in para- and tetraplegic persons: follow-up studies,” *Spinal Cord*, vol. 36, pp. 744–749, 1998.
- [2] A. Wernig, S. Müller, A. Nanassy, and E. Cagol, “Laufband therapy based on ‘rules of spinal locomotion’ is effective in spinal cord injured persons,” *European Journal of Neuroscience*, vol. 7, no. 4, pp. 823–829, 1995.
- [3] D. A. N. Claysson B Vimieiro, Breno G Nascimento and M. Pinotti, “Development of a hip orthosis using pneumatic artificial,” in *Proceeding of TMSi*, pp. 1–4, ABCM, 2005.
- [4] K. Bharadwaj and T. G. Sugar, “Kinematics of a robotic gait trainer for stroke rehabilitation,” in *Proceedings 2006 IEEE International Conference on Robotics and Automation, 2006. ICRA 2006.*, pp. 3492–3497, May 2006.
- [5] D. P. Ferris, K. E. Gordon, G. S. Sawicki, and A. Peethambaran, “An improved powered ankle foot orthosis using proportional myoelectric control,” *Gait Posture*, vol. 23, no. 4, pp. 425–428, 2006.
- [6] N. Costa, M. Bezdicek, M. Brown, J. O. Gray, D. G. Caldwell, and S. Hutchins, “Joint motion control of a powered lower limb orthosis for rehabilitation,” *International Journal of Automation and Computing*, vol. 3, pp. 271–281, Jul 2006.
- [7] T. Miyoshi, K. Hiramatsu, S.-I. Yamamoto, K. Nakazawa, and M. Akai, “Robotic gait trainer in water: Development of an underwater gait-training orthosis,” *Disability and Rehabilitation*, vol. 30, no. 2, pp. 81–87, 2008. PMID: 17852216.
- [8] G. S. Sawicki and D. P. Ferris, “A pneumatically powered knee-ankle-foot orthosis (kafo) with myoelectric activation and inhibition,” *Journal of NeuroEngineering and Rehabilitation*, vol. 6, p. 23, Jun 2009.

-
- [9] S. Hussain, S. Q. Xie, P. K. Jamwal, and J. Parsons, “An intrinsically compliant robotic orthosis for treadmill training,” *Medical Engineering and Physics*, vol. 34, no. 10, pp. 1448 – 1453, 2012.
- [10] K. E. Gordon, G. S. Sawicki, and D. P. Ferris, “Mechanical performance of artificial pneumatic muscles to power an ankle–foot orthosis,” *Journal of Biomechanics*, vol. 39, no. 10, pp. 1832 – 1841, 2006.
- [11] P. Beyl, K. Knaepen, S. Duerinck, M. V. Damme, B. Vanderborght, R. Meeusen, and D. Lefeber, “Safe and compliant guidance by a powered knee exoskeleton for robot-assisted rehabilitation of gait,” *Advanced Robotics*, vol. 25, no. 5, pp. 513–535, 2011.
- [12] T. Choi and J. Lee, “Control of manipulator using pneumatic muscles for enhanced safety,” *IEEE Transactions on Industrial Electronics*, vol. 57, pp. 2815–2825, Aug 2010.
- [13] S. Fisher, L. Lucas, and T. A. Thrasher, “Robot-assisted gait training for patients with hemiparesis due to stroke,” *Topics in Stroke Rehabilitation*, vol. 18, no. 3, pp. 269–276, 2011. PMID: 21642064.
- [14] J. H. Lilly and P. M. Quesada, “A two-input sliding-mode controller for a planar arm actuated by four pneumatic muscle groups,” *IEEE Transactions on Neural Systems and Rehabilitation Engineering*, vol. 12, pp. 349–359, Sept 2004.
- [15] T.-J. Yeh, M.-J. Wu, T.-J. Lu, F.-K. Wu, and C.-R. Huang, “Control of mckibben pneumatic muscles for a power-assist, lower-limb orthosis,” *Mechatronics*, vol. 20, no. 6, pp. 686 – 697, 2010.
- [16] T. Kawamura, K. Takanaka, T. Nakamura, and H. Osumi, “Development of an orthosis for walking assistance using pneumatic artificial muscle: A quantitative assessment of the effect of assistance,” in *2013 IEEE 13th International Conference on Rehabilitation Robotics (ICORR)*, pp. 1–6, June 2013.
- [17] M. Kumamoto, T. Oshima, and T. Yamamoto, “Control properties induced by the existence of antagonistic pairs of bi-articular muscles—mechanical engineering model analyses,” *Human Movement Science*, vol. 13, no. 5, pp. 611–634, 1994.

-
- [18] Q.-T. Dao, H. Moriko, and S.-i. Y. Yamamoto, "Design and evaluation of the lower-limb robotic orthosis for gait rehabilitation actuated by pneumatic artificial muscle," in *Proceedings of the 2nd International Conference on Biomedical Signal and Image Processing*, pp. 85–89, ACM, 2017.
- [19] Y. Shibata, S. Imai, T. Nobutomo, T. Miyoshi, and S. Yamamoto, "Development of body weight support gait training system using antagonistic bi-articular muscle model," in *2010 Annual International Conference of the IEEE Engineering in Medicine and Biology*, pp. 4468–4471, Aug 2010.
- [20] M. A. M. Dzahir, T. Nobutomo, and S. I. Yamamoto, "Development of body weight support gait training system using pneumatic mckibben actuators - control of lower extremity orthosis-," in *2013 35th Annual International Conference of the IEEE Engineering in Medicine and Biology Society (EMBC)*, pp. 6417–6420, July 2013.
- [21] F. Prattico, M. Dzahir, and S. ichiroh Yamamoto, "Computed-torque method for the control of a 2-dof orthosis actuated through pneumatic artificial muscles: a specific case for the rehabilitation of the lower limb," *Indian Ocean Review of Science and Technology*, vol. 3, pp. 1–9, 2014.
- [22] S. Hussain, S. Q. Xie, and P. K. Jamwal, "Control of a robotic orthosis for gait rehabilitation," *Robotics and Autonomous Systems*, vol. 61, no. 9, pp. 911 – 919, 2013.
- [23] S. Hussain, S. Q. Xie, and P. K. Jamwal, "Adaptive impedance control of a robotic orthosis for gait rehabilitation," *IEEE Transactions on Cybernetics*, vol. 43, pp. 1025–1034, June 2013.
- [24] S. Hussain, S. Q. Xie, and P. K. Jamwal, "Robust nonlinear control of an intrinsically compliant robotic gait training orthosis," *IEEE Transactions on Systems, Man, and Cybernetics: Systems*, vol. 43, pp. 655–665, May 2013.
- [25] S. Hussain, P. K. Jamwal, M. H. Ghayesh, and S. Q. Xie, "Assist-as-needed control of an intrinsically compliant robotic gait training orthosis," *IEEE Transactions on Industrial Electronics*, vol. 64, pp. 1675–1685, Feb 2017.

-
- [26] Duschau-Wicke, Alexander, Caprez, Andrea, and R. Robert, "Patient-cooperative control increases active participation of individuals with sci during robot-aided gait training," *Journal of NeuroEngineering and Rehabilitation*, vol. 7, p. 43, Sep 2010.
- [27] S. K. Banala, S. H. Kim, S. K. Agrawal, and J. P. Scholz, "Robot assisted gait training with active leg exoskeleton (alex)," *IEEE Transactions on Neural Systems and Rehabilitation Engineering*, vol. 17, pp. 2–8, Feb 2009.
- [28] W. H. ORGANIZATION, "World report on disability 2011," *www.who.int*, vol. 1, no. 1, pp. 1–350, 2011.
- [29] D. B. Reynolds, D. W. Repperger, C. A. Phillips, and G. Bandry, "Modeling the dynamic characteristics of pneumatic muscle," *Annals of Biomedical Engineering*, vol. 31, pp. 310–317, Mar 2003.
- [30] K. Xing, J. Huang, Y. Wang, J. Wu, Q. Xu, and J. He, "Tracking control of pneumatic artificial muscle actuators based on sliding mode and non-linear disturbance observer," *IET Control Theory Applications*, vol. 4, pp. 2058–2070, October 2010.
- [31] D. X. Ba and K. K. Ahn, "Indirect sliding mode control based on gray-box identification method for pneumatic artificial muscle," *Mechatronics*, vol. 32, pp. 1 – 11, 2015.
- [32] T. V. Minh, T. Tjahjowidodo, H. Ramon, and H. V. Brussel, "Cascade position control of a single pneumatic artificial muscle–mass system with hysteresis compensation," *Mechatronics*, vol. 20, no. 3, pp. 402 – 414, 2010.
- [33] G. Andrikopoulos, G. Nikolakopoulos, and S. Manesis, "Adaptive internal model control scheme for a pneumatic artificial muscle," in *2013 European Control Conference (ECC)*, pp. 772–777, July 2013.
- [34] J. H. Lilly and L. Yang, "Sliding mode tracking for pneumatic muscle actuators in opposing pair configuration," *IEEE Transactions on Control Systems Technology*, vol. 13, pp. 550–558, July 2005.
- [35] T. Choi, B. Choi, and K. Seo, "Position and compliance control of a pneumatic muscle actuated manipulator for enhanced safety," *IEEE Transactions on Control Systems Technology*, vol. 19, pp. 832–842, July 2011.

-
- [36] S. Xie, J. Mei, H. Liu, and Y. Wang, “Hysteresis modeling and trajectory tracking control of the pneumatic muscle actuator using modified prandtl–ishlinskii model,” *Mechanism and Machine Theory*, vol. 120, pp. 213 – 224, 2018.
- [37] T. KOSAKI, A. MINESAKI, and M. SANO, “Adaptive hysteresis compensation with a dynamic hysteresis model for control of a pneumatic muscle actuator,” *Journal of Environment and Engineering*, vol. 7, no. 1, pp. 53–65, 2012.
- [38] T. Vo-Minh, T. Tjahjowidodo, H. Ramon, and H. V. Brussel, “A new approach to modeling hysteresis in a pneumatic artificial muscle using the maxwell-slip model,” *IEEE/ASME Transactions on Mechatronics*, vol. 16, pp. 177–186, Feb 2011.
- [39] T. V. Minh, B. Kamers, H. Ramon, and H. V. Brussel, “Modeling and control of a pneumatic artificial muscle manipulator joint – part i: Modeling of a pneumatic artificial muscle manipulator joint with accounting for creep effect,” *Mechatronics*, vol. 22, no. 7, pp. 923 – 933, 2012.
- [40] D. X. Ba, T. Q. Dinh, and K. K. Ahn, “An integrated intelligent nonlinear control method for a pneumatic artificial muscle,” *IEEE/ASME Transactions on Mechatronics*, vol. 21, pp. 1835–1845, Aug 2016.
- [41] R. M. Robinson, C. S. Kothera, R. M. Sanner, and N. M. Wereley, “Nonlinear control of robotic manipulators driven by pneumatic artificial muscles,” *IEEE/ASME Transactions on Mechatronics*, vol. 21, pp. 55–68, Feb 2016.
- [42] L. Cveticanin, M. Zukovic, I. Biro, and J. Sarosi, “Mathematical investigation of the stability condition and steady state position of a pneumatic artificial muscle – mass system,” *Mechanism and Machine Theory*, vol. 125, pp. 196 – 206, 2018.
- [43] L. Zhao, X. Liu, and T. Wang, “Trajectory tracking control for double-joint manipulator systems driven by pneumatic artificial muscles based on a nonlinear extended state observer,” *Mechanical Systems and Signal Processing*, vol. 122, pp. 307 – 320, 2019.

-
- [44] Y. Yuan, Y. Yu, Z. Wang, and L. Guo, “A sampled-data approach to nonlinear eso-based active disturbance rejection control for pneumatic muscle actuator systems with actuator saturations,” *IEEE Transactions on Industrial Electronics*, vol. 66, pp. 4608–4617, June 2019.
- [45] L. Zhao, H. Cheng, Y. Xia, and B. Liu, “Angle tracking adaptive backstepping control for a mechanism of pneumatic muscle actuators via an aeso,” *IEEE Transactions on Industrial Electronics*, vol. 66, pp. 4566–4576, June 2019.
- [46] A. Merola, D. Colacino, C. Cosentino, and F. Amato, “Model-based tracking control design, implementation of embedded digital controller and testing of a biomechatronic device for robotic rehabilitation,” *Mechatronics*, vol. 52, pp. 70 – 77, 2018.
- [47] Y. Yuan, Y. Yu, and L. Guo, “Nonlinear active disturbance rejection control for the pneumatic muscle actuators with discrete-time measurements,” *IEEE Transactions on Industrial Electronics*, vol. 66, pp. 2044–2053, March 2019.
- [48] H. Yang, Y. Yu, and J. Zhang, “Angle tracking of a pneumatic muscle actuator mechanism under varying load conditions,” *Control Engineering Practice*, vol. 61, pp. 1 – 10, 2017.
- [49] L. Zhao, Q. Li, B. Liu, and H. Cheng, “Trajectory tracking control of a one degree of freedom manipulator based on a switched sliding mode controller with a novel extended state observer framework,” *IEEE Transactions on Systems, Man, and Cybernetics: Systems*, vol. 49, pp. 1110–1118, June 2019.
- [50] S. Devasia, D. Chen, and B. Paden, “Nonlinear inversion-based output tracking,” *IEEE Transactions on Automatic Control*, vol. 41, pp. 930–942, July 1996.
- [51] S. Devasia, “Should model-based inverse inputs be used as feedforward under plant uncertainty?,” *IEEE Transactions on Automatic Control*, vol. 47, pp. 1865–1871, Nov 2002.
- [52] D. A. Winter, *Biomechanics and motor control of human movement*. John Wiley & Sons, 2009.

-
- [53] G. Andrikopoulos, G. Nikolakopoulos, and S. Manesis, “Advanced nonlinear pid-based antagonistic control for pneumatic muscle actuators,” *IEEE Transactions on Industrial Electronics*, vol. 61, pp. 6926–6937, Dec 2014.
- [54] P. Shah and S. Agashe, “Review of fractional pid controller,” *Mechatronics*, vol. 38, pp. 29–41, 2016.
- [55] Y. Chen, I. Petras, and D. Xue, “Fractional order control—a tutorial,” in *American Control Conference, 2009. ACC’09.*, pp. 1397–1411, IEEE, 2009.
- [56] M. Ö. Efe, “Fractional order systems in industrial automation—a survey,” *IEEE Transactions on Industrial Informatics*, vol. 7, no. 4, pp. 582–591, 2011.
- [57] M. Nguyen and X. Chen, “Discrete-time fractional order integral sliding mode control for piezoelectric actuators with improved performance based on fuzzy tuning,” vol. 2018-July, pp. 554–559, 2019. cited By 0.
- [58] S. Freivogel, J. Mehrholz, T. Husak-Sotomayor, and D. Schmalohr, “Gait training with the newly developed ‘lokoHELP’-system is feasible for non-ambulatory patients after stroke, spinal cord and brain injury. a feasibility study,” *Brain Injury*, vol. 22, no. 7-8, pp. 625–632, 2008.
- [59] S. J. Behrman, A. L. Harkema, “Locomotor training after human spinal cord injury: a series of case studies,” *Phys Ther*, vol. 80, pp. 688–700, Jul 2000.
- [60] P. Horata, S. Chiewchanwattana, and K. Sunat, “A comparative study of pseudo-inverse computing for the extreme learning machine classifier,” in *The 3rd International Conference on Data Mining and Intelligent Information Technology Applications*, pp. 40–45, Oct 2011.
- [61] Q.-T. Dao and S.-i. Yamamoto, “Assist-as-needed control of a robotic orthosis actuated by pneumatic artificial muscle for gait rehabilitation,” *Applied Sciences*, vol. 8, no. 4, 2018.
- [62] M. D. Lewek, T. H. Cruz, J. L. Moore, H. R. Roth, Y. Y. Dhaher, and T. G. Hornby, “Allowing intralimb kinematic variability during locomotor training poststroke improves kinematic consistency: A subgroup analysis from a randomized clinical trial,” *Physical Therapy*, vol. 89, no. 8, pp. 829–839, 2009.

- [63] M. A. Perez, B. K. S. Lugholt, K. Nyborg, and J. B. Nielsen, "Motor skill training induces changes in the excitability of the leg cortical area in healthy humans," *Experimental Brain Research*, vol. 159, pp. 197–205, Nov 2004.
- [64] A. A. Timmermans, H. A. Seelen, R. D. Willmann, and H. Kingma, "Technology-assisted training of arm-hand skills in stroke: concepts on reacquisition of motor control and therapist guidelines for rehabilitation technology design," *Journal of NeuroEngineering and Rehabilitation*, vol. 6, p. 1, Jan 2009.
- [65] R. Shadmehr and F. A. Mussa-Ivaldi, "Adaptive representation of dynamics during learning of a motor task.," *The Journal of neuroscience : the official journal of the Society for Neuroscience*, vol. 14 5 Pt 2, pp. 3208–24, 1994.
- [66] J. H. Graham, J. F. Meagher, and S. J. Derby, "A safety and collision avoidance system for industrial robots," *IEEE Transactions on Industry Applications*, vol. IA-22, pp. 195–203, Jan 1986.
- [67] B. Karlsson, N. Karlsson, and P. Wide, "A dynamic safety system based on sensor fusion," *Journal of Intelligent Manufacturing*, vol. 11, pp. 475–483, Oct 2000.
- [68] E. Ohashi, T. Aiko, T. Tsuji, H. Nishi, and K. Ohnishi, "Collision avoidance method of humanoid robot with arm force," *IEEE Transactions on Industrial Electronics*, vol. 54, pp. 1632–1641, June 2007.
- [69] M. Zinn, O. Khatib, B. Roth, and J. K. Salisbury, "Playing it safe [human-friendly robots]," *IEEE Robotics Automation Magazine*, vol. 11, pp. 12–21, June 2004.
- [70] Q. Dao and S. Yamamoto, "Modified computed torque control of a robotic orthosis for gait rehabilitation," in *2018 40th Annual International Conference of the IEEE Engineering in Medicine and Biology Society (EMBC)*, pp. 1719–1722, July 2018.

Research Achievements

Journals

- [P.1] Quy-Think Dao, Yamamoto, S.I, “Discrete-Time Fractional Order Integral Sliding Mode Control of an Antagonistic Actuator Driven by Pneumatic Artificial Muscles”. *Applied Sciences*, 2019. 9(12): p. 2503.
- [P.2] Quy-Think Dao, Yamamoto, S.I, “Assist-as-Needed Control of a Robotic Orthosis Actuated by Pneumatic Artificial Muscle for Gait Rehabilitation”. *Appl. Sci.* 2018, 8, 499.

International conference papers

- [P.3] Quy-Think Dao, Yamamoto, S.I, “Safety Enhancement of a Pneumatic Artificial Muscle Actuated Robotic Orthosis for Gait Rehabilitation.”, In *2018 3rd Asia-Pacific Conference on Intelligent Robot Systems (ACIRS)*, Nagoya, 2019.
Award: Excellent Oral Presentation Award.
- [P.4] Quy-Think Dao, Yamamoto, S.I, “Modified Computed Torque Control of a Robotic Orthosis for Gait Rehabilitation.”, In *Proceedings of the 40th Annual International Conference of the IEEE Engineering in Medicine and Biology Society, EMBC’18*, Honolulu Hawaii USA, 17-21 July 2018
- [P.5] Quy-Think Dao, Yamamoto S.I (2019) “Adaptive Impedance Control of a Robotic Orthosis Actuated by Pneumatic Artificial Muscle”. In: *Lhotska L., Sukupova L., Lacković I., Ibbott G. (eds) World Congress on Medical Physics and Biomedical Engineering 2018. IFMBE Proceedings*, vol 68/2.
Award: Young Investigator Challenge Finalist of IFMBE.
- [P.6] Quy-Think Dao, Shin-ichiroh Yamamoto, “Trajectory Tracking Control of a Robotic Orthosis for Gait Rehabilitation: A Feedforward-Feedback Con-

trol Approach”, *The 10th Biomedical Engineering International Conference (BMEiCON-2017)*, Hokkaido, Japan, 2017.

- [P.7] Quy-Thinkh Dao, Moriko Hagiwara, Shin-ichiroh Yamamoto, “Design and Evaluation of the Lower-limb Robotic Orthosis for Gait Rehabilitation Actuated by Pneumatic Artificial Muscle”, In proceedings of *the 5th International Conference on Biological and Medical Sciences ICBMS 2017*, KitaKuyShu, Japan.

Award: Best Presentation Award.